



UNIVERSIDAD JUÁREZ AUTÓNOMA DE TABASCO

DIVISIÓN ACADÉMICA DE CIENCIAS BÁSICAS



**Structural, optical and photocatalytic
properties of $\text{Bi}_{1-x}\text{AxFeO}_3$ ($\text{A} = \text{Ca, Sr}$)
synthesized by Pechini method**

A THESIS

In Partial Fulfilment of the Requirements for the
Degree of

**Maestría en Ciencias en Química Aplicada
con Orientación en Fisicoquímica**

Submitted by:

B.Sc. Evaristo Salaya Gerónimo

Supervisor:

Dr. David Salvador García Zaleta (UJAT-DAMJM)

Cunduacán, Tabasco

September 2020



UNIVERSIDAD JUÁREZ
AUTÓNOMA DE TABASCO
ESTUDIO EN LA DUDA. ACCIÓN EN LA FE"



División
Académica
de Ciencias
Básicas



DIRECCIÓN

10 de septiembre de 2020

Ing. Evaristo Salaya Gerónimo
Pasante de la Maestría en Ciencias
en Química Aplicada
PRESENTE

Por medio de la presente y de la manera más cordial, me dirijo a usted para hacer de su conocimiento que proceda a la impresión del trabajo titulado "**Structural, optical and photocatalytic properties of Bi_{1-x}A_xFeO₃ (A=Ca, Sr) synthesized by Pechini method**" en virtud de que reúne los requisitos para el EXAMEN PROFESIONAL para obtener el grado de Maestro en Ciencias en Química Aplicada.

Sin otro particular, reciba un cordial saludo.

Atentamente

Dr. Gerardo Delgadillo Piñón

Director

C.c.p.-Archivo.

Miembro CUMEX desde 2008



UNA ALIANZA DE CALIDAD POR LA EDUCACIÓN SUPERIOR

Km.1 Carretera Cunduacán-Jalpa de Méndez, A.P. 24, C.P. 86690, Cunduacán, Tab., México.
Tel/Fax: (993) 3581500 Ext. 6702,6701 E-Mail: dirección.dacb@ujat.mx

www.ujat.mx

CARTA AUTORIZACIÓN

El que suscribe, autoriza por medio del presente escrito a la Universidad Juárez Autónoma de Tabasco para que utilice tanto física como digitalmente el Trabajo Receptacional en la modalidad de Tesis denominada: "**Structural, optical and photocatalytic properties of Bi_{1-x}A_xFeO₃ (A = Ca, Sr) synthesized by Pechini method**", de la cual soy autor y titular de los Derechos de Autor.

La finalidad del uso por parte de la Universidad Juárez Autónoma de Tabasco del Trabajo Receptacional antes mencionado, será única y exclusivamente para difusión, educación y sin fines de lucro; autorización que se hace de manera enunciativa mas no limitativa para subirla a la Red Abierta de Bibliotecas Digitales (RABID) y a cualquier otra red académica con las que la Universidad tenga relación institucional.

Por lo antes manifestado, libero a la Universidad Juárez Autónoma de Tabasco de cualquier reclamación legal que pudiera ejercer respecto al uso y manipulación de la tesis mencionada y para los fines estipulados en este documento.

Se firma la presente autorización en la ciudad de Cunduacán, Tabasco el Día 10 de Septiembre de 2020.

AUTORIZO

I.A. EVARISTO SALAYA GERÓNIMO

Universidad Juárez Autónoma de Tabasco.
Dedicated to
My Family
&
To Mother Nature
'for being a source of inspiration and experience'

Acknowledgments

This thesis has been come out due to the help, support, guidance, and collaboration from many people. Some of them are mentioned here:

I would like to express my extreme thanks and gratitude to my supervisor Dr. David Salvador García Zaleta for his support, guidance, encouragement and help during my master research.

Also, my sincere gratitude to Dr. Ali M. Abdel-Mageed for his monitoring, comments, and suggestions throughout my international research in Ulm University.

Special thanks to Dr. Gabriela Jácome Acatitla, Pablo Daniel and Julieta and for their collaboration, useful discussions and the funny moments that we spent together.

I would like to thank all the present and past members of the nanotechnology, the MCQA and the IOK groups for their collaboration, help and friendship.

I would like to express my thanks to Dr. José Pacheco Sosa and Dr. J. Gilberto Torres Torres for taking care of all the administrative work of my thesis defense. Also, for taking care of all DACB-UJAT administrative work.

I appreciate the Consejo Nacional de Ciencia y Tecnología (CONACYT-Mexico) and Universidad Juárez Autónoma de Tabasco (Mexico) for the financial support.

Finally, I would like to extremely thank my parents for their support, unlimited love, and prayers from the faraway distance to keep me going on. I sincerely appreciate my sisters and my brothers for their support, love, and encouragements.

Cunduacán, June 2020

Evaristo Salaya Gerónimo

Resumen

En el presente trabajo se investigó el efecto del dopaje con cationes de Ca y Sr en las propiedades estructurales y fotocatalíticas del BiFeO₃ (BFO). Se prepararon series de polvos de BFO dopado a diferentes concentraciones de Ca y Sr ($\text{Bi}_{1-x}\text{A}_x\text{FeO}_3$, $x = 0, 0.05, 0.10, 0.15$; A = Ca, Sr) por medio del método Pechini modificado. Los resultados de XRD revelaron la formación de la estructura romboédrica (R3c) en todos los materiales sintetizados, así como la incorporación de los iones de Ca²⁺ and Sr²⁺ en la estructural de BFO. El tamaño promedio del cristalito en las nanopartículas de BFO se calculó usando la ecuación de Scherrer; los tamaños de cristalito resultaron dentro del rango de 23 – 55 nm. Además, El porcentaje de fases en los compuestos se determinó por medio del refinamiento Rietveld. Los resultados de SEM mostraron cambios en el tamaño de grano de las muestras, lo cual fue atribuido al aumento de vacancias de oxígeno. Los resultados de la espectroscopía UV-Vis mostraron una disminución gradual en los valores de banda prohibida conforme la concentración de dopante aumentaba. El análisis superficial por XPS reveló los picos característicos de bismuto y hierro en los compuestos de BiFeO₃, así como los picos de Ca y Sr en las muestras dopadas. La actividad fotocatalítica de los fotocatalizadores de BCaFO y BSrFO se evaluó por medio de la degradación de azul de metileno y 4-clorofenol. Se observó que la actividad fotocatalítica se vio afectada por la concentración de dopante. Las muestras de BCaFO y BSrFO mostraron una mayor respuesta comparadas con la muestra de BiFeO₃ sin dopar, esto debido a que la sustitución con iones alcalinos optimizó tanto la absorción de luz visible como la efectiva separación de electrones y huecos en las muestras dopadas de BFO. Finalmente, se observó que las vacancias de oxígeno en la superficie, inducidas por el dopaje con Ca y Sr, inhibieron la recombinación de pares electrón-hueco, lo cual propició la efectiva transferencia de transportadores de carga fotogenerados hacia la superficie.

Abstract

In this work, the effect of Ca and Sr doping on the structural and photocatalytic properties of BiFeO_3 (BFO) was investigated. A series of Ca and Sr doped BFO nanoparticles containing different dopant contents ($\text{Bi}_{1-x}\text{A}_x\text{FeO}_3$, $x = 0, 0.05, 0.10, 0.15$; A = Ca, Sr) were prepared by a modified Pechini method. XRD results revealed the formation of rhombohedral structure ($R\bar{3}c$) in all the compounds, as well as the successful incorporation of Ca^{2+} and Sr^{2+} ions into the BFO structure. The average crystallite sizes of BFO nanoparticles were calculated by Scherrer equation revealing sizes in the range of 23 - 55 nm. Due to small traces of secondary phases, as orthorhombic and/or tetragonal, were observed in the doped compounds, the percentages of phases were determined by Rietveld refinement. SEM results showed changes in the grain size of the samples attributed to the promotion of oxygen vacancies. UV-Vis spectroscopy results showed a gradual decrement of the band gap values when the dopant concentration increased. The surface analysis by XPS technique revealed the characteristic peaks of Fe and Bi in the BiFeO_3 compound, among the peaks of Ca and Sr in the doped samples. The photocatalytic activity of BCaFO and BSrFO photocatalysts was evaluated by the degradation of methylene blue and 4-chlorophenol. The photocatalytic activity was found to be enhanced by the doping content. The BCaFO and BSrFO samples showed higher photocatalytic activity compared to the undoped BiFeO_3 sample, attributed to the enhanced visible light absorption and the successful separation of photogenerated electrons and holes in the doped samples. Additionally, the surface oxygen vacancies, induced by Ca and Sr doping, inhibited the recombination of electron-holes, which could promote the relocation of photogenerated charge carriers to the surface.

Table of Contents

Chapter 1: Introduction.....	1
1.1 General introduction	2
1.2 Motivation and problem statement.....	4
1.3 Dissertation organization	6
Chapter 2: Review of the Development of doped BiFeO₃ for the Degradation of Organic Pollutants	7
2.1 Degradation of organic pollutants	8
2.2 Photocatalysis.....	14
2.3 BiFeO ₃ as photocatalyst	19
2.3.1 Methods of synthesis.....	22
2.3.2 Doping	25
Chapter 3: Synthesis and Characterization of the Materials: Methods and Techniques	29
3.1 Synthesis of Bi _{1-x} A _x FeO ₃	30
3.2 Catalyst characterization.....	32
3.2.1 X-Ray Diffraction (XRD)	32
3.2.2 Rietveld Refinement.....	32
3.2.3 Scanning Electron Microscopy (SEM)	33
3.2.4 UV-Vis Diffuse Reflectance Spectroscopy (DRS).....	33
3.2.5 X-Ray Photoelectron Spectroscopy (XPS)	33
3.3 Probe degradations	35
Chapter 4: Characterizations of Bi_{1-x}A_xFeO₃: Results and Discussion.....	36
4.1 X-Ray Diffraction (XRD).....	37
4.2 Rietveld Refinement.....	41
4.3 Scanning Electron Microscopy (SEM).....	46
4.4 UV-Vis Diffuse Reflectance Spectroscopy (DRS)	52
4.5 X-Ray Photoelectron Spectroscopy (XPS).....	56

Chapter 5: Photocatalytic Activity of $B_{1-x}A_xFeO_3$.....	60
5.1 Methylene blue photocatalytic degradation.....	61
5.2 4-chlorophenol photocatalytic degradation	66
Conclusions.....	71
References	72
Annexes	91
A.1 X-Ray Diffraction (XRD)	92
A.2 Rietveld Refinement	96
A.3 Scanning Electron Microscopy (SEM)	98
A.4 UV-Vis Diffuse Reflectance Spectroscopy (DRS).....	102
A.6 X-Ray Photoelectron Spectroscopy (XPS)	106

Table of figures

Figure 1. Skeletal formula of methylene blue.	10
Figure 2. Skeletal formula of 4-chlorophenol.	12
Figure 3. Primary processes in semiconductor photocatalysis.	14
Figure 4. Schematic of ABO_3 perovskite structure; a) lattice and b) polyhedrons.	19
Figure 5. Structures of BiFeO_3 . (a) The cubic perovskite unit cell. (b) Two pseudo-cubic cells with cation shifts and octahedra rotations (c) the rhombohedral cell. (d) The highly distorted tetragonal-like phase of BFO.	21
Figure 6. Schematic of the Pechini process to obtain metal/organic gels.....	24
Figure 7. Scheme of the modified Pechini method followed in this study.....	31
Figure 8. a) XRD patterns for as-prepared BFO NPs; b) patterns of the main peak between 31° and 33° in BFO samples.....	37
Figure 9. a) XRD patterns for BCaFO-05, BCaFO10 and BCaFO-15 NPs; b) patterns of the main peak between 31° and 33° in Ca doped BFO samples.	38
Figure 10. a) XRD patterns for BSrFO-05, BSrFO10 and BSrFO-15 NPs; b) patterns of the main peak between 31° and 33° in Sr doped BFO samples.	39
Figure 11. Rietveld refinement of the XRD patterns of undoped BFO sample. The differences between observed (red circles) and calculated (blue line) spectra are plotted (grey line). Bragg reflections are indicated by ticks..	41
Figure 12. Rietveld refinement of the XRD patterns of a) BCaFO-05, b) BCaFO-10, and c) BCaFO-15 samples. The differences between observed (red circles) and calculated (blue line) spectra are plotted (grey line). Bragg reflections are indicated by ticks.	43

Figure 13. Rietveld refinement of the XRD patterns of a) BSrFO-05, b) BSrFO-10, and c) BSrFO-15 samples. The differences between observed (red circles) and calculated (blue line) spectra are plotted (grey line). Bragg reflections are indicated by ticks.....	45
Figure 14. SEM images and EDS spectrum of undoped BFO.....	46
Figure 15. SEM images of a) and b) BCaFO-05; c) and d) BCa-FO-10; e) and f) BCaFO-15 samples.....	48
Figure 16. SEM images of a) BCaFO-05; c) BCaFO-10; and e) BCaFO-15. EDS spectra of b) BCaFO-05; d) BCaFO-10; and f) BCaFO-15 samples.....	49
Figure 17. SEM images of a) and b) BSrFO-05; c) and d) BSr-FO-10; e) and f) BSrFO-15.	50
Figure 18. SEM images of a) BSrFO-05; c) BSrFO-10; and e) BSrFO-15. EDS spectra of b) BSrFO-05; d) BSrFO-10; and f) BSrFO-15 samples.....	51
Figure 19. Tauc plot $(\alpha h\nu)^2$ vs Eg of BFO.....	52
Figure 20. Tauc plot $(\alpha h\nu)^2$ vs Eg of BFO-Ca ($0 < x < 0.15$).....	53
Figure 21. Tauc plot $(\alpha h\nu)^2$ vs Eg of BFO-Sr ($0 < x < 0.15$).....	54
Figure 22. a) XPS wide-scan spectra of the prepared undoped BFO sample; b) Bi 4f peaks; c) Fe 2p peaks; d) XPS O 1s peaks.....	57
Figure 23. a) XPS wide-scan spectra of the BCaFO-10 sample; b) Ca 2p peaks; c) Fe 2p peaks; d) XPS O 1s peaks.....	58
Figure 24. a) XPS wide-scan spectra of the BSrFO-10 sample; b) Sr 3d peaks; c) Fe 2p peaks; d) XPS O 1s peaks.....	59

Figure 25. Photocatalytic degradation of MB as a function of the irradiation time under visible light for the BCaFO-05, BCaFO-10 and BCaFO-15 samples.	62
Figure 26. Kinetic curves for the photocatalytic degradation of MB under sunlight irradiation using BCaFO-05, BCaFO-10 and BCaFO-15 samples.....	63
Figure 27. Photocatalytic degradation of MB as a function of the irradiation time under visible light for the BSrFO-05, BSrFO-10 and BSrFO-15 samples.	64
.....	64
Figure 28. Kinetic curves for the photocatalytic degradation of MB under sunlight irradiation using BSrFO-05, BSrFO-10 and BSrFO-15 samples.....	65
Figure 29. Photocatalytic degradation of 4CP as a function of the irradiation time under visible light for the BCaFO-05, BCaFO-10 and BCaFO-15 samples.	67
.....	67
Figure 30. Kinetic curves for the photocatalytic degradation of 4CP under sunlight irradiation using BCaFO-05, BCaFO-10 and BCaFO-15 samples.....	68
Figure 31. Photocatalytic degradation of 4CP as a function of the irradiation time under visible light for the BSrFO-05, BSrFO-10 and BSrFO-15 samples.	69
.....	69
Figure 32. Kinetic curves for the photocatalytic degradation of 4CP under sunlight irradiation using BSrFO-05, BSrFO-10 and BSrFO-15 samples.....	70

List of tables

Table 1. Physicochemical properties of methylene blue and 4-chlorophenol.....	10
Table 2. The reactions involved in the photocatalytic oxidation process for the degradation of organic pollutants.....	15
Table 3. Structures parameters of BiFeO ₃	22
Table 4. Average crystallite size for BFO, BCaFO and BSrFO powders.....	40
Table 5. Refinement parameters of BFO sample.	42
Table 6. Refinement parameters of BCaFO-05, BCaFO-10 and BCaFO-15 samples.	42
Table 7. Refinement parameters of BSrFO-05, BSrFO-10 and BSrFO-15 samples.	44
Table 8. Band gap values for as prepared BFO, BCaFO and BSrFO samples.	55

Chapter 1: Introduction

Universidad Juárez Autónoma de Tabasco.
México.

1.1 General introduction

The intensive industrial development has caused an important environmental pollution [1]. This issue has been a major concern for ecosystems and human health attracting the global consideration for its solution. Consequently, several organic pollutants, such as textile dyes, pesticides and insecticides, have been detected in the aquatic environment [2].

In this sense, dyes, widely used in the textile and printing industries [3], have caused water pollution due to their discharge into the environment, chemical stability, complex molecular structure and synthetic origin; thus they are difficult to treat [4]. Similarly, pesticides have been employed extensively in agricultural practices to control weeds (herbicides), insects (insecticides) or fungi (fungicides) and to increase crop yields [5]. In general, these compounds are applied in higher quantities than those required, are toxic and prevalent in the environment; subsequently, there is a need to remove them [6].

Advanced Oxidation Processes (AOPs) have emerged as alternative techniques for treatment of hazardous pollutants [7]. AOPs are based on the in situ production of highly reactive hydroxyl radicals ($\cdot\text{OH}$) that non-selectively react with most organics, being able to degrade even highly recalcitrant compounds [8].

Photocatalysis (as an AOP) has attracted much attention on the environmental pollution control, due to its prominent features, such as high efficiency, low energy consumption, mild reaction conditions, wide application and minimal secondary pollution [9]. In addition, the visible light active photocatalysts are non-toxic, relatively inexpensive, have high surface area and broad absorption spectra ranging from UV to visible region [10,11]. However, there are a few research gaps identified in the application of photocatalysis, such as low quantum efficiency due to inefficient visible light harvesting, design of suitable photoreactor, recovery, reuse, scale-up, etc. [12].

In recent years, scientific reports on the synthesis and characterization of BiFeO_3 (BFO), with a rhombohedral distorted perovskite, as a promising photocatalyst for

the degradation of many organic pollutants have increased significantly, which can be attributed to its narrow band gap and excellent chemical stability [13–16]. However, many strategies have been developed to enhance the photocatalytic efficiency of BFO by modifying its properties as size and morphology of its particles, cation doping, and coupling with other semiconductors [17–20].

In this work, $\text{Bi}_{1-x}\text{A}_x\text{FeO}_3$ ($\text{A} = \text{Ca}^{2+}, \text{Sr}^{2+}; x = 0.05, 0.1, 0.15$) compounds were synthesized by the Pechini method. The as-prepared materials were characterized by X-Ray Diffraction (XRD), Rietveld Refinement, Scanning Electron Microscopy (SEM), UV-Vis spectroscopy and X-Ray photoelectron Spectroscopy (XPS). The photocatalytic activity was evaluated in the degradation of methylene blue and 4-chlorophenol under visible light irradiation.

1.2 Motivation and problem statement

Among the many investigated photocatalyst materials in the past decades, BiFeO₃ remains as a candidate for potential applications in solar cells, solar fuels, and environmental cleaning applications [18,21]. Its narrow band gap of ~2.2 eV allows the material to use a large portion of visible light [22,23]. However, it suffers greatly in:

- Fast electron-hole pair recombination
- Presence of secondary phases

The successful incorporation of dopant elements in the BFO material has released new challenges to improve its photocatalytic activity [24]. Usually, a small quantity of dopant can inhibit the recombination rate of photo-generated charge carriers which helps in enhancing the photocatalytic activity of photocatalyst [25]. But the choice of a suitable dopant remains challenging [26]. If the amount of dopant exceeds to critical value then it may behave as recombination centers for photo-generated charge carriers, which can reduce the photocatalytic performance [27].

It is known that synthesizing single phase perovskite BFO ceramics is still a challenge to achieve [28]. During synthesis process, some unwanted impurity phases such as Bi₂₅FeO₃₉, Bi₂Fe₄O₉ and Bi₂O₃ are produced along with pure BFO [29,30]. The main reasons attributed to the appearance of impurities are the evaporation of Bi component during the preparation process due to the low decomposition temperature of bismuth salts, and the altered chemical valence of Fe ion in an oxygen-deficient atmosphere [31,32].

Several steps and strategies have been applied to increase the photocatalytic efficiency of BFO nanoparticles, as the modification of its structure by introducing elements as dopants [20,25]. In this thesis, undoped BiFeO₃ and doped-BiFeO₃ with alkaline cations (Ca²⁺, Sr²⁺) photocatalyst have been designed and prepared to report the issues of light absorption and charge carrier dynamics.

The effect of synthesis method of the material has been studied in terms of nano size and absence of secondary phases, which are believed to be favorable for photocatalytic applications [33]. A suitable Pechini method was selected for synthetizing BFO nanopowders with size distribution and uniform morphology.

The photocatalytic properties of undoped and doped BFO materials have been investigated for the degradation of various organic pollutants under visible light [21,24,26]. All prepared photocatalysts were tested under the reaction of photodegradation of organic pollutants such as methylene blue and 4-chlorophenol.

To summarize, the aim of the present thesis was to design, synthesize, characterize, and test undoped and doped-BiFeO₃ with alkaline cations (Ca²⁺, Sr²⁺) photocatalysts with the approach of optimizing their performance through understandings of the mechanisms for enhanced photocatalytic activity.

1.3 Dissertation organization

The thesis is divided into five chapters. First chapter explains the motivation of this research along with the problem statement of the study. The second chapter presents a detailed literature review on the area under study. The reported works in literature related to the degradation of organic compounds, the main process of photocatalysis, the BiFeO₃ introduced as photocatalyst, along the method of synthesis and doping effects are discussed. In the third chapter, the method of synthesis of all BFO samples is explained. This chapter also illustrates all the characterization techniques carried out for analysis of their properties in the present investigation. The fourth and fifth chapters present the results of the characterization techniques, as well, the photocatalytic response of the compounds, respectively. Finally, the conclusions of this work are presented.

Chapter 2: Review of the Development of doped BiFeO₃ for the Degradation of Organic Pollutants

Universidad Juárez Autónoma de Tabasco.

2.1 Degradation of organic pollutants

Nowadays, the growing human population has posed several challenges to the global economy, particularly in terms of energy security and environmental conservation. Global economy depends mainly on non-renewable and finite fossil fuels [34]. As a result, industries need to look for alternative strategies to make their production costs competitive and environment friendly [35]. Besides energy supply, water pollution by organic compounds arising from these industrial, agricultural and urban human activities is also a challenge to solve [36].

The common classes of compounds that occur in polluted water are solvents, dyes, dioxins, dibenzofurans, pesticides, polychlorinated biphenyls, chlorophenols, asbestos, arsenic, and heavy metals [37]. These compounds are persistent owing to their resistance to conventional chemical, biological and photolytic processes of degradation [38]. Owing to their toxicity, organic pollutants released into the aquatic ecosystem can cause various environmental problems and harm human health. They can be carcinogenic, teratogenic, mutagenic and interfere with the endocrine system [39].

Synthetic dyes are a necessity in various significant industries such as the leather, paper as well as textile industries for its color-giving properties [40]. Daily, once dyes have served their purpose, huge volume of them are discarded without further care into water bodies [41]. Therefore, textile wastewater treatment is a big challenge because it contains organic dyes which cause multiple and multi-scale damage to the receiving environment [42].

Dyes are often difficult to decompose in water as they have composite molecular structures that cause them to be more stable toward light and resistant to their degradation [43]. Textile wastewater effluents can be treated using several physicochemical methods. These physicochemical processes inherit several drawbacks such as expensive, limited application and sludge handling [44].

Though biological processes are attractive cost effective and environmental friendly, but microorganisms require additional carbon source for their growth to treat colored wastewater, and are also slow, require expensive equipment, and can lead to secondary pollution [45].

10

Among dyes, pesticide pollution has been also recognized as an important global issue with scientists and environmental agencies tackling the problem with the development of more biocompatible pesticides which aim to minimize the side effects on the non-target species. However, even low levels of these compounds in effluents may result in toxicity, with increased risk due to bio-accumulation and potential long term chronic effects [46]. Consequently, these types of effluents cannot be discharged directly into the environment [47].

The presence of phenols, which structure comprises an aromatic ring containing one or more hydroxyl substituents [48], in ecosystems is associated with the production and degradation of many pesticides [49]. However, the structure of a pesticide molecule determines its physicochemical properties and inherent biodegradation [50].

Phenol and derivatives are usually obtained from petroleum or coal tar [51]. Because of their extensive use in chemical, petrochemical and pharmaceutical industries, the removal of phenols from wastewater by means of an effective and economical method is essential for the safe discharge of effluents into natural water streams [52]. Besides, they are generally toxic, mutagenic and carcinogenic for aquatic and human life, and cause serious problems in the ecosystems [53].

The physicochemical properties of pollutants determine their behavior upon entering the water. Some relevant general and physical properties are summarized in Table 1, including the CAS number, density and solubility in water of methylene blue and 4-chlorophenol. Physical, chemical and biological technologies or combination of them, have been investigated to remove these organic compounds from wastewater [54].

Table 1. Physicochemical properties of methylene blue and 4-chlorophenol.

Chemical name	Cas no.	Density (g cm ⁻³)	Solubility in water (g L ⁻¹)	Ref.
Methylene blue	61-73-4	1.757	43.6	[55]
4-chlorophenol	106-48-9	1.31	27.1	[56]

Methylene blue, also known as methylthioninium (MB), with the chemical formula C₁₆H₁₈N₃SCl (Figure 1) and water solubility 43.6 g L⁻¹, is not especially toxic in comparison to other dyes, but it can cause some mental and physical disorders in large dosage (>7.0 mg kg⁻¹) [57]. Recently, it has been demonstrated that advanced oxidation processes (AOPs) possess many advantages and results in highly efficiency in the treatment of effluents containing MB. Removing MB from aqueous solution by various AOPs has been intensively investigated in the literature.

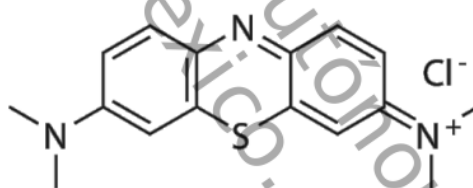


Figure 1. Skeletal formula of methylene blue.

Toxic organic compounds can be effectively oxidized by a simple electrochemical method, demonstrating that this method may be viable in degradation of a large group of dyes widely present in textile wastewater. The electrochemical oxidation of MB in aqueous solution has been studied by galvanostatic electrolysis using Pt/MnO₂ electrode as anode in presence of <0.1 mol L⁻¹ of sodium sulfate. After 120 min operated at pH 8, it was obtained higher than 90% of MB removal with a decrease of slightly over 70% of COD [58].

A novel nanocoated electrode was used on the sonoelectrochemical catalytic oxidation of MB wastewater. Since, nano-scale electrodes generate more hydroxyl radicals than non-nano-scale electrodes do, the treatment process was enhanced by ultrasound. Under optimum operating conditions, it resulted in a 92% removal efficiency [59].

Another important AOP, the conventional heterogeneous Fenton process holds great promise in the treatment of non-biodegradable organic pollutants by the generation of relatively non-selective, strong oxidative hydroxyl radicals ($\cdot\text{OH}$) by activating H_2O_2 with Fe^{2+} . It has been reported that paper mill sludge-derived heterogeneous catalyst (PMS-Fe-380) was tested for the degradation of MB. Under optimum conditions, 81% mineralization was achieved within 90 min, suggesting a promising and environmentally friendly method [60].

To improve this method, photodegradation of MB was evaluated under ultraviolet (UV) light irradiation in presence of H_2O_2 using novel hybrid nanostructures of $\alpha\text{-Fe}_2\text{O}_3$ anchored to graphene oxide nanosheet ($\alpha\text{-Fe}_2\text{O}_3@\text{GO}$) at pH 3. High efficiencies of MB degradation were achieved (around 96–100%). The results showed that the possible degradation mechanism of MB involved the rupture of phenyl ring due to the highly effective attack of reactive oxygen species [61].

Since ozone is a strong oxidant, ozonation is shown as a very effective AOP in decolorizing dyes present in wastewater to provide a solution to the environmental problem. The effect of ozone concentration with modeled and experimental data was evaluated for MB removal from aqueous solution in a continuous reactor. The results showed that increasing the inlet ozone gaseous concentration increased the rate of MB removal, assuming that MB removal by ozone is in the fast-kinetic regime [62].

The ozonation of MB in combination with UV light was reported. The results showed a complete decolorization of MB. Even though, neither the combination of ozonation with the UV irradiation nor increasing the pH value from 5 to 11 have shown synergistic effect on the decolorization efficiency of MB, a significant improvement in the mineralization efficiency was observed by exposure to the UV light [63]

Another important organic pollutant compound is 4-chlorophenol (4-CP), with chemical formula $\text{ClC}_6\text{H}_4(\text{OH})$ (Figure 2) and water solubility 27.1 g L^{-1} , which is known to exhibit chronic toxic effects, including potential carcinogenicity and mutagenic activity, and also believed to affect the central nervous system, causing nausea and convulsions [64].

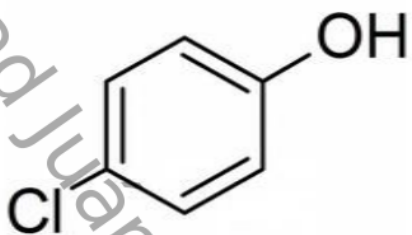


Figure 2. Skeletal formula of 4-chlorophenol.

Recently, the electrochemical degradation of 4-CP in chloride-rich wastewater was studied. A titanium cathode in combination with a coated anode ($\text{Ti/RuO}_2\text{-IrO}_2$) was used. The indirect oxidation resulted in the fast degradation of 4-chlorophenol throughout polychlorinated intermediates (2,4-dichlorophenol and 2,4,6-trichlorophenol). During prolonged treatment, these reaction intermediates are also further degraded [65].

Moreover, Pt/TiO_2 nanotubes have been prepared using an anodization oxidation method by applying voltage and further treated under UV light irradiation. Results showed that only 60% 4-CP was eliminated at the Pt electrode; however, the UV treated electrode exhibited a superior electrocatalytic activity (over 90%) toward the oxidation of 4CP. Attributing this improved activity to the enhanced donor density, conductivity, and high overpotential for oxygen evolution under UV irradiation [66].

Similarly, bimetallic zerovalent iron-silver nanoparticles (NZVI-Ag) immobilized in alginate beads have been synthesized and successfully tested on 4-CP dechlorination and complete degradation upon further Fenton oxidation by H_2O_2 .

addition after 30 min of reaction. The combined treatment allowed complete dechlorination and TOC removal at room temperature and initial pH= 3 [67].

In recent years, polyoxometalates have attracted attention for the Fenton (or Fenton-like) oxidation process. In 2015, an iron-containing silicotungstate ($\text{Fe}^{\text{III}}\text{AspSiW}$) was employed as a heterogeneous catalyst for Fenton oxidizing 4-CP. The $\text{Fe}^{\text{III}}\text{AspSiW}$ catalyst showed high activity for oxidation of 4-CP by H_2O_2 in a range from acidic to near neutral pH under irradiated conditions. The enhanced degradation of 4-CP under irradiation was attributed to the synergistic effect of Fenton-like catalysis of ferric iron and photocatalysis of anions present in $\text{Fe}^{\text{III}}\text{AspSiW}$ [68].

The catalytic ozonation on traditional MgO was substantially enhanced for removing 4-CP by preparing three sheet-like MgO materials. It is well known that the direction to tailor catalytic activity might change by selectively exposing a crystal facet. Results showed that the pseudo first-order reaction constant of 4-CP removal in ozonation catalyzed by the three sheet-like MgO was from 3.1 to 4.8 higher than in the single ozonation. It indicates that the catalytic activity significantly depends on the crystal facet besides the surface area [69].

Likewise, the catalytic properties of ultra-small β -FeOOH nanorods in ozonation of 4-CP has been reported. The removal efficiency of 4-CP was substantially enhanced achieving 99% in the presence of β -FeOOH/ozone compared to 67% in ozone alone after 40 min. The catalytic properties of the material during ozonation process were found to be evident at lower initial pH of 3.5, attributed to the heterogeneous surface breakdown of O_3 by β -FeOOH [70].

Since the chemical technologies have been found to produce secondary pollutants and prove to be expensive [71], the photocatalytic degradation is presented as an environmental friendly and low cost method, which may include complete mineralization, solution to the lack of waste disposal problem and applicability at normal temperature and pressure conditions [72].

2.2 Photocatalysis

Photocatalyst reactions (Figure 3) [73] begin when the catalyst absorbs electromagnetic radiation ($h\nu$) with energy equal to or greater than its band gap. A crucial step is the formation of electron and hole (e^-/h^+) pairs which require the promotion of electrons from the valence band (VB) to the conduction band (CB) [74, 75]. Simultaneously, e^-/h^+ undergo recombination, which reduces quantum yield. This recombination rate is affected by many factors related to photocatalyst structures and surface modification [76].

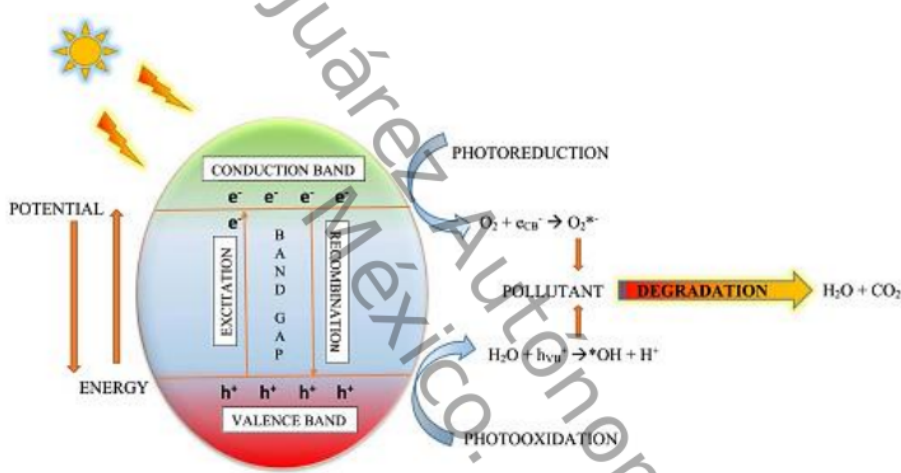


Figure 3. Primary processes in semiconductor photocatalysis.

For key reactions involved in photocatalytic oxidation, see Table 2 [77]. Equation 1 (photoexcitation) explains the semiconductor (where MO_x is a metallic oxide) activation by light ($h\nu$) [78]. The formed $HOO^{•}$ (Equation 5) can lead to the formation of H_2O_2 and $HO^{•}$. Through this way, the recombination of electron-hole gets effectively inhibited and the lifetime of positive holes is prolonged. The generated radicals (mainly including $HO^{•}$ and $O_2^{•-}$) in solution are very efficient non-selective oxidizers, which result in the oxidation and eventual mineralization of organic compounds [79].

Table 2. The reactions involved in the photocatalytic oxidation process for the degradation of organic pollutants.

Reactions	Eq. No.
Photoexcitation: $MO_x + h\nu \rightarrow h^+ + e^-$	1
Oxidation of hydroxyl: $OH^- + h^+ \rightarrow \cdot OH$	2
Oxygen ionosorption: $O_2 + e^- \rightarrow O_2^-$	3
Ionization of water: $H_2O \rightarrow OH^- + H^+$	4
Protonation of superoxide: $O_2\cdot^- + H^+ \rightarrow HOO\cdot$	5
Electron scavenger: $HOO\cdot + e^- \rightarrow HOO^-$	6
Formation of H_2O_2 : $HOO^- + H^+ \rightarrow H_2O_2$	7
Formation of $\cdot OH$: $H_2O_2 + e^- \rightarrow \cdot OH + OH^-$	8
Pollutant + $\cdot OH \rightarrow$ degradation products	9
Pollutant + $h^+ \rightarrow$ oxidation products	10
Pollutant + $e^- \rightarrow$ reduction products	11

The photocatalytic oxidation of some organic species often proceeds via adsorption of the contaminant on the surface of the catalyst, followed by direct subtraction of the contaminant's electrons by positively charged holes. Another possible oxidation occurs with $\cdot OH$ radicals, which are generated from the water of the aqueous environment. Even though both reactions may proceed simultaneously, the leading mechanism will depend on the physicochemical properties of the contaminant [80].

If these e^-/h^+ pairs are not scavenged rapidly after photoexcitation, they combine within picoseconds and neutralize, a phenomenon known as recombination.
8 Recombination gives rise to dissipation of energy and hence results in reduction of quantum efficiency. This phenomenon may take place either on the surface or in the bulk of the catalyst due to several reasons attributing to defects in the crystal [81].

Several semiconductors (e.g., TiO_2 , BiO , ZnO , Al_2O_3 , SnO_2 , SiO_2 , In_2O_3 , WO_3 , ZnS , Fe_2O_3 , CdS , $SrTiO_2$, WO_2 , $\alpha-Fe_2O_3$ etc.) have emerged as good photocatalyst for wastewater treatment [82]. Various techniques have been employed to make the catalysts be able to absorb a photon in the visible light region and have a low electron-hole recombination rate. To name a few, all of the following techniques,
12

such as doping, non-metals doping, coupling with others semiconductor, co-doping and surface modification via organic materials have been attempted [83].

It is well known that the effectiveness of TiO_2 as a photocatalyst owns to its crystal phase, particle size, specific area, pore structure, chemical stability, low cost and non-toxicity [84]. Moreover, its wide band gap energy (ca. 3.0 eV for rutile and 3.2 eV for anatase) means that only 5% of the solar spectrum can be used [85].

Activated under UV irradiation TiO_2 has been used as photocatalyst for the degradation of MB. Results showed that the degradation efficiency increased with increasing the pH of the solution and decreasing the initial dye concentration. Even though, increasing the catalyst loading up to 1 g L^{-1} showed an improvement in the degradation efficiency, this deteriorated with a further increase in the catalyst loading. A complete decolorization of 10 ppm MB solution was achieved in the solution at pH 7 with a catalyst loading of 1 g L^{-1} [86].

Moreover, the photocatalytic activity of ternary nanocomposites based on titanium dioxide, ferric oxide, and reduced graphene oxide ($\text{rGO-Fe}_3\text{O}_4-\text{TiO}_2$) has been evaluated under the degradation of MB. About 94% of the dye was degraded from the wastewater. The enhancement of this ternary system in the photocatalytic activity was attributed to the efficient separation of charge carriers from TiO_2 to rGO under light and the initiation of photo-Fenton reaction due to the incorporated Fe_3O_4 [87].

17

Another work showed a hybrid system integrating a series of unit processes such as a conventional TiO_2 photocatalytic reactor as well as microwave and UV radiation. The decomposition rate of 4-CP was calculated with respect to the pH, hydrogen peroxide level, and oxygen gas injection. Results showed a significant cooperation effect was also observed in the combined processes. Four intermediates were reported to be generated through hydroxylation and dechlorination in the proposed photocatalytic pathway [88].

As an effort to improve their ability to absorb visible light and photocatalytic performance, Nd^{3+} -doped TiO_2 nanoparticles were synthesized. The complete

degradation of 4-CP was reached within 60 min under visible light, implying that doped nanocomposites would be very useful for treating wastewater by sunlight through the AOP's [89].

On the other hand, bismuth-based compounds have taken much attention in photocatalysis due to its distinctive electronic structure. Particularly, β -Bi₂O₃ is a potential candidate as a visible-light driven photocatalyst owing to its narrow band gap of 2.85 eV [90]. The orbital hybridization between Bi 6s and O 2p in Bi₂O₃ allows the photogenerated holes to move on the valence band, which obstructs the recombination of photogenerated e⁻/h⁺ pairs to a certain degree [91].

Bi₂O₃ on the Mg/Al layered double hydroxide was prepared and modified with Pd(II) (Pd(II)-Bi₂O₃/RLDH). The as-prepared Pd(II)-Bi₂O₃/RLDH exhibited an efficient photocatalytic activity for the degradation of MB under visible light irradiation, attributed to its narrow band gap of 2.19 eV. Consequently to the increment of Pd content, the Pd particles agglomeration increased, the photocatalyst surface area was reduced and the efficiency decreased [92].

Following with the degradation of MB, a Bi₂O₃/g-C₃N₄ photocatalyst was prepared and evaluated. The results showed that the photoexcited e⁻ in the CB of Bi₂O₃ and photogenerated h⁺ in the VB of g-C₃N₄ combined quickly, so the photoexcited e⁻ in the CB of g-C₃N₄ and h⁺ in the VB of Bi₂O₃ participate in redox reactions. Hence, it exhibited a rate constant of MB photocatalytic degradation about 3.4 times higher than g-C₃N₄ under visible light illumination [93].

Additionally, modified Bi₂O₃/g-C₃N₄ composites were evaluated by degradation of 4-CP under visible light irradiation. The results agreed that the Bi₂O₃/g-C₃N₄ composites showed higher photocatalytic activity than Bi₂O₃ and g-C₃N₄, respectively. Also, this enhancement could be attributed to the suitable band positions between Bi₂O₃ and g-C₃N₄, which leads to a low photogenerated e⁻/h⁺ pairs recombination [94].

Among these, Fe_2O_3 , has demonstrated to be another promising candidate for photocatalytic applications due to its narrow band gap of about 2.2 eV. It can absorb light up to 600 nm collecting up to 40% of the solar spectrum energy. Also, Fe_2O_3 is stable in most aqueous solutions ($\text{pH} > 3$) [10]. Since the faster recombination rate of photogenerated charge limits its application, different approaches such as morphological controlled synthesis, doping and compositing process have been applied to improve its photocatalytic performance [95].

Materials based on Fe_2O_3 and activated carbons (Fe-ACs) were evaluated by degradation of MB under UV illumination. The effects of Fe content were investigated, reaching a photodegradation up to 26% within 120 min of reaction. The results shown that the increase of the Fe content, the absent of hydrogen peroxide in operation, the low Fe filtering near neutral pH, and the formation of no sludge affected significantly the photodegradation rate constants of the Fe-AC samples [96].

Recent studies indicate that Fe_2O_3 is a good candidate to couple with SnO_2 to compose heterojunction structures for photocatalytic degradation of pollutants. To improve its photocatalytic activity, a novel $\text{Fe}_2\text{O}_3/\text{SnO}_2$ nanobelt was fabricated. The results showed that the MB degradation rate constant on the $\text{Fe}_2\text{O}_3/\text{SnO}_2$ is approximately 12 times to that of Fe_2O_3 . This could be attributed to the direct charge transfer pathway of the well-formed heterojunction structure of $\text{Fe}_2\text{O}_3/\text{SnO}_2$ and the high surface area of the uniform nanobelts [97].

In 2017, nanostructured Fe_2O_3 thin films were deposited onto fluorine doped tin oxide coated glass substrates. Even though optical study showed a variation on the band gap energy of Fe_2O_3 films from 2.19 to 2.35 eV, the synthesized Fe_2O_3 catalyst was used for the degradation of 4-CP, which reached 50% under sunlight illumination after 240 min [98].

2.3 BiFeO₃ as photocatalyst

A perovskite structure is any compound that has the same crystallographic structure as the perovskite mineral (CaTiO_3) and generic formula ABX_3 (Figure 4) [99]. Ideally, the perovskite structure can be illustrated as cubic, where A and B are cations of different size and X is the anion (usually oxygen), which bonds to both. A is a monovalent, divalent, or trivalent metal and B a pentavalent, tetravalent, or trivalent element, respectively [100].

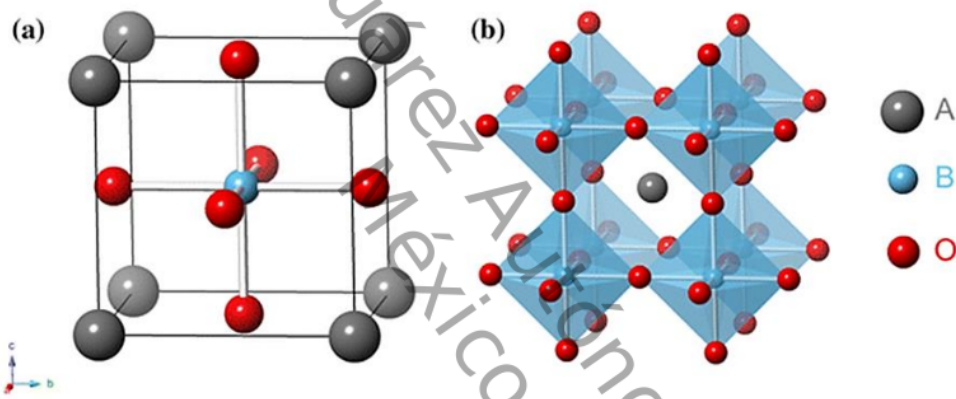


Figure 4. Schematic of ABO_3 perovskite structure; a) lattice and b) polyhedrons.

There are two geometrical packings to visualize the perovskite structure, as a three-dimensional framework of BO_6 octahedra, and as a cubic closed-packed arrangement of A and O ions, with the B ions filling the interstitial positions [101].

15

The B atom has 6-fold coordination number and the A atom has 12-fold coordination number; the A site cation is slightly larger than B cation. Atom A is found at the cube corner position and B is at the body center while oxygen atoms are at face-centered positions but O is the oxygen ion has the ratio of 1:1:3 [102].

In most cases, perovskites have a distorted type of cubic structure. These distortions are incredibly large and complicated [103]. The possibility of preparing multicomponent perovskites by either partial substitution of metal cations in A or B sites or inserting metal oxides into a layered structure allows researchers to explore and modulate the crystal structures and the related physicochemical and catalytic properties of the perovskite oxides [104,105].

According to the literature, the main mechanisms of distortion can be classified into five types: (1) distortion of the BX_6 octahedron; (2) off-center displacement of the B cations in the BX_6 ; (3) tilting of the octahedra, which is typically caused by an A cation since it is too small to be located at the cuboctahedral site; (4) assembling of more than one kind of cation, A or B, or more than one kind of vacancy; and (5) ordering of more than one kind of anion or vacancy. These properties are significant in many applications that use perovskite materials [106].

In the past few decades, a wide range of perovskite photocatalysts have been developed for water splitting and organic pollutant degradation under UV or visible light irradiation [107]. These representative examples and brief experimental results on them are summarized according to their structures, which can be classified into five groups: ABO_3 -type, $AA'BO_3$, $ABB'O_3$, $AB(ON)_3$ -type, and $AA'BB'O_3$ -type [105].

It is well known that the ABO_3 -type perovskite bismuth ferrite ($BiFeO_3$; BFO) (Figure 5) [108] exhibits high ferroelectric and magnetic properties at room temperature as well as very high ferroelectric Curie point and G-type antiferromagnetic Neel temperature [109]. Hence, the main applications of BFO perovskites concern magnetic disk drives, magnetic memories, magnetic hybrid technology, magnetic sensors, microelectronics and telecommunication applications [110,111]. Nevertheless, researchers have found that BFO can be used also in photocatalysis for the degradation of organic pollutants present in wastewater.

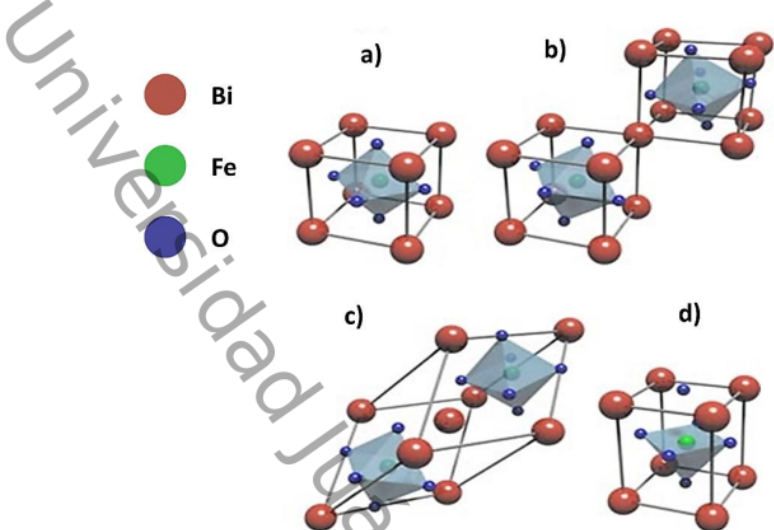


Figure 5. Structures of BiFeO₃. (a) The cubic perovskite unit cell. (b) Two pseudo-cubic cells with cation shifts and octahedra rotations (c) the rhombohedral cell. (d) The highly distorted tetragonal-like phase of BFO.

The lattice parameters of the BFO are shown in Table 3. The unit cell of bismuth iron oxide can also be described in hexagonal frame of reference with lattice parameters $a, b = 5.58\text{\AA}$ and $c = 13.90\text{\AA}$. Bi³⁺ and Fe³⁺ have both six-fold coordination, in which Bi³⁺ ions occupy the cubic-octahedral positions and Fe³⁺ ions in octahedral coordination [112, 113]. BFO is reported to possess a distorted perovskite structure with space group R3c at room temperature in a rhombohedral system with a moderate room-temperature band gap near or in the visible range, which is considerably lower than most other ABO₃ perovskites [114,115].

BFO as a semiconductor perovskite with optical band gap of ~2.2 eV has significant potential for the photoinduced water oxidation [116]. The band bending of BFO particles especially in heterogeneous structures affects the separation of photoexcited electron-hole entities in the space charge region. Thus, the narrow band gap and low recombination of charge carriers in BFO are key parameters that play a substantial role in photoactivity [117].

Table 3. Structures parameters of BiFeO₃.

Structure parameters	Values
Space group	R3c (n° 161)
Cell parameters	$a = b = 5.5870 \text{ \AA}$
	$c = 13.8898 \text{ \AA}$
	$\alpha = \beta = 90^\circ$
	$\gamma = 90^\circ$

It is known that the particle morphology plays an important role on the photocatalytic performance of BFO. However, it is important to mention that in most cases the kinetics of phase formation makes difficult to obtain BFO particles with single crystalline phase, nanoscale size and favorable morphology [118]. Therefore, synthesizing single crystalline BFO nanoparticles with favorable morphology remains as a challenge to achieve.

In order to obtain a comparative morphology between the conventional and more complex methods, the solid state reaction, co-precipitation, sol-gel, ultrasound, hydrothermal and Pechini methods have been studied during the last few decades for the preparation of perovskite oxides [119].

2.3.1 Methods of synthesis

Several methods, such as hydrothermal, sol gel, and solid-state reaction have been employed to synthesize polycrystalline perovskite materials. Usually, the precursors are simple binary oxides or salts altered at a relatively high temperatures [120]. The method of synthesis selected should be fitted to the desired properties of the material in the final application.

Hydrothermal synthesis is one of the most promising method for the fabrication of nanostructures with high crystallinity, high purity, and narrow particle size distribution at low temperature [121]. It has been shown that the concentration of reagents, the reaction temperature, the reaction time and the surfactants are important factors in influencing the structural growth of the products [122].

Single crystalline BFO nanoparticles with different particle morphology and size could steadily be obtained by modified hydrothermal method. The as-prepared BFO particles were mainly in a square or rectangle-like morphology. The results showed that BFO nanoparticles synthesized at 200 °C for 3 h with spherical shape have a small particle size and low band gap of ~1.97 eV, leading to a higher photodegradation of methylene orange (MO) under visible light irradiation [123].

11

In contrast, the sol-gel process is based on the hydrolysis and condensation of molecular precursors, performed under mild conditions. There are two chemical ways to form the solid phase network: the metal-organic route, using metal alkoxides in organic solvents and the inorganic route, using metal salts (chlorides, nitrates, sulfides, etc.) in aqueous solutions [124]. The sol-gel process begins usually with the alcoholic solution of a metal alkoxide precursor. The condensation of hydroxyl groups, produced by the hydrolysis of metal alkoxides, form a three-dimensional network. The two simultaneous reactions produce alcohol and water as sub-products. The process ends with the formation of a metal oxide network [125].

This method has several advantages over other techniques. It produces uniform sizes, well-distributed components, and high purity in the final powder. The physicochemical properties of the BFO particles strongly depend on the hydrolysis and drying steps [126]. It is reported that using metal nitrates and polyethylene glycol as surfactant and dispersant, are crucial to obtain single-phase BFO particles with a perovskite structure and sizes ranging from 80 to 120 nm. It was found that the precursor concentration and the annealing temperature have significant influences on the impurity, particle size and band gap (~2.1 eV) of BFO powders. The synthesized samples exhibited efficient photocatalytic degradation on visible-light of MO as well [127].

Moreover, BFO perovskites have been synthesized at 600 to 800 °C of calcination by this process, obtaining nanoparticles with a crystallite size of 60–70 nm. The obtained perovskite catalysts exhibited high stability and efficient catalytic activity in heterogeneous Fenton-like oxidation of phenol at neutral conditions [128].

Nevertheless, impurity, particle size and agglomeration are challenges that must be solved for the synthesis of BFO by those methods. And the effects of synthetic parameters such as temperature and precursor concentration on the product remain still not clear and the surface state of the product is not supported.

The Pechini process (Figure 6) results as a modified sol-gel method, where the metal salts are dissolved in a mixture of citric acid and ethylene glycol (EG) to form a solution containing metal–citrate chelate complexes. This solution is heated to produce a polyester network containing the metallic ions homogeneously distributed. Finally, the material is calcinated to combust the organic matrix and form the metal oxide product at adequate temperatures [129].

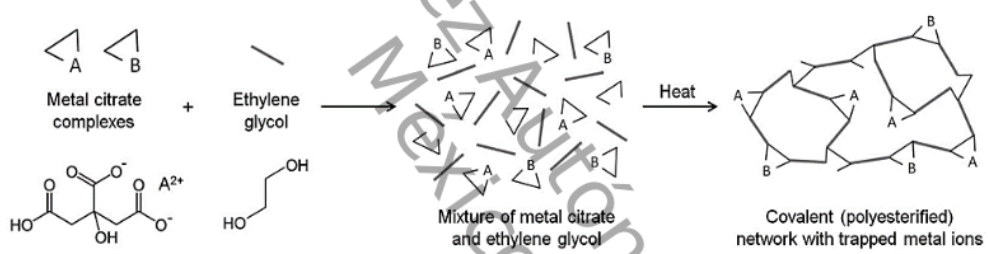


Figure 6. Schematic of the Pechini process to obtain metal/organic gels.

Recently, single-phase BFO nanoparticles have been successfully synthesized with average size ~64 nm by using formic acid as a chelating agent and EG as a polymerizing agent through a modified Pechini process. In this process the formic acid acts as a buffer enabling the slow hydrolysis while EG coordinates with metal cations to form polymeric complexes and prevent their mobilization. This immobilization remains as a key step in forming single-phase BFO perovskite, since it can reduce segregations of specific metals and maintain stoichiometry during calcination [28].

2.3.2 Doping

Recent works have proved that modifying the A-site Bi^{3+} ions with rare-earth ions or divalent ions can lead the improvement on the properties of BFO compounds. Firstly, the amount of partial substitution at the A sites in BFO has a strong influence on the formation of perovskite phase, especially in the case of substitution by bivalence or ¹⁶ tetravalence ions. If the partial substitution at the A sites is too high, there will be other oxides formed and the expected perovskite structure cannot be obtained. In contrast, if the partial substitution at the A sites is too low, the raising effect could not success [130].

Since a few A-site compatible rare earths ions such as La, Gd and Nd have considerably higher bond enthalpies with oxygen than the Bi–O bond, they are often added to BFO in order to minimize carrier donating/trapping vacancies via stabilizing the oxygen in the lattice. Hence, compensation of vacancy carriers generated via doping can lead to a relatively less free carrier densities BFO [131].

La doped BFO powders have been prepared by microwave hydrothermal method and a microwave route. The results showed a transformation at the sharp single peak ($2\theta = 32^\circ$) of BFO when La content was increased. The distortion of the crystal structure of BFO ceramics by the introduction of La could lead to the formation of more short-range charge carriers. In addition, a relation between the increment of magnetization and La contents was observed, which could be ascribed to two aspects: the fact that La possessing magnetic property and the introduction of La could change the polarization of the samples [132].

Another example is the substitution with magnetic Gd^{3+} ions to improve the structural properties of BFO. The structural analysis revealed the presence of rhombohedral structure in undoped and 5% Gd doped BFO ceramics. Even though the coexistence of two phases was confirmed indicating the phase transition from rhombohedral to orthorhombic at doping higher than 10%; a suppression of impurity peaks was observed showing the successful incorporation of Gd^{3+} ions in the BFO crystal structure [133]. In contrast, single-phase Nd doping BFO nanopowders synthesized

by sol-gel method showed a structure transition from rhombohedral to triclinic and finally to tetragonal structure to become microwave absorbing materials with high performance [134].

In the last decades, most of the investigations of A-site alkaline ions doping have been focused on the effects and influences on the structural properties of BFO. For example, Ca substitution was confirmed to change the local distortion and strain on the R3c and P4mm co-existing phases which is reflected in physical properties of the system. The mechanism based on electronic conduction as a consequence of instinctively produced oxygen vacancies acting as donor of impurities to compensate Ca acceptors and maintain a steady Fe^{3+} valence state suggested a novel platform for highly efficient ferroelectric applications [135].

Some other studies have indicated that successfully synthesized by sol-gel method Sr-doped BFO nanoparticles have presented rhombohedral structure. Results revealed the formation of highly agglomerated nanoparticles with reduced size, which tend to grow into well-developed nanoparticles with increasing the calcination temperature. Owing to the oxygen vacancies created due to the charge imbalance and enhanced lattice strain of heterovalent Sr-doping, the magnetization was enhanced. The formation of oxygen vacancies by Sr-doping in the lattice reduced dielectric constant which decreased while particle size revealed better obstruction of charge carriers [136].

On the other hand, Ba doping has not showed any evidence of structural transition with doping up to 20% Ba^{2+} ions. Therefore, results have revealed an improvement in the magnetic properties of the BFO nanoparticles. The basis of this increase in the magnetization suggested the presence of Fe^{2+} or Fe^{4+} states due to structural changes caused by the Fe-O-Fe bond angle and defects [137].

To date, metal ion doping has been regarded also as an efficient method to improve the photocatalytic activity of BFO. In 2017, Sm-doped BFO nanoparticles were prepared by a sol-gel method and evaluated for MO photodegradation. Results demonstrated that the band gap of the prepared BFO nanoparticles significantly

decreased when increasing Sm doping concentration. This optimal photocatalytic performance of the Sm-doped BFO photocatalyst was ascribed to the increased optical absorption as well as the efficient migration and separation of photogenerated electron-hole pairs derived from Sm dopant trapping level in BFO [24].

Likewise, high-purity Y-doped BFO nanoparticles were successfully fabricated by a facile green route. The synthesized samples exhibited a rhombohedral perovskite structure with a particle size in the range of 80 – 90 nm. Also, a diminution of band gap energy from 2.07 to 2.05 eV as the concentration of Y dopant increased was observed. The obtained products were evaluated on the photocatalytic degradation of MB under direct sunlight. There was a remarkable improvement in the photocatalytic activity attributed to the strong absorption of visible light and the effective separation of photoinduced e^-/h^+ pair [138].

The effective Sr^{2+} doping influences have been also evaluated on the photocatalytic properties of BFO for the degradation of MB. The best and optical photocatalyst was confirmed by its weak photoluminescence intensity. In addition, the photocatalytic property of Sr-doped nanofibers was much higher (up to 85% of degradation achieved) than that of nanoparticles with the same constituent attributed to their unique one-dimension fibrous structure [139].

There are more degradation-resistant compounds in industrial wastewater than organic dyes, such as phenolic compounds. Subsequently, to remove phenol in industrial wastewater, La-doped BFO photocatalysts synthesized by a facile sol-gel method were evaluated under simulated sunlight irradiation. The introduction of La effectively suppressed the generation of an impurity phase as reported before. A degradation rate of 96% was reached after 180 min of reaction. The 15% La-doped BFO photocatalyst exhibited the best activity and good recycling stability. The existence of $\cdot OH$ radicals as primary active species by adding different scavengers during the photodegradation of phenol was confirmed [140]

Recently, Pd-doped BFO composites were effectively prepared by hydrothermal method. The Pd-BFO composites showed much higher photocatalysis performance

(~99% of degradation achieved) than the undoped BFO under direct sunlight for phenol after 240 min of reaction. The improved photocatalytic performance was ascribed to the creation of heterojunction among the metallic Pd and BFO, which led to the generated •OH radicals participate in the degradation of phenolic compounds. Besides, the photocatalytic process proved to be more economical by using Pd-BFO as a photocatalyst [141]

Since the stability of the crystalline phase by promising Pechini method of synthesis has been confirmed and doping with Ca^{2+} and Sr^{2+} cations for the photocatalytic degradation of phenols has not been reported yet, the main approach of the present work is doping perovskite-type BFO with cations, as well as evaluating their catalytic activity on photocatalysis.

Chapter 3: Synthesis and Characterization of the Materials: Methods and Techniques

Universidad Juárez Autónoma de Tabasco.
México.

3.1 Synthesis of $\text{Bi}_{1-x}\text{A}_x\text{FeO}_3$

The following reagents were used for the synthesis without additional purification: bismuth(III) nitrate pentahydrate ($\text{Bi}(\text{NO}_3)_3 \cdot 5\text{H}_2\text{O}$) (Sigma-Aldrich, 98.0%), iron(III) nitrate nonahydrate ($\text{Fe}(\text{NO}_3)_3 \cdot 9\text{H}_2\text{O}$) (Sigma-Aldrich, 98.0%), calcium nitrate tetrahydrate ($\text{Ca}(\text{NO}_3)_2 \cdot 4\text{H}_2\text{O}$) (Sigma-Aldrich, 99.9%), strontium nitrate ($\text{Sr}(\text{NO}_3)_2$) (Sigma-Aldrich, 99.9%), ethylene glycol (EG) ($\text{C}_2\text{H}_6\text{O}_2$) (Sigma-Aldrich, 99.8%) and citric acid ($\text{C}_6\text{H}_8\text{O}_7$) (Sigma-Aldrich, 99.5%).

$\text{Bi}_{1-x}\text{Ca}_x\text{FeO}_3$ and $\text{Bi}_{1-x}\text{Sr}_x\text{FeO}_3$ (for $0 < x < 0.15$) powders were synthesized by a modified Pechini method. A schematic diagram (Figure 7) shows the successive stages for the synthesis of BFO particles. In order to prepare the initial solutions, stoichiometric quantities of Bi, Fe, and dopant cations (Ca^{+2} , Sr^{+2}) precursors were separately dissolved in the presence of a complexing agent (EG) (1:16 %mol) and a volume of citric acid (1:4 mol%) under magnetic stirring at room temperature (25 °C).

Once the solutions were prepared, they were mixed to initialize the polyesterification. Prepared sols were kept at 90 °C to evaporate the solvents and to accomplish the polyesterification, brown foamy-like viscous gels were obtained. Then, the temperature was raised up to 350 °C for 1 h at a heating rate of 3 °C min⁻¹ to eliminate the water residuals and dry the gels until they turned into dry resins. After, these dry resins were homogenized and milled to obtain powders. To start the pyrolysis process and to get rid of the organic part, calcination was carried out at 600 °C for 1 h at a heating rate of 3 °C min⁻¹ to obtain crystallized undoped and doped BFO nanoparticles.

Finally, the obtained powders $\text{Bi}_{1-x}\text{Ca}_x\text{FeO}_3$ and $\text{Bi}_{1-x}\text{Sr}_x\text{FeO}_3$ containing a concentration of $x = 0 < x < 0.15$ were named BFO, BCaFO-05, BCaFO-10, BCaFO-15, BSrFO-05, BSrFO-10 and BSrFO-15, respectively.

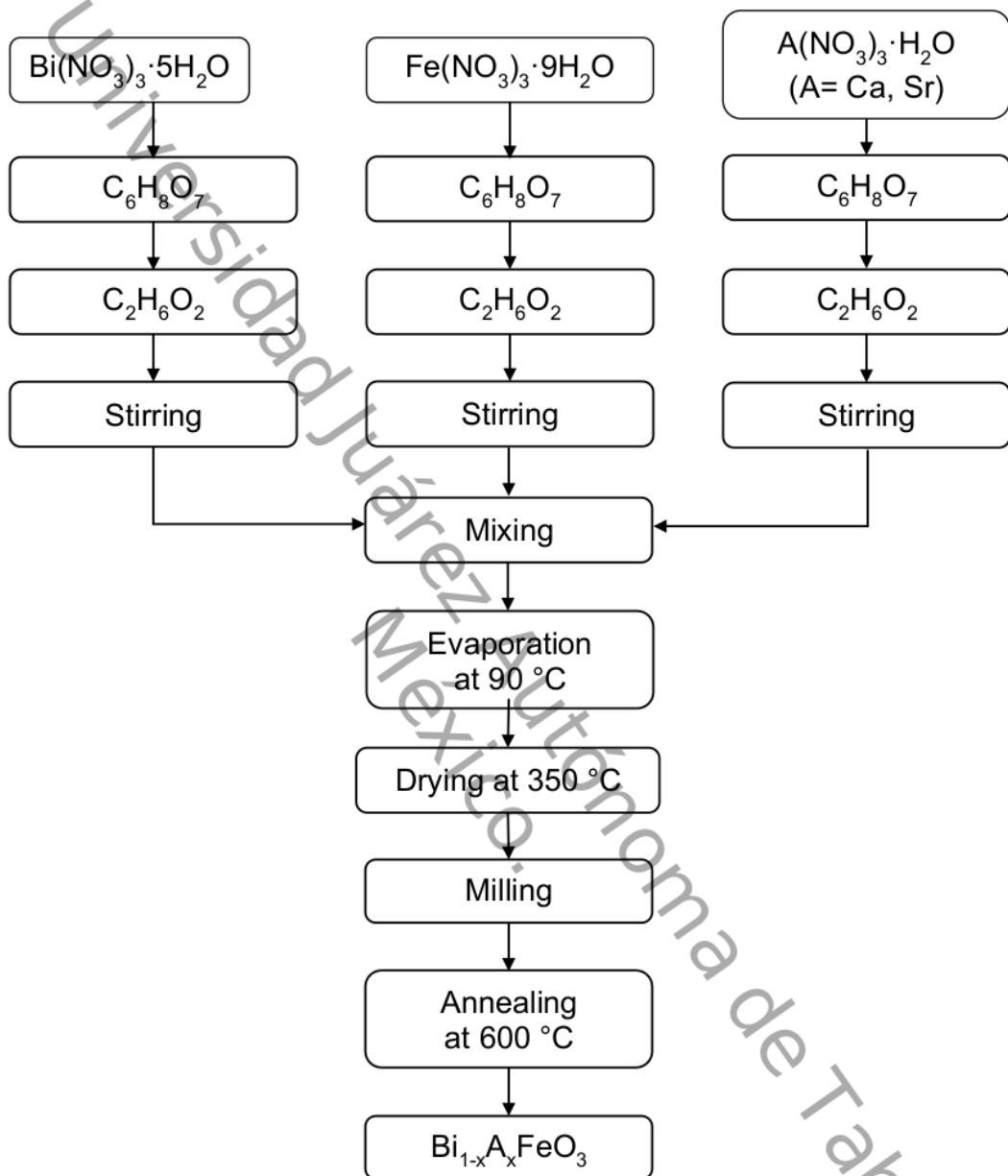


Figure 7. Scheme of the modified Pechini method followed in this study.

3.2 Catalyst characterization

The synthesized powders were characterized by the following physicochemical techniques. A brief description of each technique carried out is presented in the Annexes section.

3.2.1 X-Ray Diffraction (XRD)

The X-Ray Diffraction technique commonly provides information about structure type, crystalline phases, average crystal size, crystallinity, and crystal defects. XRD peaks are produced by constructive interference of a monochromatic beam of X-rays scattered at specific angles from each set of lattice planes in a sample. The distribution of atoms within the lattice determines the peak intensity.¹⁹

Crystal structure and phase were examined by using XRD technique on a (Bruker D2 Phaser, coupled with Lynxeye detector) diffractometer. Incident X-ray radiation was CuK α_1 ($\lambda = 1.5406 \text{ \AA}$) and CuK α_2 ($\lambda = 1.5444 \text{ \AA}$), respectively. The scanned 2θ range was $20^\circ - 80^\circ$. The step size for data collection was 0.02° with a collection time 2 s at each step.

3.2.2 Rietveld Refinement

The experimental step-scanned values can be fitted to calculated values by a least-squares refinement. The Rietveld method operates with a whole pattern fitting algorithm where all profiles for each phase are considered as known, and an available model for each crystal structure. Using all reflections in a pattern minimizes the ambiguity in derived weight fractions and the effects of preferred orientation, primary extinction, and nonlinear detection systems.

Crystal structure and cell parameters were fitted using Rietveld analysis on TOPAS software version 5.0. In the present approach the Rietveld refinement was carried out on to collect information about unit cell parameters, atom positions, as well as to determine the phase composition of the samples.

3.2.3 Scanning Electron Microscopy (SEM)

Scanning electron microscopy (SEM) is a technique commonly used for observing and analyzing the microstructure and morphology of catalysts. The sample is irradiated with a finely focused electron beam systematically scanned across the surface of the specimen, resulting in a wide range of signals that reveal information about the sample including morphology and chemical composition.

Microstructures of as-prepared sample powders were inspected under a scanning electron microscope Jeol model JSM-6010LA+ operated at 20 kV.

3.2.4 UV-Vis Diffuse Reflectance Spectroscopy (DRS)

UV-Visible (UV-Vis) spectroscopy is a useful technique for the determination of the absorption properties of materials. Particularly, in the case of semiconductors, measurements of diffuse reflectance allow to estimate the band gap energy value. This parameter determines the light energy that may be used to activate the solid catalyst. Additionally, the information provided by the diffused reflectance technique is about the electronic properties of a material and the coordination and oxidation state of transition metals cations.

To study the optical properties and to calculate the band gap of as-prepared samples, the UV–Vis diffuse reflectance spectra (DRS) were recorded using a UV–Vis spectrophotometer (Shimadzu UV-2600) with an integrating sphere assembly in 200–800 nm region.

3.2.5 X-Ray Photoelectron Spectroscopy (XPS)

X-ray photoelectron spectroscopy (XPS) is a surface analysis technique that is based on energy spectrum measurements of photoelectrons emitted from a material surface under irradiation with a monochromatic soft X-ray radiation. This technique typically provides information on the qualitative and quantitative elemental composition and on the electronic state of each element in the sample surface.

Surface conditions of the samples were analyzed by XPS (PHI 5800 ESCA system (Physical Electronics) using monochromatic Al K α radiation (1486 eV)). Spectra were recorded for the selected samples as representative. The XPS data was simulated and fitted using the Xpspeak41 software. The Bi, Fe, Ca and Sr surface concentrations and their ratios were calculated from the measured intensities of the Bi(4f), Fe(2p), Ca(2p) and Sr(3d) signals, using tabulated sensitivity factors and assuming a constant composition of the topmost few layers.

3.3 Probe degradations

The catalytic performance of the prepared photocatalysts was evaluated by the photodegradation of methylene blue and 4-chlorophenol in aqueous solution (30 and 30 ppm respectively). The photocatalytic experiments were carried out into a 250 mL vessel photoreactor. The reaction was directly exposed to natural sunlight irradiation. During the reaction, the cooling water was replaced to keep a constant room temperature. In a typical photocatalytic reaction, 100 mg photocatalyst was added into a 200 mL aqueous solution with air ventilation and magnetic stirring. Before the reaction start, the catalyst was placed into darkness for 30 min to reach adsorption equilibrium. Then, the suspension was irradiated for 180 min. During the photocatalytic reaction, a sampling was taken at 0, 20, 40, 60, 80, 100, 120, 140, 160 and 180 min.

The contaminant concentration was measured by a UV-Vis spectrophotometer using UV-Vis spectrophotometer (Shimadzu UV-2600) at the wavelength of 291 nm and 280 nm for methylene blue and 4-chlorophenol, respectively. The contaminant degradation (D) was calculated by [Equation 12](#).

$$D = \frac{A_0 - A_t}{A_0} \times 100\% \quad 12$$

where A_0 is the absorbance of the contaminant solution before the exposure under solar irradiation, and A_t was after irradiation. A blank test of contaminant solution irradiated without any catalyst was also performed for comparison.

Chapter 4: Characterizations of $\text{Bi}_{1-x}\text{A}_x\text{FeO}_3$: Results and Discussion

Universidad Juárez Autónoma de Tabasco.
México.

4.1 X-Ray Diffraction (XRD)

The XRD pattern of undoped BFO sample calcinated at 600 °C for 1 h is shown in Figure 8. It can be noticed that single-phase BFO was successfully obtained without any secondary phases or impurities and all observed diffraction peaks match well with the powder diffraction file card (JCPDS No. 86-1518 [33]). Although it is well-known that single phase BFO is quite difficult to prepare, the magnified XRD pattern in the range between ~31° and 33° at 2θ (Figure 8b) confirms the formation of the rhombohedral R3c, which could indicate that the method followed in this work was favorable for its synthesis. Consequently, it can be concluded that no structural transition from rhombohedral to orthorhombic or to other phases occurred.

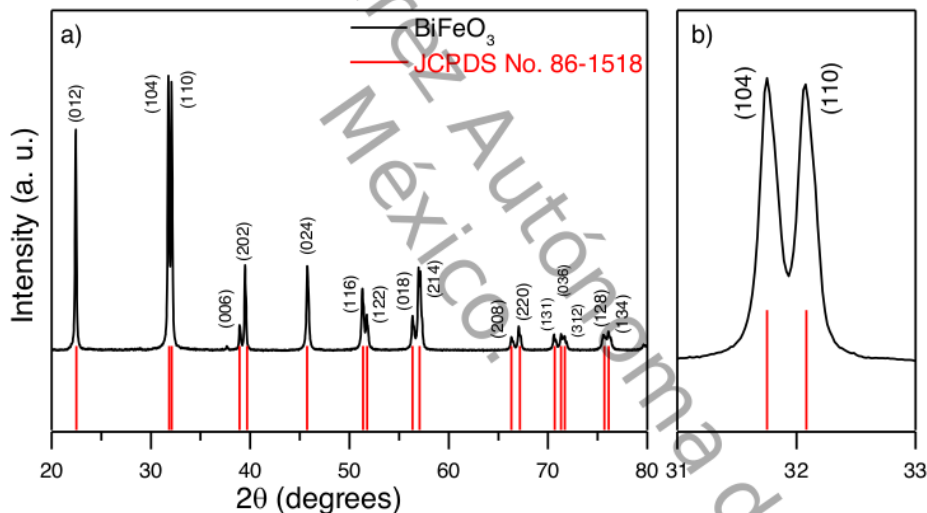


Figure 8. a) XRD patterns for as-prepared BFO NPs; b) patterns of the main peak between 31° and 33° in BFO samples.

The XRD patterns of BCaFO compounds are shown in Figure 9. The results indicate the formation of rhombohedral lattice with R3c space group, as in the undoped BFO sample. However, some extra peaks were detected ~26° - 29° at 2θ for the BCaFO-5 and BCaFO-10 samples, which matched with $\text{Bi}_2\text{Fe}_4\text{O}_9$ (marked with *), according to the JCPDS No. 20-0836 [142] diffraction file card. It can be noticed that these

small peaks disappeared in the BCaO-15 sample, but some minor traces of the Bi_2O_3 phase (JCPDS No. 78-1793 [143], marked with +) were formed.

The (104) and (110) peaks are the main reflections of the BiFeO_3 phase Figure 9b shows that these peaks merged into a single (110) peak with the dopant increasing. Since the ionic radius of Ca^{2+} (1.03 Å) is smaller than that of Bi^{3+} (1.17 Å), the Ca substitution also decreased the lattice distance and thus the unit cell, which can be seen as a shift of the diffraction peaks to larger angles [144,145]. It can be also noticed that no additional peak related to CaO was observed.

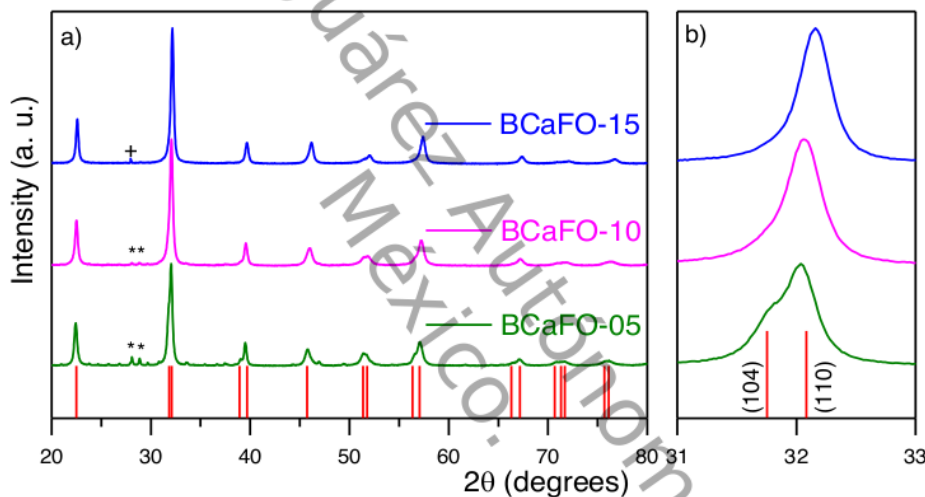


Figure 9. a) XRD patterns for BCaFO-05, BCaFO10 and BCaFO-15 NPs; b) patterns of the main peak between 31° and 33° in Ca doped BFO samples.

The XRD patterns of the BSrFO compounds are shown in Figure 10. The successful formation of the BFO structure (JCPDS No. 86-1518) was confirmed for all the BSrFO samples. Some extra peaks were also detected $\sim 26^\circ - 29^\circ$ at 2θ , related to $\text{Bi}_2\text{Fe}_4\text{O}_9$ (JCPDS No. 20-0836, marked with *).

Similar to the BCaFO samples, the (104) and (110) main peaks of BFO phase also merged into a single peak (Figure 10b) suggesting the successful incorporation of the dopant ion in the crystal structure; however, the peaks shifted slightly to the left

due to the ionic radius of Sr^{2+} (1.18 \AA) under the coordination number 6 is almost the same than that of Bi^{3+} (1.17 \AA) [146].

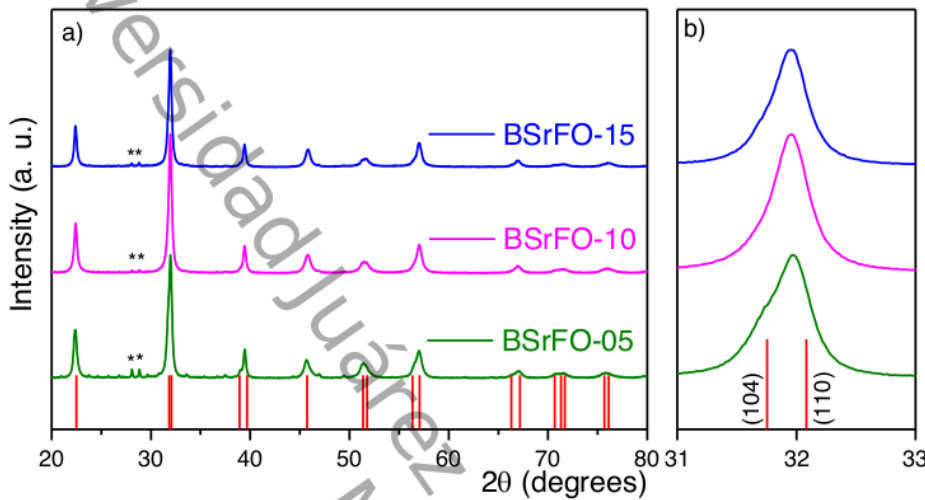


Figure 10. a) XRD patterns for BSrFO-05, BSrFO-10 and BSrFO-15 NPs; b) patterns of the main peak between 31° and 33° in Sr doped BFO samples.

Among the high volatility of Bi at high temperatures during calcination process, the electrons form the 6s orbitals of Bi^{3+} tend to hybridize with 2s and 2p orbitals of oxygen to form a space-filling localized lobe, which might push away its neighboring atoms causing a structural distortion and the formation of secondary phases [147,148]. Hence, it can be inferred that Ca^{2+} or Sr^{2+} ion substitution can stabilize the oxygen octahedron due to the charge compensation by the cation valance state [146,149]. From the present XRD results, this suppression of the Bi volatility and successful stabilization can be correlated to the decrease of the secondary phases when the ion dopant concentration increased.

To date, the amount of secondary phases for the synthesized compounds in this work is smaller as compared to works reported in the literature [136, 139], confirming the promising of the Pechini method. This could be attributed to the fact that in this method of synthesis, citric acid was used to coordinate metal ions (from the metal nitrate solutions) and ethylene glycol was used as a solvent to facilitate the

polymerization process, resulting in the formation of a homogeneous polymer network with metal ions uniformly distributed throughout the organic matrix [150,151].

The average crystallite size (L) of all samples was calculated according to Scherrer's formula (Equation 13) [152]:

$$L = \frac{0.89\lambda}{\beta \cos\theta} \quad 13$$

where λ is the characteristic X-ray wavelength equal to 0.15406 nm, β is full width at half maxima (FWHM in radians) and θ is the angle of diffraction (in radians). The calculated average crystallite size values for BFO, BCaFO and BSrFO powders are summarized in Table 4.

Table 4. Average crystallite size for BFO, BCaFO and BSrFO powders.

Samples	BFO	BCaFO-05	BCaFO-10	BCaFO-15	BSrFO-05	BSrFO-10	BSrFO-15
Average crystallite size (nm)	54.6	24.2	23.7	30.8	26.9	24.8	26.0

The calculated average crystallite size was found to be ~54 nm for undoped BFO, which confirms that the crystal size is in the nanometric range. As it can be seen, the average crystallite size decreases in replacing Bi with any of the two divalent substituents due to the change in ionic size, which causes a reduction in the unit cell volume; however, it increases when the dopant concentration reaches 15 mol% attributed to internal stresses, such as chemical pressure and lattice mismatch. This can be also correlated to the propensity of the crystal structure to suffer phase transformation from rhombohedral to orthorhombic structure with cations substitution [153, 154].

4.2 Rietveld Refinement

The Rietveld method uses a least squares approach to refine a theoretical line profile until it matches the measured profile. Rietveld refinement of XRD patterns was initially performed using the space group R3c for all the samples.

Figure 11 shows the measured, simulated and difference profiles resulted of the Rietveld refinement for the undoped BFO sample. It can be noticed that the observed and calculated profiles successfully matched with the rhombohedral phase with R3c space group.

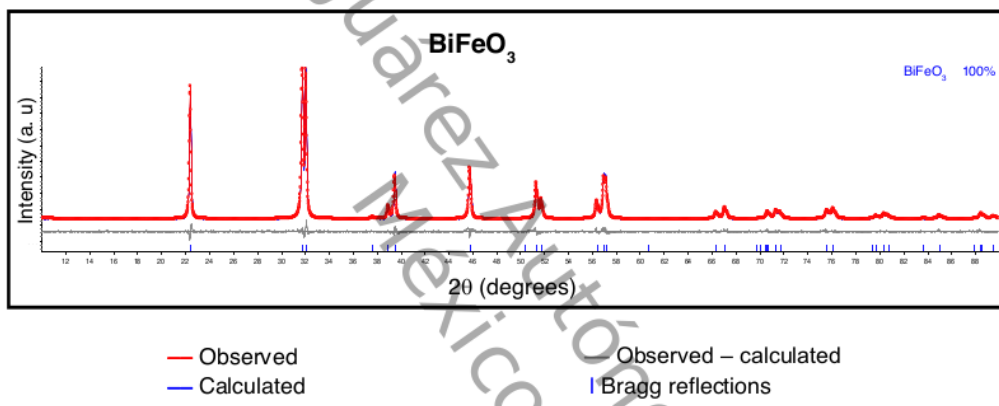


Figure 11. Rietveld refinement of the XRD patterns of undoped BFO sample. The differences between observed (red circles) and calculated (blue line) spectra are plotted (grey line). Bragg reflections are indicated by ticks.

The lattice constants ($a=b$ and c), cell volume (V) and refinement parameters for the undoped BFO sample are presented in Table 5. The relatively small R-values of refinements (R_p , R_{wp} and R_{exp}) and goodness of fitting (GOF) suggest that all the main rhombohedral R3c phase peaks can be refined with good confidence factors between the simulated and measured values of XRD patterns, which confirm the presence of one single crystal phase in well agreement with previous reports [155,156].

Table 5. Refinement parameters of BFO sample.

Sample	Space group	a (Å)	b (Å)	c (Å)	V (Å³)
BFO	R3c (100 %)	5.5775	5.5775	13.8616	373.44199
<i>Conventional Rietveld R-factors</i>					
	<i>R_p</i>	<i>R_{wp}</i>	<i>R_{exp}</i>	<i>GOF</i>	
	5.47	6.96	5.95	1.17	

The Rietveld refinement results of the BCaFO samples are illustrated in Figure 12 and the quantification of phases is summarized in Table 6. For the BCaFO-05 sample, the rhombohedral phase accounts of about 90%, and the orthorhombic phase represents the remaining contribution of about 10%. On the other hand, the contribution of the orthorhombic phase decreases to 7% for the BCaFO-10 sample. For the BCaFO-15 sample, the tetragonal phase was best-fit with contribution reached only less than 1%. The obtained values of GOF ($\text{GOF} = \text{R}_{\text{wp}}/\text{R}_{\text{exp}}$) (≤ 3.32) are in a good agreement with those reported in the literature; hence, it can be concluded that a successful refinement was achieved [135,145].

Usually, the reflections might be partially or completely overlapped, resulting challenging and unusual to estimate the volume contents of individual phases in this type of compounds [157]. However, the quantitative estimation of phases could help to attribute properly the photocatalytic response to the BFO phase.

Table 6. Refinement parameters of BCaFO-05, BCaFO-10 and BCaFO-15 samples.

Sample	Phases (%)			<i>R_p</i>	<i>R_{wp}</i>	<i>R_{exp}</i>	<i>GOF</i>
	BiFeO ₃ (Rhombohedral)	Bi ₂ Fe ₄ O ₉ (Orthorhombic)	Bi ₂ O ₃ (Tetragonal)				
BCaFO-05	90	10		3.84	5.41	1.85	2.93
BCaFO-10	93	7		4.24	6.06	1.82	3.32
BCaFO-15	99.52		0.48	3.87	5.38	1.82	2.96

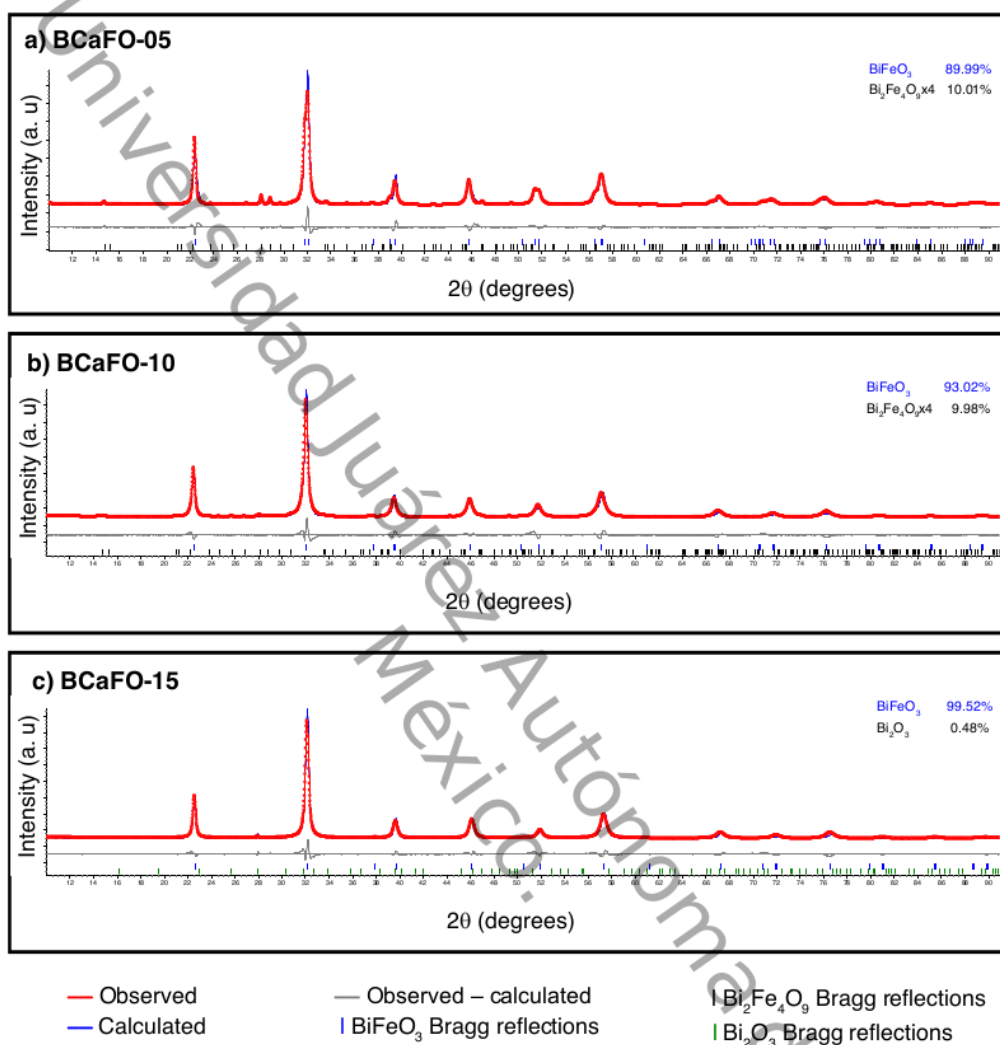


Figure 12. Rietveld refinement of the XRD patterns of a) BCaFO-05, b) BCaFO-10, and c) BCaFO-15 samples. The differences between observed (red circles) and calculated (blue line) spectra are plotted (grey line). Bragg reflections are indicated by ticks.

Figure 13 shows the Rietveld refinement results for the BSrFO samples and the quantification of phases is summarized in Table 7. For the BSrFO-05 sample, the rhombohedral phase dominates with about 87.6%, and the orthorhombic phase represents the remaining ~12.4%. In contrast, the contribution of the orthorhombic

phase decreases to 2.3% and 2.8%, for BSrFO-10 and BSrFO-15, respectively. the obtained values of GOF (≤ 3.96) are in a good agreement with those reported in the literature; hence, it can be concluded that a successful refinement was achieved [136,146].

As discussed previously, the differences between the ionic radius of the dopant and of Bi might mismatch in the lattice causing a structural distortion. With equivalent substituted concentration, the smaller dopant ion will cause larger lattice distortion, as in the case of Ca substitution), which is attributed to a chemical-like pressure effect caused by the smaller radio of the dopant ions [147]. On the other hand, the percentage of a secondary phase with increasing the Sr content as the ionic radius of Sr^{2+} and Bi^{3+} are almost the same.

Table 7. Refinement parameters of BSrFO-05, BSrFO-10 and BSrFO-15 samples.

Sample	Phases (%)		R_p	R_{wp}	R_{exp}	GOF
	BiFeO_3 (Rhombohedral)	$\text{Bi}_2\text{Fe}_4\text{O}_9$ (Orthorhombic)				
BSrFO-05	87.6	12.4	5.05	7.34	1.86	3.96
BSrFO-10	97.7	2.3	4.21	5.92	1.80	3.29
BSrFO-15	97.2	2.8	3.84	5.41	1.80	3.00

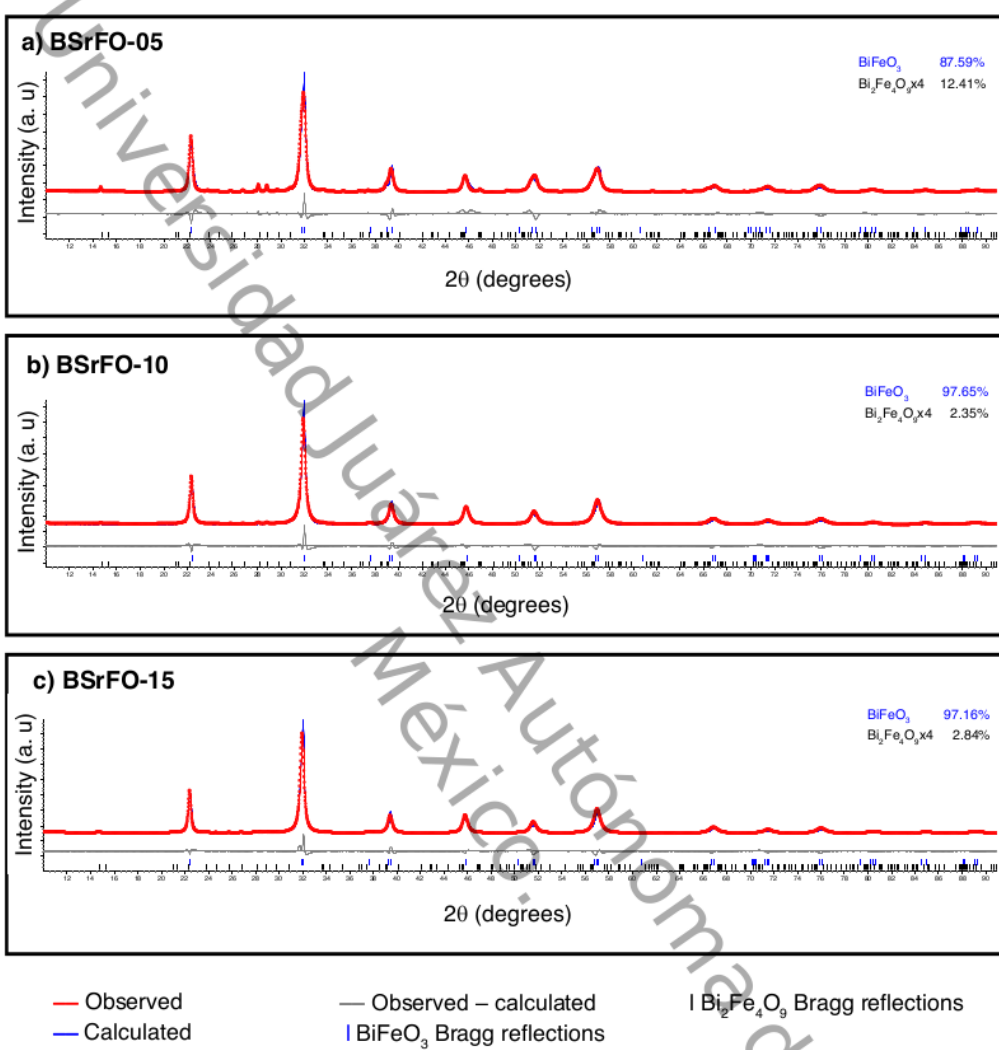


Figure 13. Rietveld refinement of the XRD patterns of a) BSrFO-05, b) BSrFO-10, and c) BSrFO-15 samples. The differences between observed (red circles) and calculated (blue line) spectra are plotted (grey line). Bragg reflections are indicated by ticks.

4.3 Scanning Electron Microscopy (SEM)

SEM was used to investigate the morphology of the prepared samples. Figure 14 shows the SEM images and the EDS analysis of undoped BFO sample. Figures 14a and 14b display aggregated of grains with irregular shapes and agglomerated particles. This could be attributed to the formation of a liquid phase during the synthesis process leading a rapid/discontinuous grain growth [158].

Figure 14d shows the compositional analysis (EDS spectrum) of the typical BFO compound. The elemental peaks of Bi, Fe, and O were confirmed; no other elements were detected in the undoped BFO sample.

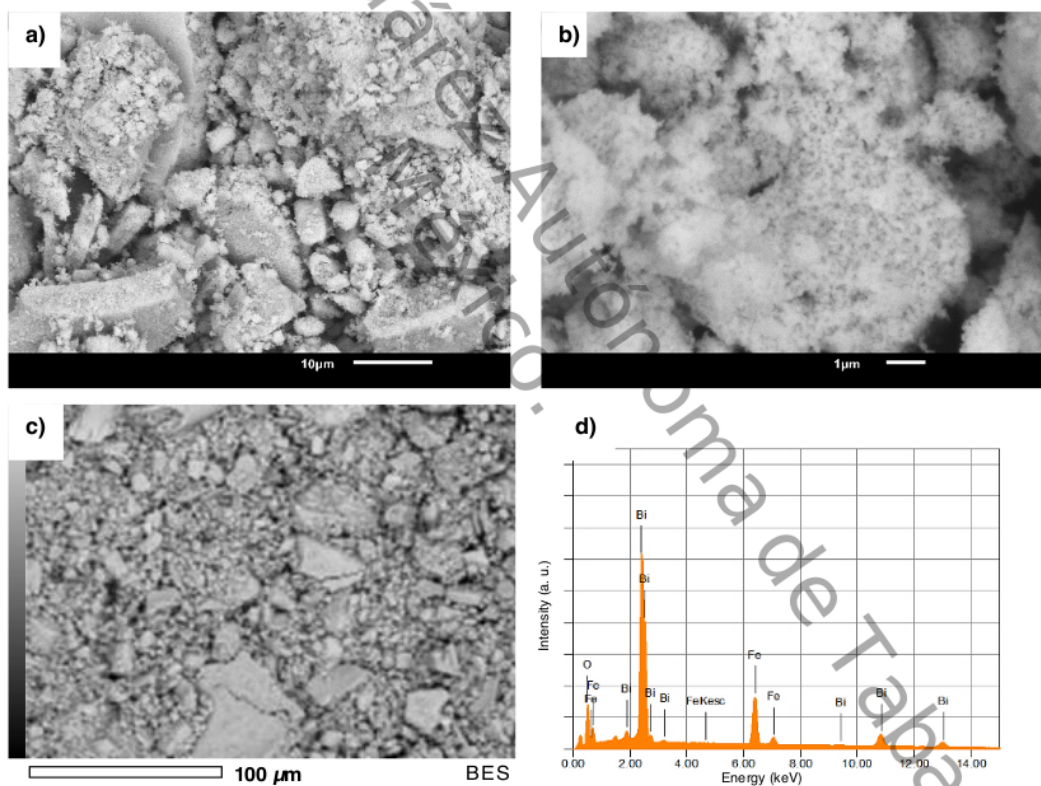


Figure 14. SEM images and EDS spectrum of undoped BFO.

Figure 15 shows the SEM images of BCaFO samples with different content of Ca. Some effects on the morphology of the doped BFO samples with irregular shapes and sizes were observed due to the introduction of Ca dopants. The observed changes in the porosity can be explained by the occupation of certain evaporated A-site by alkaline ions and the substitution of Ca atoms in place of Bi atoms having smaller ionic radius [149]. Figure 16 shows the compositional analysis (EDS spectrum) of the BCaFO samples, where the characteristics peaks of Bi, Ca, Fe, and O are shown. This analysis confirmed the expected amount of the present elements and the successful Ca doping in the prepared BCaFO samples.

Figure 17 shows the SEM images of BSrFO samples with different Sr content. From the micrographs of BSrO samples, no significant influence of Sr doping on the morphology, shape and grain size was observed, but a slight increase of the porosity can be noticed; the latter could be attributed to the synthesis procedure and to the Sr doping [159]. Additionally, Figure 18 shows the compositional analysis (EDS spectrum) of the BSrFO samples. The intensity of the characteristic peaks of Bi, Sr, Fe, and O confirmed the expected amount of these elements in the doped BFO structure.

1 The doping effect with Ca and Sr on the BiFeO_3 structure slightly modified the grain growth of the particles (as the doping content was increased), considering that grain growth depends upon the concentration of oxygen vacancies and diffusion rate of the ions. [160]. The oxygen vacancies would not only come from the volatilization of Bi, but also came from the fluctuation of Fe ions valence state [161], further discussed in the XPS results section. Consequently, the content of Ca or Sr ions on the A-site substitution influences the average size and homogeneity of the grains.

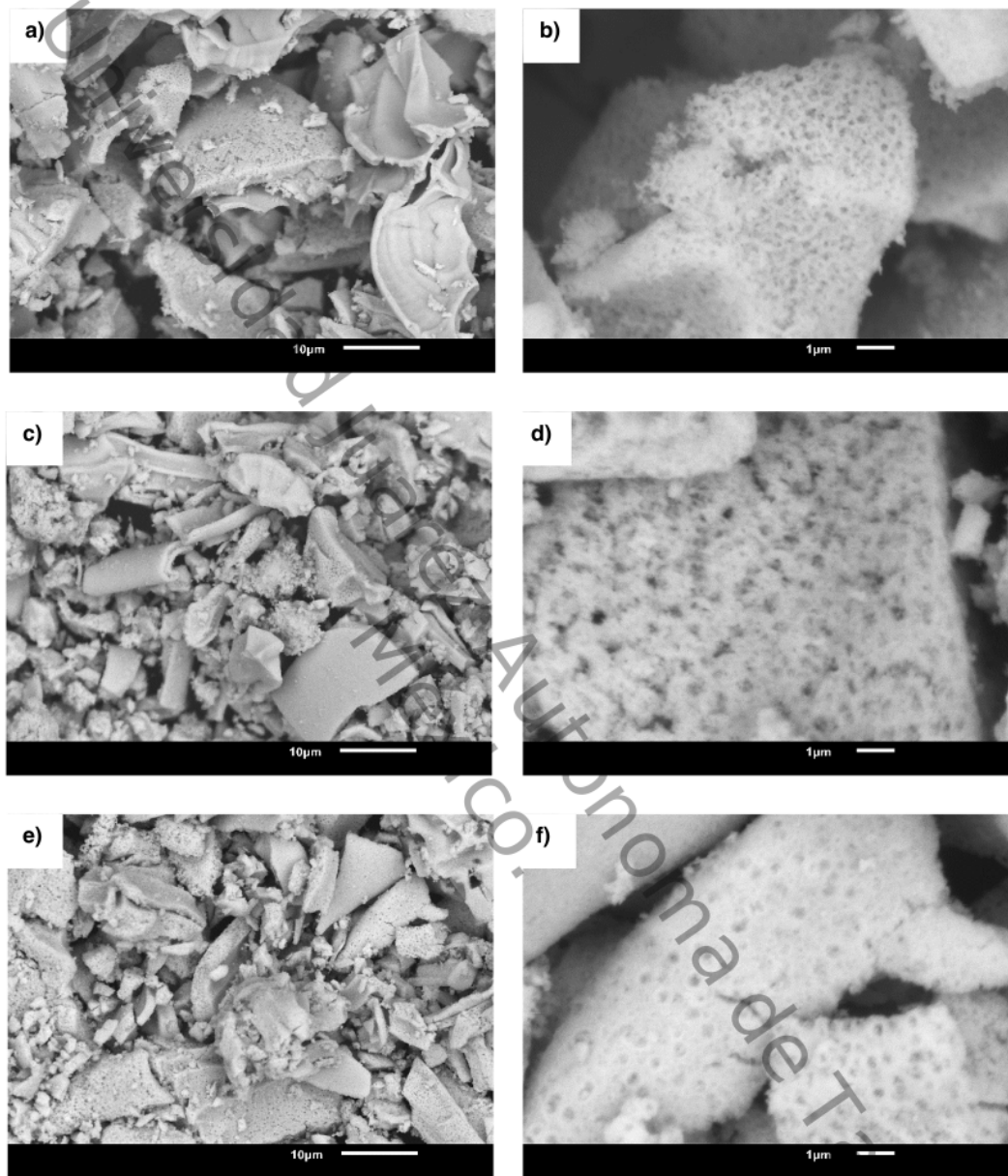


Figure 15. SEM images of a) and b) BCaFO-05; c) and d) BCa-FO-10; e) and f) BCaFO-15 samples.

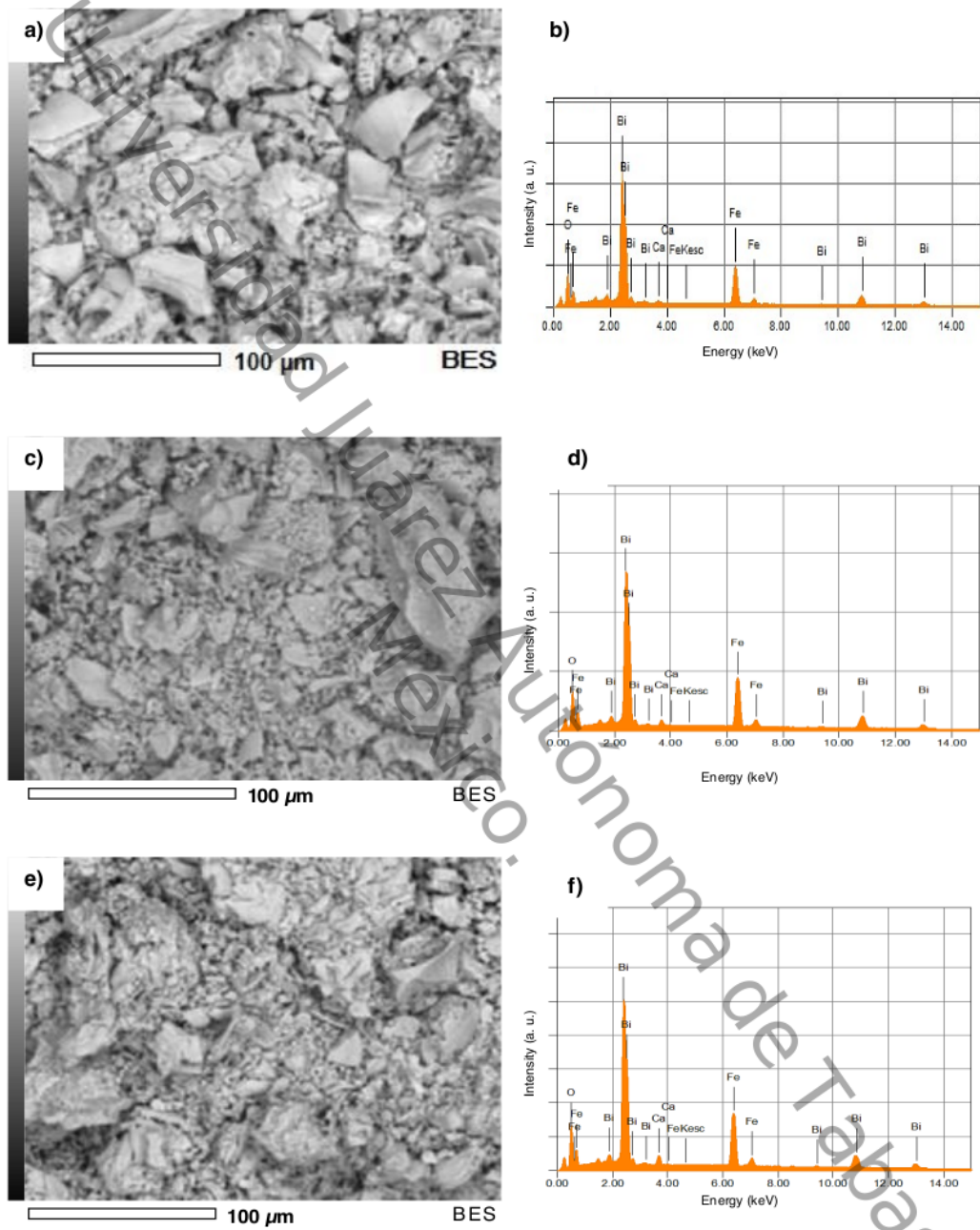


Figure 16. SEM images of a) BCaFO-05; c) BCaFO-10; and e) BCaFO-15. EDS spectra of b) BCaFO-05; d) BCaFO-10; and f) BCaFO-15 samples.

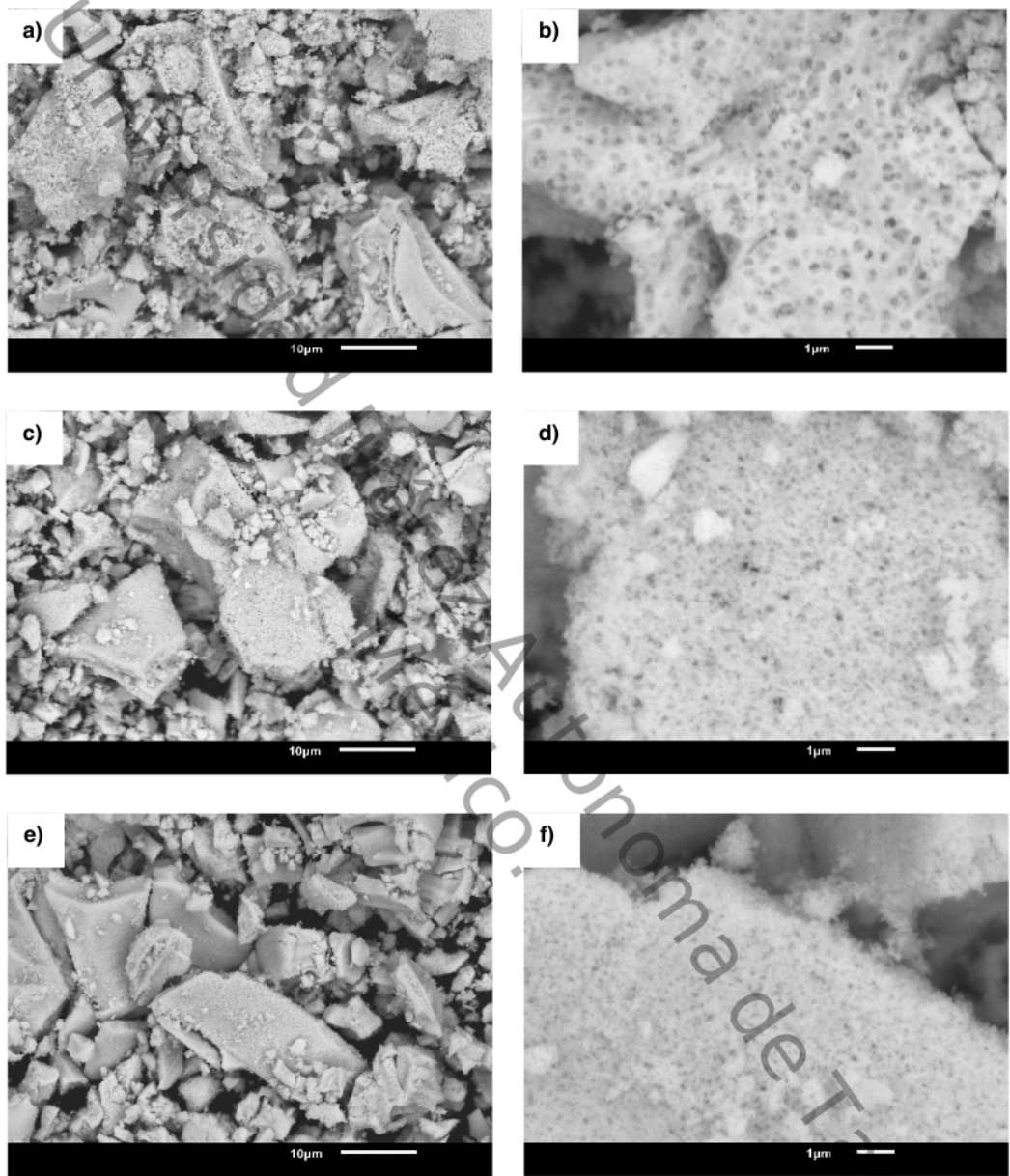


Figure 17. SEM images of a) and b) BSrFO-05; c) and d) BSr-FO-10; e) and f) BSrFO-15.

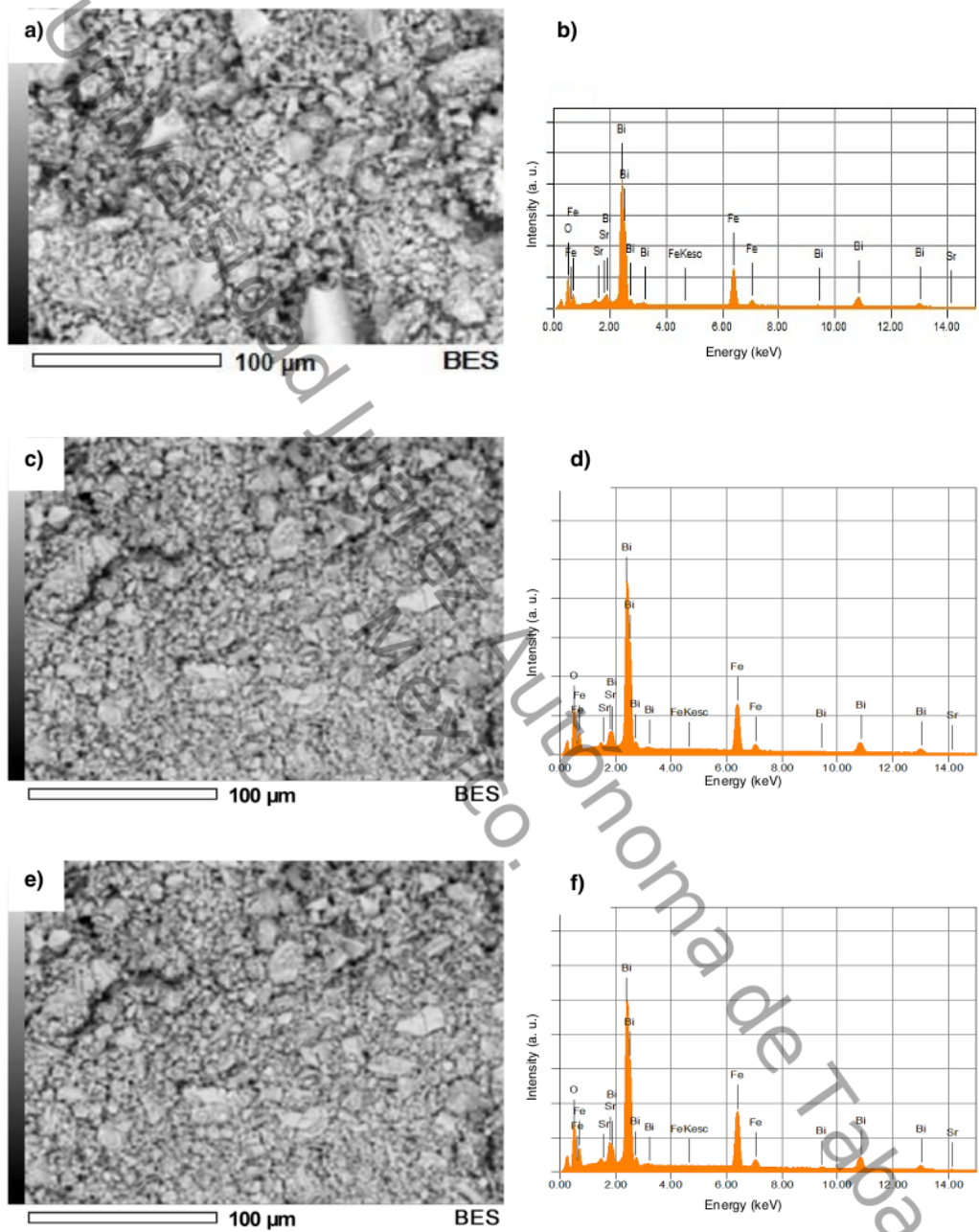


Figure 18. SEM images of a) BSrFO-05; c) BSrFO-10; and e) BSrFO-15. EDS spectra of b) BSrFO-05; d) BSrFO-10; and f) BSrFO-15 samples.

4.4 UV-Vis Diffuse Reflectance Spectroscopy (DRS)

The band gap of the samples was estimated by Diffuse reflectance spectroscopy using [Equation 14](#) [162].

$$\alpha h\nu = A(E_g - h\nu)^n \quad 14$$

1

where α is the absorption coefficient, $h\nu$ is the incident photon energy, A is the absorption constant, E_g is band gap and n is a constant having value $1/2$ for direct band gap and 2 for indirect band gap.

[Figure 19](#) shows the Tauc plot $(\alpha h\nu)^2$ vs photon energy to calculate the band gap of the undoped BFO sample. The linear portion of Tauc plot was extrapolated to $\alpha = 0$, so the estimated band gap value is 2.24 eV ([Table 8](#)). According to the literature, this value corresponds to the energy difference between top of the valence band (O 2p) and bottom of the conduction band (Fe 3d) of BFO [163].

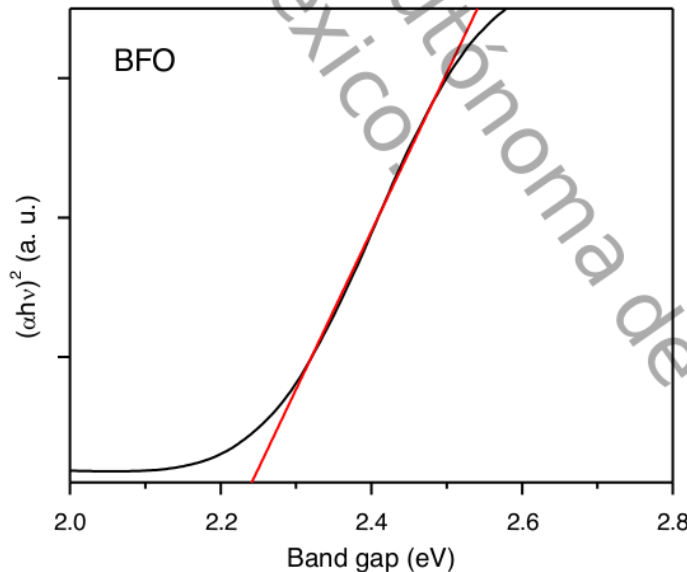


Figure 19. Tauc plot $(\alpha h\nu)^2$ vs E_g of BFO.

Figure 20 shows the Tauc plot $(\alpha h\nu)^2$ vs photon energy of the BCaFO samples. A decrement in the characteristic absorption spectra can be observed with increasing the Ca content. Previous studies have confirmed that a decrement in band gap may be attributed to the electronic transitions involving charge transfer from valence band O 2p states to conduction band Fe 3d states [164,165]. Thus, the obtained band gab values can suggest an enhancement in the visible light adsorption of the BCaFO samples.

As it is also known, Ca doping in BFO lattice may lead defects such as oxygen vacancies. These vacancies can generate impurity levels in the forbidden band, which results in the shift in the donor level above the original valence band. Meanwhile with increasing Ca content, the Ca acceptor band is introduced in the forbidden band, which causes the narrowing of band gap [166].

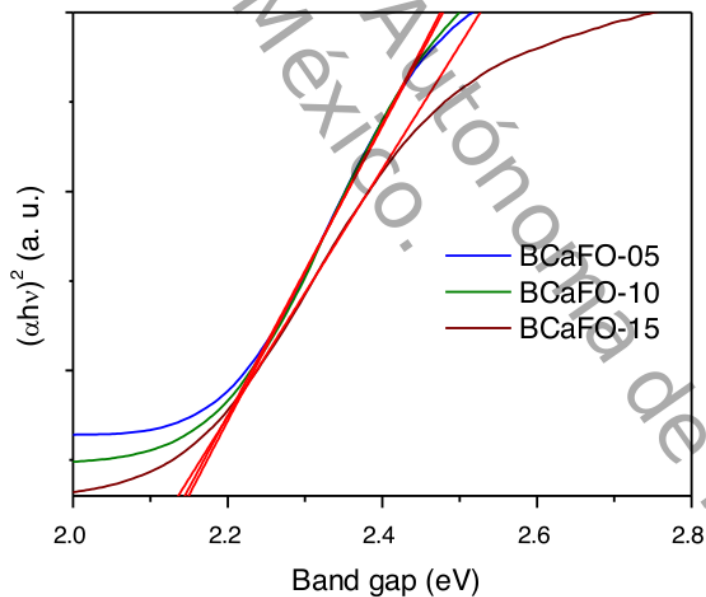


Figure 20. Tauc plot $(\alpha h\nu)^2$ vs E_g of BFO-Ca ($0 < x < 0.15$).

For the BSrFO samples (Figure 21), the band gap decreased with increasing the Sr content; however, a direct function of the band gap variation and Sr concentration cannot be suggested. The calculations resulted narrower than undoped BFO band gap, although wider than the values obtained when it was doped with Ca, which are comparable with previous reports [167]. It has been reported that this decrease in the band gap may be ascribed to the orientation of oxygen octahedral, changes in the crystal structure and decrease of the contribution of a secondary phase present in the compound [168, 169].

Similar to the Ca cations, Sr cations may form defects on the electronic structure and oxygen vacancies to compensate the required charge in the BFO lattice. In order to neutralize the charge produced due to the mechanism of charge compensation, doping acceptor Sr^{2+} ions in BFO would generate oxygen vacancies [170].

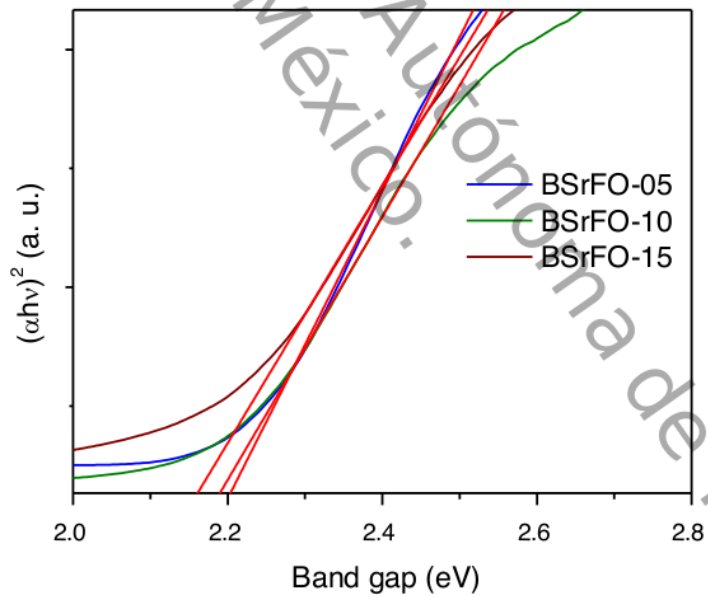


Figure 21. Tauc plot $(\alpha h\nu)^2$ vs Eg of BFO-Sr ($0 < x < 0.15$).

The direct band gap values have been estimated for BFO, BCaFO and BSrFO powders, respectively, using the slope of the linear portion. They are summarized in

Table 8, resulting narrower than 2.24 eV of visible light energy. In agreement with the XRD results and previous reports, the bandgap energy also depends upon the particles size. The reduction in optical band-gap energy with increasing dopant concentration may also cause enhancement of surface area, contraction of the unit cell volume and reduction in average crystallite size. This trend of reduction in Eg with decreasing crystallite size could be ascribed to the competing effects of micro-strain, columbic interactions, and oxygen defects [171]. However, an increase of the crystallite size and decrease of the Eg can be observed for the substitution with 15 mol% dopant, this should be describe by other effects related to the internal chemical pressure and the presence of secondary phases [154].

Table 8. Band gap values for the BFO, BCaFO and BSrFO samples.

Samples	BFO	BCaFO-05	BCaFO-10	BCaFO-15	BSrFO-05	BSrFO-10	BSrFO-15
Eg (eV)	2.24	2.15	2.14	2.13	2.20	2.19	2.16

Although the synthesized powders should exhibit the ability of photocatalytic degradation under visible-light irradiation, other parameters may also affect its performance of the optimal photocatalyst on the degradation of organic pollutants.

4.5 X-Ray Photoelectron Spectroscopy (XPS)

Since Fe valence is sensitive to oxygen vacancies, XPS is used to investigate the Fe composition of BFO samples and to clarify the type of traps present. All signals were referenced to C 1s peak at 284.7 eV, arising from adventitious carbon. Different Gaussian functions were applied to unfold overlapping peaks.

Binding energy of core-level electrons for constituent elements Bi, Fe and O is shown in Figure 22. The Bi 4f state typically involves two peaks centered at 159 eV and 164 eV, assignable to Bi 4f_{7/2} and Bi 4f_{5/2} states of Bi³⁺ species, respectively [172]. This confirms that bismuth ions are in the trivalent oxidation state. No zero valent Bi nor high oxidation state of Bi (e.g. Bi⁵⁺) was observed here.

The Fe 2p core-level spectrum contains two main peaks, which correspond to the Fe 2p_{1/2} and Fe 2p_{3/2} states. Satellite peaks are also observed, which are thought to be characteristic of Fe oxidation. The Fe 2p_{3/2} peak was well fitted by two peaks, corresponding to the Fe³⁺ and Fe²⁺ states at 710.9 and 709.5 eV, respectively [173,174]. This demonstrates that the BFO sample is a mixed valence system of Fe³⁺ and Fe²⁺, and that the ratio of these states is about 1:2. Fe²⁺ possibly originates from the charge compensation of oxygen vacancies, which is common in perovskite oxides, in agreement with previous reports [175].

The O 1s core levels are divided into the low binding energy peaks and the high binding energy peaks. The asymmetric peak of the O anion at BE = 531.5 eV proves that oxygen vacancies are present in the BFO.

It is known that oxygen vacancy can form a defect-induced impurity band between the conduction band and valence band [166]. Therefore, doping Ca²⁺ or Sr²⁺ acceptor ions in BFO would generate oxygen vacancy to neutralize the charge produced due to the mechanism of charge compensation.

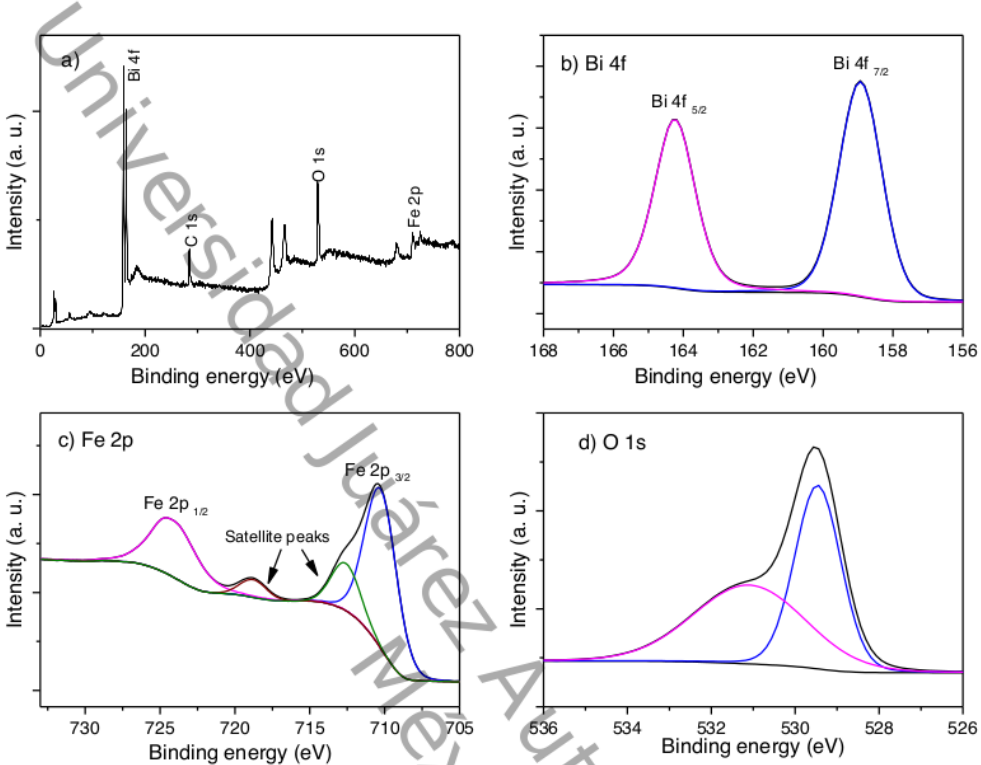


Figure 22. a) XPS wide-scan spectra of the prepared undoped BFO sample; b) Bi 4f peaks; c) Fe 2p peaks; d) XPS O 1s peaks.

Figure 23 shows the XPS spectra of the BCaFO-10 sample, selected as representative. The Ca 2p state typically involves two peaks centered at 346.8 eV and 350.4 eV, assignable to Ca 2p_{1/2} and Ca 2p_{3/2} states of Ca²⁺ species, respectively. No zero valent Ca was observed here.

The present results also confirm the coexistence of chemical states Fe³⁺ and Fe²⁺ ions. With the incorporation of Ca, Fe 2p_{3/2} and Fe 2p_{1/2} peaks as well as the satellite peaks shifted to lower binding energy, implying that the contents of Fe²⁺ and its associated oxygen vacancies increase with the Ca doping [176].

Comparing the ratio of fitted O 1s peak areas, the concentration ratio of oxygen vacancies and O decreased, indicating that the amount of oxygen vacancies increased with the incorporation of Ca²⁺ ions. It is reported that the origin of oxygen

vacancy could be attributed to doping Ca^{2+} at A-site and the redox reaction between Fe^{3+} and Fe^{2+} on the surface of the particles for charge neutralization [177,178].

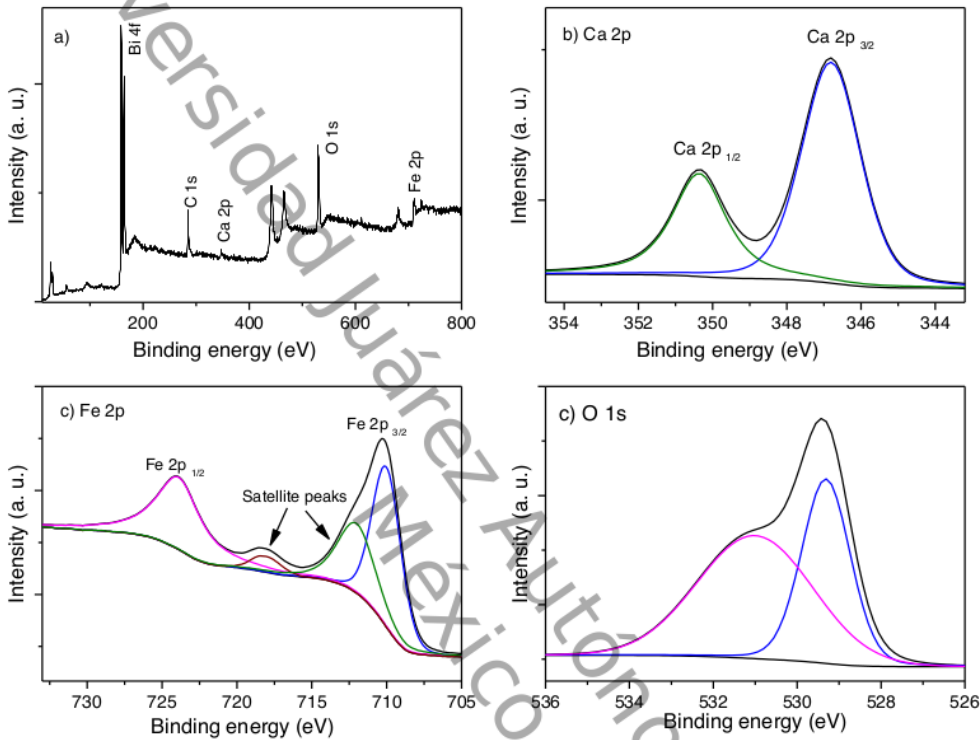


Figure 23. a) XPS wide-scan spectra of the BCaFO-10 sample; b) Ca 2p peaks; c) Fe 2p peaks; d) XPS O 1s peaks.

Figure 24 shows the XPS spectra of the BSrFO-10 sample, selected as representative. The Sr 3d state typically involves two peaks centered at 132.6 eV and 134.3 eV, assignable to $\text{Sr } 3\text{d}_{3/2}$ and $\text{Sr } 3\text{d}_{5/2}$ states of Sr^{2+} species, respectively. No changes in the binding energy of Bi nor any signal of metallic Sr were observed here, which may indicate that Sr^{2+} should have successfully substituted some of Bi ions in the BFO lattice.

The results also confirmed that the oxidation states of Fe^{3+} and Fe^{2+} co-exist. In this case, the binding energy of Fe^{2+} and Fe^{3+} cations slightly increased after Sr doping. Among the compensation of oxygen vacancies, this slight change may be attributed

to the changes in the Fe-O bond, due to the lattice distortion caused by the incorporation of similar ionic radius in the structure, as discussed in the XRD results section [179].

The two O 1s peaks could be ascribed to the lattice oxygen and surface chemisorbed oxygen, arising from the oxygen-metal bonds and surface chemisorbed species (such as O^- , O_2^- and O^{2-}), respectively. These absorbed species are generally associated with the formation of oxygen vacancies in perovskite oxides [180]. Therefore, this behavior may indicate an increase of oxygen vacancies with the incorporation of Sr^{2+} ions to maintain the electrical neutrality of the system.

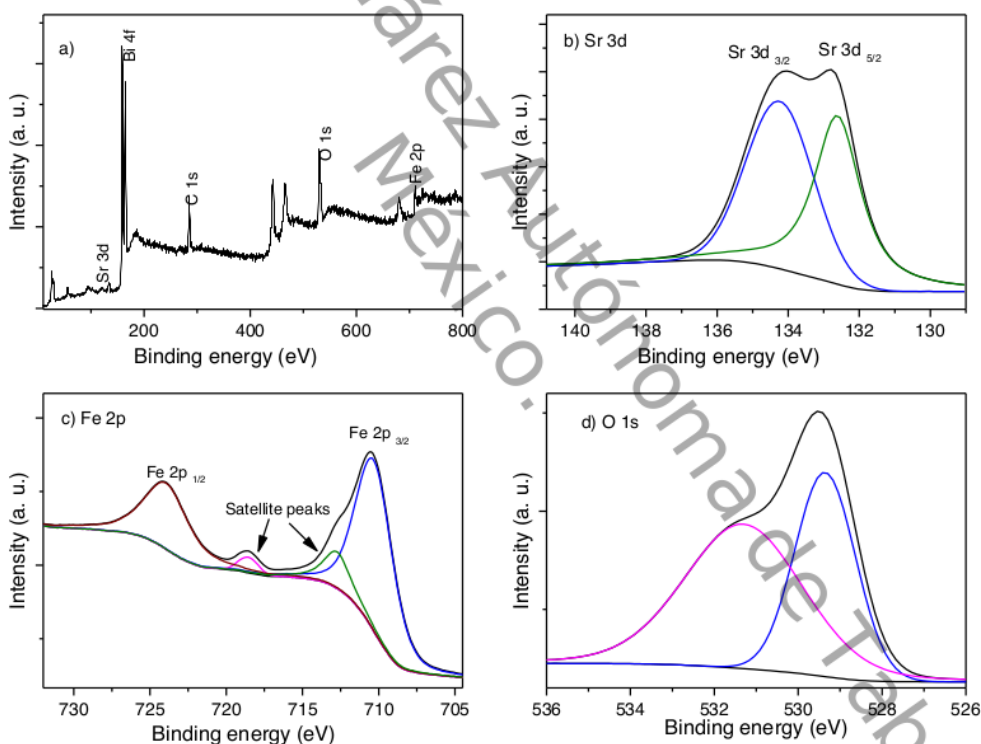


Figure 24. a) XPS wide-scan spectra of the BSrFO-10 sample; b) Sr 3d peaks; c) Fe 2p peaks; d) XPS O 1s peaks.

Chapter 5: Photocatalytic Activity of $B_{1-x}A_xFeO_3$

Universidad Juárez Autónoma de Tabasco.
México.

5.1 Methylene blue photocatalytic degradation

As it is known, BFO can be considered a photocatalyst for degradation of organic pollutants in water due to its narrow band gap (2.2 - 2.8 eV) and excellent chemical stability [21]. In this sense, the photocatalytic performances of BCaFO-05, BCaFO-10 and BCaFO-15 were evaluated towards the degradation of methylene blue (MB) under natural sunlight irradiation. Also, the photocatalytic activity of undoped BFO was investigated to be compared for all the cases.

Figure 25 shows the MB photocatalytic degradation as a function of light irradiation time. The photocatalytic MB degradation percentages are 28.4%, 37.2% and 31.5% under natural sunlight irradiation after 180 min, for BCaFO-05, BCaFO-10 and BCaFO-15, respectively. Compared with the photocatalytic performance of BFO, which degradation rate reached about 28%, the catalyst with 10 mol% of Ca doping showed the highest degradation efficiency.

Generally, the photocatalytic activity of a semiconductor material is related to surface area, visible light absorption and separation/transporting rates of photogenerated e^-/h^+ [14]. In the present work, the increased photocatalytic activity could be attributed to the optical properties enhanced with doping of 10 mol% Ca, in agreement to the optical and XPS results, which may reduce the e^-/h^+ pair recombination in the MB photodegradation [181].

On the other hand, the optical results may suggest an optimal visible light absorption for the BCaFO-15 sample; however, it can be seen a decrease of its degradation rate, which could be related to the increase on the crystal size caused by the lattice distortion.

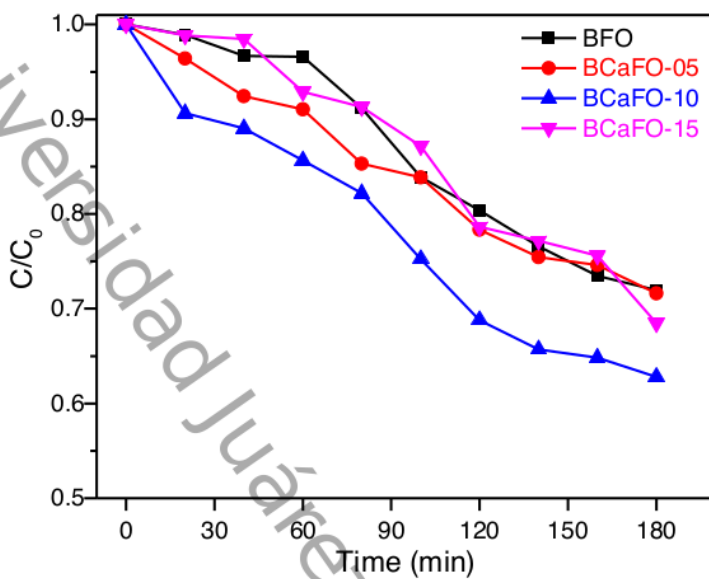


Figure 25. Photocatalytic degradation of MB as a function of the irradiation time under visible light for the BCaFO-05, BCaFO-10 and BCaFO-15 samples.

The graphical evaluation of the degradation rate, by the plots of $\ln(C_0/C)$ versus the sunlight exposure time, is presented in Figure 26. Here, the linear fitting curves indicate that the photocatalytic reaction followed pseudo-first-order reaction kinetics, following the Langmuir-Hinshelwood's model, which equation is (Equation 15) [182]:

$$\ln \frac{C_0}{C} = kt \quad 15$$

1 where C_0 and C are the organic pollutant initial concentration (mg L^{-1}) and at different irradiation time t , respectively, and k is the pseudo-first-order rate constant of photodegradation. The calculated reaction rate constant (k) values were 1.85×10^{-3} , 2.59×10^{-3} and $2.1 \times 10^{-3} \text{ min}^{-1}$ for the BCaFO-05, BCaFO-10 and BCaFO-15 samples, respectively. From these results, an optimum doping concentration of Ca^{2+} ions in BFO nanoparticles for photocatalytic performances could be suggested for 10 mol%.

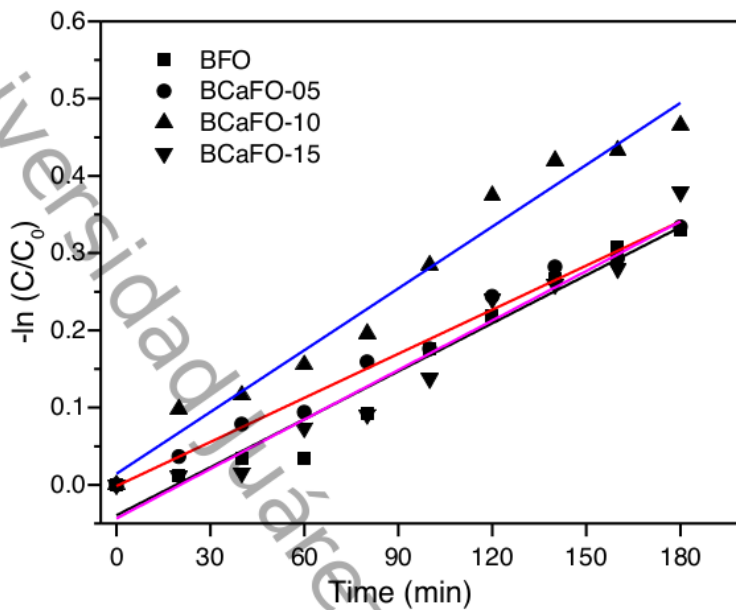


Figure 26. Kinetic curves for the photocatalytic degradation of MB under sunlight irradiation using BCaFO-05, BCaFO-10 and BCaFO-15 samples.

Figure 27 shows the photocatalytic degradation of MB as a function of sunlight exposure time for BSrFO samples. 30.6% of MB was decomposed after 3 h under natural sunlight using the BSrFO-05 sample. Compared with the undoped BFO, the BSrFO-10 exhibited a low activity for the MB photodegradation of only 14.4%. Among all the BSrFO photocatalysts, the BSrFO-15 sample exhibited a higher activity, and about 27.6% of MB was decomposed.

It can be noticed that the photocatalytic performances of obtained BSrFO photocatalyst were significantly influenced by the Sr doping concentration. With the increase of the Sr doping concentration from 5% to 10%, the degradation efficiency of the BSrFO photocatalysts first increased and then decreased. When the Sr doping concentration was 15%, the catalyst increased the degradation efficiency, which was about 2 times than that of BSrFO-10.

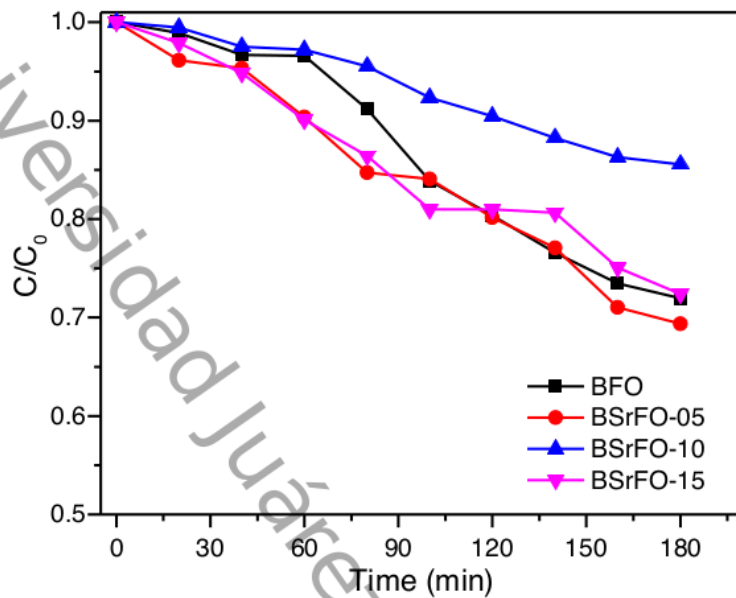


Figure 27. Photocatalytic degradation of MB as a function of the irradiation time under visible light for the BSrFO-05, BSrFO-10 and BSrFO-15 samples.

From Figure 28, the calculated reaction rate constant (k) values were 2.0×10^{-3} , 8.7×10^{-4} and $1.8 \times 10^{-3} \text{ min}^{-1}$ for the BSrFO-05, BSrFO-10 and BSrFO-15 samples, respectively. The reaction rate of the BSrFO samples increased first and then decreased with increasing the concentration of Sr ions, showing a similar behavior to the undoped BFO.

In this case the photocatalytic activity could be significantly influenced by the Sr^{2+} doping concentration. Even though the optical and morphological defects derived from Sr^{2+} dopants would facilitate the separation of photogenerated e^-/h^+ pairs and enhance the photocatalytic activity, the discrepancy might be attributed to the excess of the Sr^{2+} dopant acting as a recombination center in BFO, thus the photoactivity results to be inhibited [24].

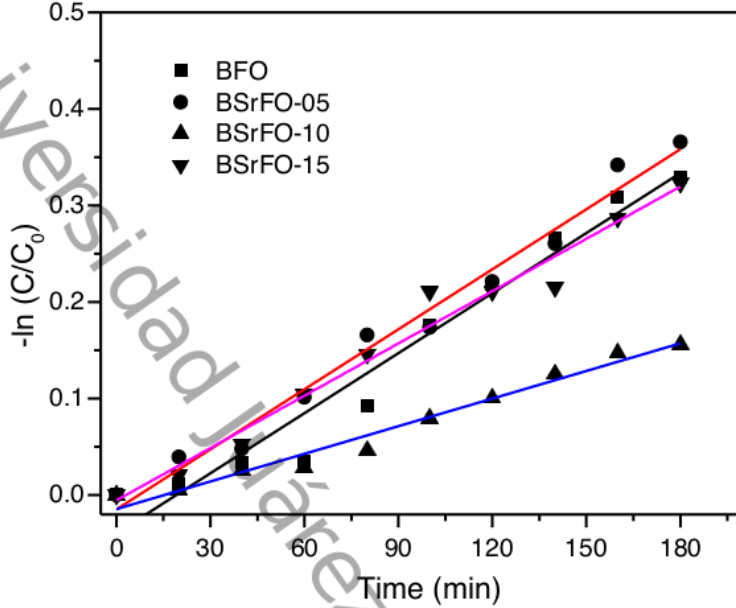


Figure 28. Kinetic curves for the photocatalytic degradation of MB under sunlight irradiation using BSrFO-05, BSrFO-10 and BSrFO-15 samples.

In summary, photocatalytic activity was found to be influenced by the cation dopant, resulting the highest with 10% Ca^{2+} doping and the lowest with 10% Sr^{2+} doping. The enhancement of the photocatalytic activity could be attributed to the oxygen vacancies derived from the defects on the structure, as discussed on the XRD, XPS and optical results. On the other hand, the observed inhibition of the photocatalytic activity could be correlated to the morphological results; however, to confirm the validity of such proposal, further characterization would be required, thus we suggest continuing the investigation of this inhibition in the future.

5.2 4-chlorophenol photocatalytic degradation

To further analyze, the photocatalytic performances of BCaFO-05, BCaFO-10 and BCaFO-15 were investigated towards the degradation of 4-chlorophenol (4CP) under natural sunlight irradiation. As well, the photocatalytic activity of undoped BFO was investigated to be compared for all the cases.

Figure 29 shows the 4CP photocatalytic activity as a function of light irradiation time. After 180 min of sunlight irradiation, 7.78%, 7.28% and 14.8% of 4CP degradation were observed for BCaFO-05, BCaFO-10 and BCaFO-15, respectively. The highest degradation efficiency was observed when the Ca doping concentration was 15%. The enhanced photocatalytic activity could be attributed to the improved structural and optical properties with the substitution of Ca ions.

It can be noticed that the BCaFO-05 and BFCaFO-10 showed an inferior photocatalytic activity, even in comparison with undoped BFO. This could be explained by the inductive effect of the substituent group at the *para* position of the 4CP. The chloride group gives stability to the molecule so, the ring opening is more difficult and the reaction rate is slow [183]. Additionally, 4CP molecule displays pKa values ranging from 9 to 10. Considering that the solutions prepared have a pH value close to neutral, this molecule will present no electrical charges; therefore, will not interact with the photocatalyst surface in a significant manner [184].

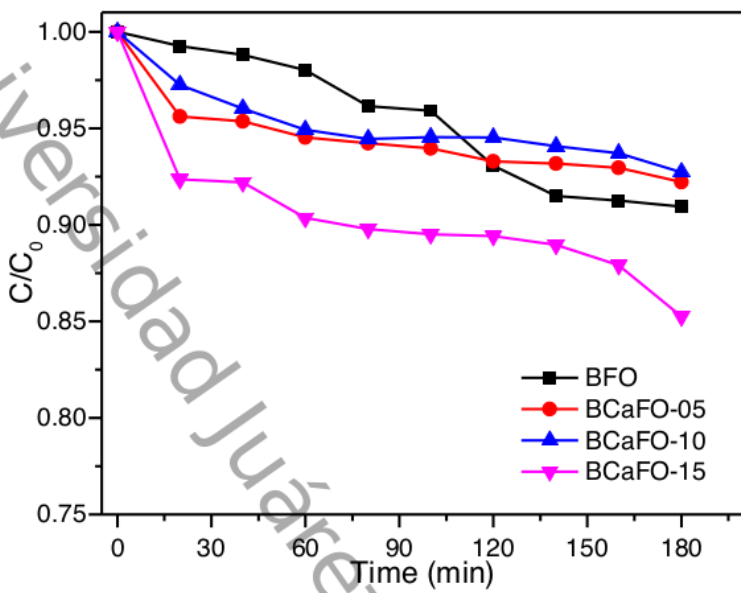


Figure 29. Photocatalytic degradation of 4CP as a function of the irradiation time under visible light for the BCaFO-05, BCaFO-10 and BCaFO-15 samples.

The graphical plots of $\ln(C_0/C)$ versus the sunlight exposure time of the degradation rate are presented in Figure 30. The calculated reaction rate constant (k) values were 4.5×10^{-3} , 4.2×10^{-3} and $8.9 \times 10^{-3} \text{ min}^{-1}$ for the BCaFO-05, BCaFO-10 and BCaFO-15 samples, respectively. Since the reaction rate constant for BCaFO-15 was found to be about 2 times than that of the other samples, a positive effect on the doping concentration of Ca^{2+} ions in BFO nanoparticles for photocatalytic performances could be suggested.

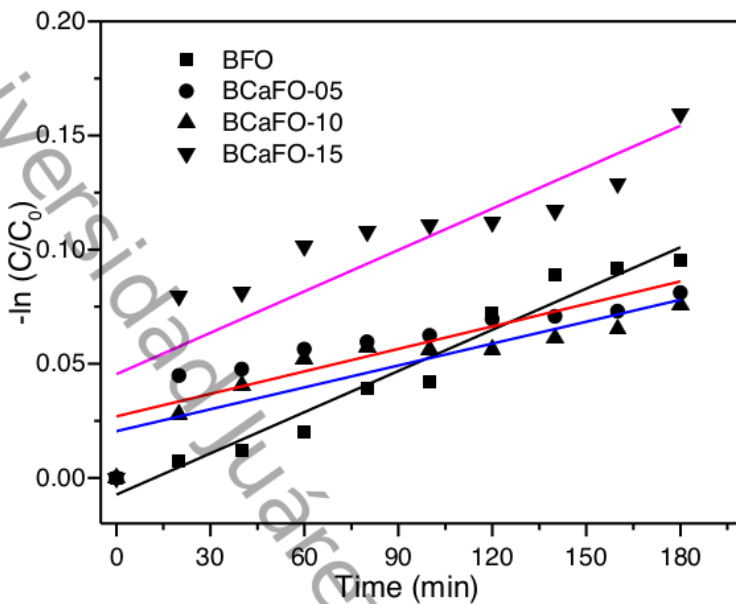


Figure 30. Kinetic curves for the photocatalytic degradation of 4CP under sunlight irradiation using BCaFO-05, BCaFO-10 and BCaFO-15 samples.

Figure 31 shows the 4CP photocatalytic activity as a function of light irradiation time. After 180 min of light irradiation, the photocatalytic 4CP degradation of 5.4%, 15.7% and 15.62% were observed for BSrFO-05, BSrFO-10 and BSrFO-15, respectively. It can be observed that the highest degradation efficiency was showed by the BSrFO-10 and BSrFO-15 samples.

In a similar manner to the BCaFO-05 sample, the BSrFO-05 sample showed low photocatalytic activity, which suggests that the molecule poorly interacts with the photocatalyst, as discussed before. On the other hand, the highest photocatalytic activity of the BSrFO-10 and BSrFO-15 could be ascribed to their narrow band gap. As it is known, when the band gap decreases compared to that of pure BFO, lower incident photon energy in the form of visible light produces the e^-/h^+ pairs which increases the production of hydroxyl radicals ($\cdot OH$) at the surface of the catalyst [185]. Thus, these radicals take part in the photocatalytic process for the decomposition of the 4CP molecule.

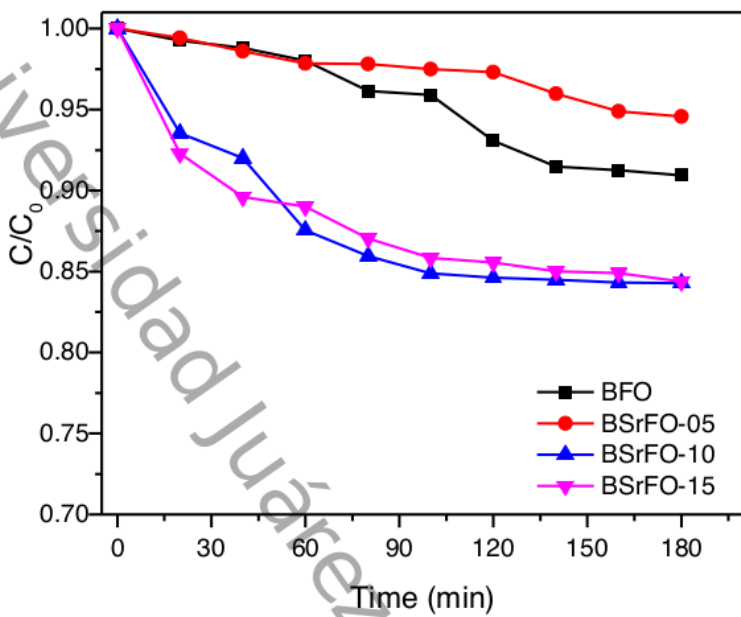


Figure 31. Photocatalytic degradation of 4CP as a function of the irradiation time under visible light for the BSrFO-05, BSrFO-10 and BSrFO-15 samples.

The plots of $\ln(C_0/C)$ versus the sunlight exposure time elaborating the graphical evaluation of the rate of the degradation process are presented in Figure 32. The calculated reaction rate constant (k) values were 3.1×10^{-3} , 9.5×10^{-3} and 9.4×10^{-3} min⁻¹ for the BSrFO-05, BSrFO-10 and BSrFO-15 samples, respectively. The results clearly demonstrated the BSrFO-10 and BSrFO-15 samples, with the doping content being equal to 10% and 15%, respectively, exhibited the highest photodegradation efficiency, which was about 3 times higher than that of BSrFO-05.

From the results, the doping content suggests a key role in achieving the higher photocatalytic activity of the doped BFO samples; if the amount of dopant exceeds to critical value then it may behave as recombination centers for photo-generated charge carriers, which can reduce the photocatalytic performance [27].

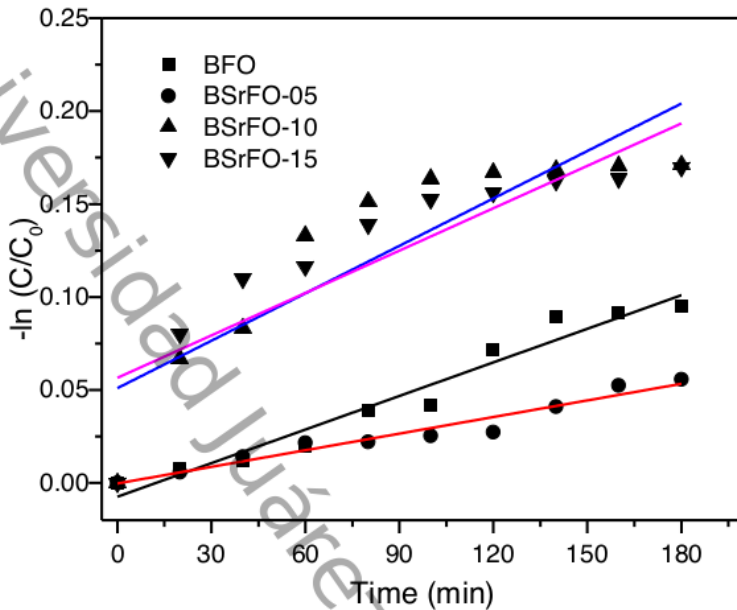


Figure 32. Kinetic curves for the photocatalytic degradation of 4CP under sunlight irradiation using BSrFO-05, BSrFO-10 and BSrFO-15 samples.

According to the literature, there are some reasons to increase the photocatalytic degradation of organic pollutants, such as dyes or benzenes, with alkaline ion doping on the BFO structure. First, the perovskite structures are flexible and allow a distortion with the existence of oxygen vacancies. The substitution with alkaline elements such as Ca^{2+} or Sr^{2+} ions at the trivalent Bi-site in BFO, can easily affect the amount of oxygen vacancies, as an effect of charge compensation, which can lead the inhibition of the recombination of photo-induced e^-/h^+ pairs during the photocatalytic reaction process [186]. The latter can be observed from the photocatalytic activity for the BCaFO-10 and BSrFO-10 samples correlated with the combined structural, optical and XPS results. Since the morphological properties could be another key factor for improving the photocatalytic activity under light irradiation, to further analysis, additional characterizations such as surface area, would be needed.

Conclusions

The Pechini method demonstrated to be efficient for the synthesis of undoped and doped-BFO catalyst, it allowed the formation of rhombohedral crystalline phase. The successful substitution of Ca^{2+} and Sr^{2+} ions by Bi^{3+} in the BFO structure and a reduction of the crystallite size were confirmed. The XRD and Rietveld refinement results also showed the presence of small traces of secondary phases, this is likely due to the facile volatilization of bismuth during the synthesis process. Changes in the grain size and in the band gap value were induced by increasing the dopant concentration. The incorporation of dopant ions in the doped-BFO increased the amount of oxygen vacancies, which could improve the photocatalytic activity of the catalysts on the degradation of MB and 4CP up to 37% and 16%, respectively. The highest photocatalytic efficiency for MB degradation was achieved by the BCaFO-10 sample. In contrast, the highest photocatalytic efficiency for 4CP degradation was given by the BSrFO-10 sample. Therefore, alkaline ion doped-BFO demonstrated to be suitable for the degradation of organic pollutants as MB and 4CP using visible light.

References

1. MiarAlipour, S., Friedmann, D., Scott, J. & Amal, R. TiO₂/porous adsorbents: Recent advances and novel applications. *Journal of Hazardous Materials* **341**, 404–423 (2018).
2. Sharma, S. *et al.* Carbon quantum dot supported semiconductor photocatalysts for efficient degradation of organic pollutants in water: A review. *Journal of Cleaner Production* **228**, 755–769 (2019).
3. Berradi, M. *et al.* Textile finishing dyes and their impact on aquatic environs. *Heliyon* **5**, e02711 (2019).
4. Benzaouak, A. *et al.* Photocatalytic degradation of methylene blue (MB) dye in aqueous solution by ferroelectric Li_{1-x}Ta_{1-x}W_xO₃ materials. *Colloids and Surfaces A: Physicochemical and Engineering Aspects* **553**, 586–592 (2018).
5. Bapat, G., Labade, C., Chaudhari, A. & Zinjarde, S. Silica nanoparticle based techniques for extraction, detection, and degradation of pesticides. *Advances in Colloid and Interface Science* **237**, 1–14 (2016).
6. Mishra, A., Mehta, A. & Basu, S. Clay supported TiO₂ nanoparticles for photocatalytic degradation of environmental pollutants: A review. *Journal of Environmental Chemical Engineering* **6**, 6088–6107 (2018).
7. Sivagami, K., Vikraman, B., Krishna, R. R. & Swaminathan, T. Chlorpyrifos and Endosulfan degradation studies in an annular slurry photo reactor. *Ecotoxicology and Environmental Safety* **134**, 327–331 (2016).
8. Moreira, F. C., Boaventura, R. A. R., Brillas, E. & Vilar, V. J. P. Electrochemical advanced oxidation processes: A review on their application to synthetic and real wastewaters. *Applied Catalysis B: Environmental* **202**, 217–261 (2017).
9. Niu, M. *et al.* The effects of precursors and loading of carbon on the photocatalytic activity of C–BiVO₄ for the degradation of high concentrations of phenol under visible light irradiation. *Catalysis Today* **258**, 585–594 (2015).
10. Mishra, M. & Chun, D.-M. α-Fe₂O₃ as a photocatalytic material: A review. *Applied Catalysis A: General* **498**, 126–141 (2015).
11. Qiao, L. *et al.* Characterization and photoelectrochemical performance of Zn-

- doped TiO₂ films by sol-gel method. *Transactions of Nonferrous Metals Society of China* **26**, 2109–2116 (2016).
- 12. Liang, Q. *et al.* Surfactant-assisted synthesis of photocatalysts: Mechanism, synthesis, recent advances and environmental application. *Chemical Engineering Journal* **372**, 429–451 (2019).
 - 13. Lam, S. M., Shih, J. C. & Mohamed, A. R. A newly emerging visible light-responsive BiFeO₃ perovskite for photocatalytic applications: A mini review. *Materials Research Bulletin* **90**, 15–30 (2017).
 - 14. Gao, X., Dai, Y., Fu, F. & Hua, X. 2D laminated cylinder-like BiFeO₃ composites: Hydrothermal preparation, formation mechanism, and photocatalytic properties. *Solid State Sciences* **62**, 6–12 (2016).
 - 15. Tong, T., Zhang, H., Chen, J., Jin, D. & Cheng, J. The photocatalysis of BiFeO₃ disks under visible light irradiation. *Catalysis Communications* **87**, 23–26 (2016).
 - 16. Guo, Y. *et al.* A simple method using citric acid as the template agent to improve photocatalytic performance of BiFeO₃ nanoparticles. *Materials Letters* **196**, 57–60 (2017).
 - 17. Safizade, B., Masoudpanah, S. M., Hasheminiasari, M. & Ghasemi, A. Photocatalytic activity of BiFeO₃/ZnFe₂O₄ nanocomposites under visible light irradiation. *RSC Advances* **8**, 6988–6995 (2018).
 - 18. Humayun, M. *et al.* Enhanced visible-light activities of porous BiFeO₃ by coupling with nanocrystalline TiO₂ and mechanism. *Applied Catalysis B: Environmental* **180**, 219–226 (2016).
 - 19. Ramezanalizadeh, H. & Manteghi, F. Immobilization of mixed cobalt/nickel metal-organic framework on a magnetic BiFeO₃: A highly efficient separable photocatalyst for degradation of water pollutions. *Journal of Photochemistry and Photobiology A: Chemistry* **346**, 89–104 (2017).
 - 20. Ponraj, C., Vinitha, G. & Daniel, J. A review on the visible light active BiFeO₃ nanostructures as suitable photocatalyst in the degradation of different textile dyes. *Environmental Nanotechnology, Monitoring and Management* **7**, 110–120 (2017).

21. Soltani, T. & Lee, B. K. Novel and facile synthesis of Ba-doped BiFeO₃ nanoparticles and enhancement of their magnetic and photocatalytic activities for complete degradation of benzene in aqueous solution. *Journal of Hazardous Materials* **316**, 122–133 (2016).
22. Niu, F. *et al.* Synthesis of Pt/BiFeO₃ heterostructured photocatalysts for highly efficient visible-light photocatalytic performances. *Solar Energy Materials and Solar Cells* **143**, 386–396 (2015).
23. Chen, D. *et al.* Defective BiFeO₃ with surface oxygen vacancies: Facile synthesis and mechanism insight into photocatalytic performance. *Solar Energy Materials and Solar Cells* **171**, 24–32 (2017).
24. Hu, Z. *et al.* Facile synthesis of Sm-doped BiFeO₃ nanoparticles for enhanced visible light photocatalytic performance. *Materials Science and Engineering B: Solid-State Materials for Advanced Technology* **220**, 1–12 (2017).
25. Haruna, A., Abdulkadir, I. & Idris, S. O. Photocatalytic activity and doping effects of BiFeO₃ nanoparticles in model organic dyes. *Helijon* **6**, e03237 (2020).
26. Ahmad, S. *et al.* The impact of Yb and Co on structural, magnetic, electrical and photocatalytic behavior of nanocrystalline multiferroic BiFeO₃ particles. *Ceramics International* **43**, 16880–16887 (2017).
27. Irfan, S. *et al.* Critical review: Bismuth ferrite as an emerging visible light active nanostructured photocatalyst. *Journal of Materials Research and Technology* **8**, 6375–6389 (2019).
28. Vijayasundaram, S. V., Suresh, G. & Kanagadurai, R. Chemically synthesized phase-pure BiFeO₃ nanoparticles: Influence of agents on the purity. *Nano-Structures & Nano-Objects* **8**, 1–6 (2016).
29. Shariq, M., Kaur, D. & Chandel, V. S. Structural, magnetic and optical properties of multiferroic (BiFeO₃)_{1-x}(BaTiO₃)_x solid solutions. *Chinese Journal of Physics* **55**, 2192–2198 (2017).
30. Golić, D. L. *et al.* Structural, ferroelectric and magnetic properties of BiFeO₃ synthesized by sonochemically assisted hydrothermal and hydro-evaporation chemical methods. *Journal of the European Ceramic Society* **36**, 1623–1631

- (2016).
31. Gao, T. *et al.* Shape-controlled preparation of bismuth ferrite by hydrothermal method and their visible-light degradation properties. *Journal of Alloys and Compounds* **648**, 564–570 (2015).
 32. Gil-González, E. *et al.* Characterization of mechanothesized $\text{Bi}_{1-x}\text{Sm}_x\text{FeO}_3$ samples unencumbered by secondary phases or compositional inhomogeneity. *Journal of Alloys and Compounds* **711**, 541–551 (2017).
 33. Li, J. & Yan, D. Z. Low-temperature synthesis of pure BiFeO_3 phase and variation in its morphology with temperature. *Ceramics International* **44**, 18271–18278 (2018).
 34. Yu, L. & Yıldız, İ. Energy and Water Pollution. in *Comprehensive Energy Systems* **1–5**, 950–979 (2018).
 35. Fazal, T. *et al.* Bioremediation of textile wastewater and successive biodiesel production using microalgae. *Renewable and Sustainable Energy Reviews* **82**, 3107–3126 (2018).
 36. Garcia-Segura, S. & Brillas, E. Applied photoelectrocatalysis on the degradation of organic pollutants in wastewaters. *Journal of Photochemistry and Photobiology C: Photochemistry Reviews* **31**, 1–35 (2017).
 37. Grandclément, C. *et al.* From the conventional biological wastewater treatment to hybrid processes, the evaluation of organic micropollutant removal: A review. *Water Research* **111**, 297–317 (2017).
 38. Jo, W. K. & Tayade, R. J. Recent developments in photocatalytic dye degradation upon irradiation with energy-efficient light emitting diodes. *Cuihua Xuebao/Chinese Journal of Catalysis* **35**, 1781–1792 (2014).
 39. Zhu, D. & Zhou, Q. Action and mechanism of semiconductor photocatalysis on degradation of organic pollutants in water treatment: A review. *Environmental Nanotechnology, Monitoring & Management* **12**, 100255 (2019).
 40. Natarajan, S., Bajaj, H. C. & Tayade, R. J. Recent advances based on the synergistic effect of adsorption for removal of dyes from waste water using photocatalytic process. *Journal of Environmental Sciences (China)* **65**, 201–

- 222 (2018).
41. Sen, S. K., Raut, S., Bandyopadhyay, P. & Raut, S. Fungal decolouration and degradation of azo dyes: A review. *Fungal Biology Reviews* **30**, 112–133 (2016).
 42. Sivakumar, A., Murugesan, B., Loganathan, A. & Sivakumar, P. A review on decolourisation of dyes by photodegradation using various bismuth catalysts. *Journal of the Taiwan Institute of Chemical Engineers* **45**, 2300–2306 (2014).
 43. Katheresan, V., Kansedo, J. & Lau, S. Y. Efficiency of various recent wastewater dye removal methods: A review. *Journal of Environmental Chemical Engineering* **6**, 4676–4697 (2018).
 44. Singh, R. L., Singh, P. K. & Singh, R. P. Enzymatic decolorization and degradation of azo dyes - A review. *International Biodegradation and Biodegradation* **104**, 21–31 (2015).
 45. Khandare, R. V. & Govindwar, S. P. Phytoremediation of textile dyes and effluents: Current scenario and future prospects. *Biotechnology Advances* **33**, 1697–1714 (2015).
 46. Sarangapani, C. *et al.* Pesticide degradation in water using atmospheric air cold plasma. *Journal of Water Process Engineering* **9**, 225–232 (2016).
 47. Singh, J., Yang, J. K. & Chang, Y. Y. Rapid degradation of phenol by ultrasound-dispersed nano-metallic particles (NMPs) in the presence of hydrogen peroxide: A possible mechanism for phenol degradation in water. *Journal of Environmental Management* **175**, 60–66 (2016).
 48. Vuolo, M. M., Lima, V. S. & Maróstica Junior, M. R. Phenolic Compounds. in *Bioactive Compounds* **22**, 33–50 (2019).
 49. Puszkarewicz, A., Kaleta, J. & Papciak, D. Adsorption of Phenol from Water on Natural Minerals. *Journal of Ecological Engineering* **19**, 132–138 (2018).
 50. Cycoń, M., Mrozik, A. & Piotrowska-Seget, Z. Bioaugmentation as a strategy for the remediation of pesticide-polluted soil: A review. *Chemosphere* **172**, 52–71 (2017).
 51. Wei, X. *et al.* Characterization of phenol and cresol biodegradation by compound-specific stable isotope analysis. *Environmental Pollution* **210**, 166–

- 173 (2016).
52. Aslam, M., Ismail, I. M. I., Chandrasekaran, S. & Hameed, A. Morphology controlled bulk synthesis of disc-shaped WO_3 powder and evaluation of its photocatalytic activity for the degradation of phenols. *Journal of Hazardous Materials* **276**, 120–128 (2014).
 53. Huang, Z. et al. Community analysis and metabolic pathway of halophilic bacteria for phenol degradation in saline environment. *International Biodeterioration & Biodegradation* **94**, 115–120 (2014).
 54. Kontos, S. S., Koutsoukos, P. G. & Paraskeva, C. A. Removal and recovery of phenolic compounds from olive mill wastewater by cooling crystallization. *Chemical Engineering Journal* **251**, 319–328 (2014).
 55. Kozlova, E. A. et al. Photoreactivity of metal-organic frameworks in the decolorization of methylene blue in aqueous solution. in *Catalysis Today* **266**, 136–143 (Elsevier, 2016).
 56. Peng, Y. et al. Chlorophenols in Municipal Solid Waste Incineration: A review. *Chemical Engineering Journal* **292**, 398–414 (2016).
 57. Rezakazemi, M., Albadarin, A. B., Walker, G. M. & Shirazian, S. Quantum chemical calculations and molecular modeling for methylene blue removal from water by a lignin-chitosan blend. *International Journal of Biological Macromolecules* **120**, 2065–2075 (2018).
 58. Alaoui, A., El Kacemi, K., El Ass, K., Kitane, S. & El Bouzidi, S. Activity of Pt/ MnO_2 electrode in the electrochemical degradation of methylene blue in aqueous solution. *Separation and Purification Technology* **154**, 281–289 (2015).
 59. Yang, B. et al. Effective ultrasound electrochemical degradation of methylene blue wastewater using a nanocoated electrode. *Ultrasonics Sonochemistry* **21**, 1310–1317 (2014).
 60. Zhou, G. et al. Fenton-like degradation of methylene blue using paper mill sludge-derived magnetically separable heterogeneous catalyst: Characterization and mechanism. *Journal of Environmental Sciences (China)* **35**, 20–26 (2015).

-
-
61. Liu, Y., Jin, W., Zhao, Y., Zhang, G. & Zhang, W. Enhanced catalytic degradation of methylene blue by α -Fe₂O₃/graphene oxide via heterogeneous photo-Fenton reactions. *Applied Catalysis B: Environmental* **206**, 642–652 (2017).
62. Al jibouri, A. K. H., Wu, J. & Upreti, S. R. Continuous ozonation of methylene blue in water. *Journal of Water Process Engineering* **8**, 142–150 (2015).
63. Hama Aziz, K. H. et al. Application of a planar falling film reactor for decomposition and mineralization of methylene blue in the aqueous media via ozonation, Fenton, photocatalysis and non-thermal plasma: A comparative study. *Process Safety and Environmental Protection* **113**, 319–329 (2018).
64. Huang, Q., Cao, M., Ai, Z. & Zhang, L. Reactive oxygen species dependent degradation pathway of 4-chlorophenol with Fe@Fe₂O₃ core-shell nanowires. *Applied Catalysis B: Environmental* **162**, 319–326 (2015).
65. De Coster, J., Vanherck, W., Appels, L. & Dewil, R. Selective electrochemical degradation of 4-chlorophenol at a Ti/RuO₂-IrO₂ anode in chloride rich wastewater. *Journal of Environmental Management* **190**, 61–71 (2017).
66. Tian, M., Thind, S. S., Dondapati, J. S., Li, X. & Chen, A. Electrochemical oxidation of 4-chlorophenol for wastewater treatment using highly active UV treated TiO₂ nanotubes. *Chemosphere* **209**, 182–190 (2018).
67. Barreto-Rodrigues, M., Silveira, J., García-Muñoz, P. & Rodriguez, J. J. Dechlorination and oxidative degradation of 4-chlorophenol with nanostructured iron-silver alginate beads. *Journal of Environmental Chemical Engineering* **5**, 838–842 (2017).
68. Chen, H. et al. Highly active iron-containing silicotungstate catalyst for heterogeneous Fenton oxidation of 4-chlorophenol. *Journal of Molecular Catalysis A: Chemical* **406**, 72–77 (2015).
69. Chen, J., Tian, S., Lu, J. & Xiong, Y. Catalytic performance of MgO with different exposed crystal facets towards the ozonation of 4-chlorophenol. *Applied Catalysis A: General* **506**, 118–125 (2015).
70. Oputu, O., Chowdhury, M., Nyamayaro, K., Fatoki, O. & Fester, V. Catalytic activities of ultra-small β -FeOOH nanorods in ozonation of 4-chlorophenol.

- Journal of Environmental Sciences (China)* **35**, 83–90 (2015).
71. Sivasubramanian, S. & Namasivayam, S. K. R. Phenol degradation studies using microbial consortium isolated from environmental sources. *Journal of Environmental Chemical Engineering* **3**, 243–252 (2015).
 72. Khaksar, A. M., Nazif, S., Taebi, A. & Shahghasemi, E. Treatment of phenol in petrochemical wastewater considering turbidity factor by backlight cascade photocatalytic reactor. *Journal of Photochemistry and Photobiology A: Chemistry* **348**, 161–167 (2017).
 73. Bora, L. V. & Mewada, R. K. Visible/solar light active photocatalysts for organic effluent treatment: Fundamentals, mechanisms and parametric review. *Renewable and Sustainable Energy Reviews* **76**, 1393–1421 (2017).
 74. Xu, B. *et al.* Photocatalytic removal of perfluoroalkyl substances from water and wastewater: Mechanism, kinetics and controlling factors. *Chemosphere* **189**, 717–729 (2017).
 75. Mamaghani, A. H., Haghigat, F. & Lee, C. S. Photocatalytic oxidation technology for indoor environment air purification: The state-of-the-art. *Applied Catalysis B: Environmental* **203**, 247–269 (2017).
 76. Qi, K., Cheng, B., Yu, J. & Ho, W. Review on the improvement of the photocatalytic and antibacterial activities of ZnO. *Journal of Alloys and Compounds* **727**, 792–820 (2017).
 77. Lam, S.-M., Sin, J.-C. & Mohamed, A. R. A review on photocatalytic application of g-C₃N₄/semiconductor (CNS) nanocomposites towards the erasure of dyeing wastewater. *Materials Science in Semiconductor Processing* **47**, 62–84 (2016).
 78. Shayegan, Z., Lee, C.-S. & Haghigat, F. TiO₂ photocatalyst for removal of volatile organic compounds in gas phase – A review. *Chemical Engineering Journal* **334**, 2408–2439 (2018).
 79. Xiao, J., Xie, Y. & Cao, H. Organic pollutants removal in wastewater by heterogeneous photocatalytic ozonation. *Chemosphere* **121**, 1–17 (2015).
 80. Marothu, V. K., Gorrepati, M., Idris, N. F., Idris, S. A. M. & Lella, R. K. C. Photocatalysis of β-blockers – An overview. *Arabian Journal of Chemistry*

- (2014).
81. Etacheri, V., Di Valentin, C., Schneider, J., Bahnemann, D. & Pillai, S. C. Visible-light activation of TiO₂ photocatalysts: Advances in theory and experiments. *Journal of Photochemistry and Photobiology C: Photochemistry Reviews* **25**, 1–29 (2015).
 82. Raizada, P., Sudhaik, A. & Singh, P. Photocatalytic water decontamination using graphene and ZnO coupled photocatalysts: A review. *Materials Science for Energy Technologies* **2**, 509–525 (2019).
 83. Abdullah, H., Khan, M. M. R., Ong, H. R. & Yaakob, Z. Modified TiO₂ photocatalyst for CO₂ photocatalytic reduction: An overview. *Journal of CO₂ Utilization* **22**, 15–32 (2017).
 84. Abdullah, H., Khan, M. M. R., Ong, H. R. & Yaakob, Z. Modified TiO₂ photocatalyst for CO₂ photocatalytic reduction: An overview. *Journal of CO₂ Utilization* **22**, 15–32 (2017).
 85. Shaham-Waldmann, N. & Paz, Y. Away from TiO₂: A critical minireview on the developing of new photocatalysts for degradation of contaminants in water. *Materials Science in Semiconductor Processing* **42**, 72–80 (2016).
 86. Abdellah, M. H., Nosier, S. A., El-Shazly, A. H. & Mubarak, A. A. Photocatalytic decolorization of methylene blue using TiO₂/UV system enhanced by air sparging. *Alexandria Engineering Journal* **57**, 3727–3735 (2018).
 87. Banerjee, S., Benjwal, P., Singh, M. & Kar, K. K. Graphene oxide (rGO)-metal oxide (TiO₂/Fe₃O₄) based nanocomposites for the removal of methylene blue. *Applied Surface Science* **439**, 560–568 (2018).
 88. Ki, S. J. et al. Improving removal of 4-chlorophenol using a TiO₂ photocatalytic system with microwave and ultraviolet radiation. *Catalysis Today* **293–294**, 15–22 (2017).
 89. Thomas, J., Radhika, S. & Yoon, M. Nd³⁺-doped TiO₂ nanoparticles incorporated with heteropoly phosphotungstic acid: A novel solar photocatalyst for degradation of 4-chlorophenol in water. *Journal of Molecular Catalysis A: Chemical* **411**, 146–156 (2015).
 90. Tang, X., Ma, C., Liu, N., Liu, C. & Liu, S. Visible light β-Bi₂O₃/BiOCl

- heterojunction photocatalyst with highly enhanced photocatalytic activity. *Chemical Physics Letters* **709**, 82–87 (2018).
91. Chen, X. *et al.* Visible light photocatalytic degradation of dyes by β - Bi_2O_3 /graphene nanocomposites. *Journal of Alloys and Compounds* **649**, 872–877 (2015).
 92. Zhou, Y., Shuai, L., Jiang, X., Jiao, F. & Yu, J. Visible-light-driven photocatalytic properties of layered double hydroxide supported- Bi_2O_3 modified by Pd(II) for methylene blue. *Advanced Powder Technology* **26**, 439–447 (2015).
 93. Zhang, J. *et al.* Design of a direct Z-scheme photocatalyst: Preparation and characterization of $\text{Bi}_2\text{O}_3/\text{g-C}_3\text{N}_4$ with high visible light activity. *Journal of Hazardous Materials* **280**, 713–722 (2014).
 94. Li, Y. *et al.* $\text{g-C}_3\text{N}_4$ modified Bi_2O_3 composites with enhanced visible-light photocatalytic activity. *Journal of Physics and Chemistry of Solids* **76**, 112–119 (2015).
 95. Suresh, R. *et al.* Synthesis of Co^{2+} -doped Fe_2O_3 photocatalyst for degradation of pararosaniline dye. *Solid State Sciences* **68**, 39–46 (2017).
 96. Kadirova, Z. C. *et al.* Adsorption and photodegradation of methylene blue with Fe_2O_3 -activated carbons under UV illumination in oxalate solution. *Journal of Environmental Chemical Engineering* **2**, 2026–2036 (2014).
 97. Lei, R. *et al.* Growth of $\text{Fe}_2\text{O}_3/\text{SnO}_2$ nanobelt arrays on iron foil for efficient photocatalytic degradation of methylene blue. *Chemical Physics Letters* **673**, 1–6 (2017).
 98. Hunge, Y. M. Photoelectrocatalytic degradation of 4-chlorophenol using nanostructured α - Fe_2O_3 thin films under sunlight illumination. *Journal of Materials Science: Materials in Electronics* **28**, 11260–11267 (2017).
 99. Du, H., Lin, X., Xu, Z. & Chu, D. Electric double-layer transistors: a review of recent progress. *Journal of Materials Science* **50**, 5641–5673 (2015).
 100. Vijatovic Petrovic, M. M. & Bobic, J. D. Perovskite and Aurivillius. in *Magnetic, Ferroelectric, and Multiferroic Metal Oxides* 35–49 (2018).
 101. Zhang, G. *et al.* A novel perovskite $\text{SrTiO}_3\text{-Ba}_2\text{FeNbO}_6$ solid solution for visible

- light photocatalytic hydrogen production. *Advanced Energy Materials* **7**, 1600932 (2017).
102. Assirey, E. A. R. Perovskite synthesis, properties and their related biochemical and industrial application. *Saudi Pharmaceutical Journal* **27**, 817–829 (2019).
 103. Bashan, V. & Ust, Y. Perovskite catalysts for methane combustion: applications, design, effects for reactivity and partial oxidation. *International Journal of Energy Research* **er.4721** (2019).
 104. Gao, P., Grätzel, M. & Nazeeruddin, M. K. Organohalide lead perovskites for photovoltaic applications. *Energy Environ. Sci.* **7**, 2448–2463 (2014).
 105. Zhang, G., Liu, G., Wang, L. & Irvine, J. T. S. Inorganic perovskite photocatalysts for solar energy utilization. *Chemical Society Reviews* **45**, 5951–5984 (2016).
 106. Moniruddin, M. *et al.* Recent progress on perovskite materials in photovoltaic and water splitting applications. *Materials Today Energy* **7**, 246–259 (2018).
 107. Zlotnik, S., Tobaldi, D. M., Seabra, P., Labrincha, J. A. & Vilarinho, P. M. Alkali Niobate and Tantalate Perovskites as Alternative Photocatalysts. *ChemPhysChem* **17**, 3570–3575 (2016).
 108. Sando, D., Barthélémy, A. & Bibes, M. BiFeO₃ epitaxial thin films and devices: Past, present and future. *Journal of Physics Condensed Matter* **26**, 473201 (2014).
 109. Sreenivas Puli, V. *et al.* Magnetoelectric coupling effect in transition metal modified polycrystalline BiFeO₃ thin films. *Journal of Magnetism and Magnetic Materials* **369**, 9–13 (2014).
 110. Anju *et al.* Structural transitions and multiferroicity in Ba and Co substituted nanosized bismuth ferrite. *Journal of Alloys and Compounds* **697**, 333–340 (2017).
 111. Wu, L., Sui, W., Dong, C., Zhang, C. & Jiang, C. One-dimensional BiFeO₃ nanotubes: Preparation, characterization, improved magnetic behaviors, and prospects. *Applied Surface Science* **384**, 368–375 (2016).
 112. Mtougui, S., Khalladi, R., Ziti, S., Labrim, H. & Bahmad, L. Magnetic properties of the perovskite BiFeO₃: Monte Carlo simulation. *Superlattices and*

- Microstructures* **123**, 111–118 (2018).
113. Bashir, S., Mahmood, W., Riaz, S. & Naseem, S. Structural and Magnetic Properties of BiFeO₃ Thin Films by Sol-Gel. *Materials Today: Proceedings* **2**, 5373–5377 (2015).
 114. Godara, S., Sinha, N., Ray, G. & Kumar, B. Combined structural, electrical, magnetic and optical characterization of bismuth ferrite nanoparticles synthesized by auto-combustion route. *Journal of Asian Ceramic Societies* **2**, 416–421 (2014).
 115. Gao, R. L. *et al.* Effect of cooling oxygen pressure on the photoconductivity in Bi_{0.9}La_{0.1}FeO₃ thin films. *Journal of Alloys and Compounds* **591**, 346–350 (2014).
 116. Katiyar, R. K., Misra, P., Sahoo, S., Morell, G. & Katiyar, R. S. Enhanced photoresponse in BiFeO₃/SrRuO₃ heterostructure. *Journal of Alloys and Compounds* **609**, 168–172 (2014).
 117. Sepahvand, H. & Sharifnia, S. Photocatalytic overall water splitting by Z-scheme g-C₃N₄/BiFeO₃ heterojunction. *International Journal of Hydrogen Energy* **44**, 23658–23668 (2019).
 118. Raghavendra Reddy, V. *et al.* Reduced leakage current of multiferroic BiFeO₃ ceramics with microwave synthesis. *Ceramics International* **40**, 4247–4250 (2014).
 119. Casanova Monteiro, F., de Jesus Cubas, P., Sena Kosera, V., Haas Leandro Monteiro, J. F. & Fujiwara, S. T. Photocatalytic activity of BiFeO₃ in pellet form synthetized using solid state reaction and modified Pechini method. *Journal of Photochemistry and Photobiology A: Chemistry* **367**, 390–396 (2018).
 120. Prodjosantoso, A. K., Kusumawardani, C., Utomo, M. P. & Handoko, C. T. Synthesis and Characterization of Ca_{1-x}Co_xTiO₃ and its Photocatalytic Activity on Photodegradation of Methylene Blue. *Asian Journal of Chemistry* **29**, 1270–1274 (2017).
 121. Wang, P., Pu, Y. & Dong, Z. Effects of different microwave calcination temperatures on the pure BiFeO₃ ceramics prepared by microwave hydrothermal method. in *2015 Joint IEEE International Symposium on the*

- Applications of Ferroelectric (ISAF), International Symposium on Integrated Functionalities (ISIF), and Piezoelectric Force Microscopy Workshop (PFM)*
132–135 (2015)
122. Chen, Z. & Jin, W. Low-temperature acetone-assisted hydrothermal synthesis and characterization of BiFeO₃ powders. *Journal of Materials Science: Materials in Electronics* **25**, 4039–4045 (2014).
 123. Niu, F. *et al.* Hydrothermal synthesis of BiFeO₃ nanoparticles for visible light photocatalytic applications. *Journal of Nanoscience and Nanotechnology* **15**, 9693–9698 (2015).
 124. Park, S., Kim, C. H., Lee, W. J., Sung, S. & Yoon, M. H. Sol-gel metal oxide dielectrics for all-solution-processed electronics. *Materials Science and Engineering R: Reports* **114**, 1–22 (2017).
 125. Jittiarporn, P., Badilescu, S., Al Sawafta, M. N., Sikong, L. & Truong, V. Van. Electrochromic properties of sol–gel prepared hybrid transition metal oxides – A short review. *Journal of Science: Advanced Materials and Devices* **2**, 286–300 (2017).
 126. Wang, D. *et al.* Sol–gel synthesis of Nd-doped BiFeO₃ multiferroic and its characterization. *Ceramics International* **41**, 8768–8772 (2015).
 127. Gao, T. *et al.* Synthesis of BiFeO₃ nanoparticles for the visible-light induced photocatalytic property. *Materials Research Bulletin* **59**, 6–12 (2014).
 128. Rusevova, K. *et al.* LaFeO₃ and BiFeO₃ perovskites as nanocatalysts for contaminant degradation in heterogeneous Fenton-like reactions. *Chemical Engineering Journal* **239**, 322–331 (2014).
 129. Danks, A. E., Hall, S. R. & Schnepf, Z. The evolution of ‘sol–gel’ chemistry as a technique for materials synthesis. *Materials Horizons* **3**, 91–112 (2016).
 130. Yang, Q., Liu, G. & Liu, Y. Perovskite-type oxides as the catalyst precursors for preparing supported metallic nanocatalysts: A review. *Industrial & Engineering Chemistry Research* **57**, 1–17 (2018).
 131. Khodabakhsh, M., Sen, C., Khassaf, H., Gulgun, M. A. & Misirlioglu, I. B. Strong smearing and disappearance of phase transitions into polar phases due to inhomogeneous lattice strains induced by A-site doping in Bi_{1-x}A_xFeO₃

- (A: La, Sm, Gd). *Journal of Alloys and Compounds* **604**, 117–129 (2014).
132. Wang, P. & Pu, Y. Enhanced ferroelectric and piezoelectric properties of $\text{La}_x\text{Bi}_{(1-x)}\text{FeO}_3$ ceramics studied by impedance spectroscopy. *Ceramics International* **43**, S115–S120 (2017).
133. Godara, P., Agarwal, A., Ahlawat, N. & Sanghi, S. Crystal structure, dielectric and magnetic properties of Gd doped BiFeO_3 multiferroics. *Physica B: Condensed Matter* **550**, 414–419 (2018).
134. Liu, S. *et al.* Effect of Nd-doping on structure and microwave electromagnetic properties of BiFeO_3 . *Journal of Magnetism and Magnetic Materials* **426**, 267–272 (2017).
135. Costa, L. V. *et al.* Experimental evidence of enhanced ferroelectricity in Ca doped BiFeO_3 . *Materials Chemistry and Physics* **144**, 476–483 (2014).
136. Dhir, G., Uniyal, P. & Verma, N. K. Multiferroic properties of Sr-doped BiFeO_3 nanoparticles. *Physica B: Condensed Matter* **531**, 51–57 (2018).
137. Layek, S., Verma, H. C. & Garg, A. Enhancement in magnetic properties of Ba-doped BiFeO_3 ceramics by mechanical activation. *Journal of Alloys and Compounds* **651**, 294–301 (2015).
138. Abdul Satar, N. S. *et al.* Facile green synthesis of yttrium-doped BiFeO_3 with highly efficient photocatalytic degradation towards methylene blue. *Ceramics International* **45**, 15964–15973 (2019).
139. Yang, R., Sun, H., Li, J. & Li, Y. Structural, magnetic and photocatalytic properties of Sr^{2+} doped BiFeO_3 nanofibres fabricated by electrospinning. *Ceramics International* **44**, 14032–14035 (2018).
140. Meng, W. *et al.* Influence of lanthanum-doping on photocatalytic properties of BiFeO_3 for phenol degradation. *Cuihua Xuebao/Chinese Journal of Catalysis* **37**, 1283–1292 (2016).
141. Jaffari, Z. H., Lam, S. M. & Sin, J. C. Photocatalytic degradation of organic pollutants using magnetic Pd-doped BiFeO_3 composites under visible light irradiation. in *AIP Conference Proceedings* **2157**, 020041 (2019).
142. Sharma, S., Mishra, A., Saravanan, P., Pandey, O. P. & Sharma, P. Effect of Gd-substitution on the ferroelectric and magnetic properties of BiFeO_3

- processed by high-energy ball milling. *Journal of Magnetism and Magnetic Materials* **418**, 188–193 (2016).
143. Zhang, Y. *et al.* Continuously enhanced photoactivity of hierarchical β - $\text{Bi}_2\text{O}_3/\text{Bi}_2\text{S}_3$ heterostructure derived from novel BiO_2CH_3 octagonal nanoplates. *Applied Catalysis A: General* **514**, 146–153 (2016).
 144. Yang, Y., Kang, L. & Li, H. Enhancement of photocatalytic hydrogen production of BiFeO_3 by Gd^{3+} doping. *Ceramics International* **45**, 8017–8022 (2019).
 145. Goncalves, L. F., Rocha, L. S. R., Longo, E. & Simões, A. Z. Calcium doped BiFeO_3 films: Rietveld analysis and piezoelectric properties. *Journal of Materials Science: Materials in Electronics* **29**, 784–793 (2018).
 146. Dahiya, R., Agarwal, A., Sanghi, S., Hooda, A. & Godara, P. Structural, magnetic and dielectric properties of Sr and V doped BiFeO_3 multiferroics. *Journal of Magnetism and Magnetic Materials* **385**, 175–181 (2015).
 147. Zhang, J., Wu, Y.-J. & Chen, X.-J. Structural evolution and enhanced magnetization of $\text{Bi}_{1-x}\text{Pr}_x\text{FeO}_3$. *Journal of Magnetism and Magnetic Materials* **382**, 1–6 (2015).
 148. Yuan, X. *et al.* Sr and Pb co-doping effect on the crystal structure, dielectric and magnetic properties of BiFeO_3 multiferroic compounds. *Journal of Alloys and Compounds* **708**, 93–98 (2017).
 149. Wen, X., Chen, Z., Liu, E., Lin, X. & Chen, C. Effect of Ba and Mn doping on microstructure and multiferroic properties of BiFeO_3 ceramics. *Journal of Alloys and Compounds* **678**, 511–517 (2016).
 150. Gupta, M., Gupta, M., Anu, Mudsinaiyan, R. K. & Randhawa, B. S. Physico-chemical analysis of pure and Zn Doped Cd ferrites ($\text{Cd}_{1-x}\text{Zn}_x\text{Fe}_2\text{O}_4$) nanofabricated by Pechini sol-gel method. *Journal of Analytical and Applied Pyrolysis* **116**, 75–85 (2015).
 151. Loghman-Estarki, M. R., Torkian, S., Rastabi, R. A. & Ghasemi, A. Effect of annealing temperature and copper mole ratio on the morphology, structure and magnetic properties of $\text{Mg}_{0.5-x}\text{Cu}_x\text{Zn}_{0.5}\text{Fe}_2\text{O}_4$ nanoparticles prepared by the modified Pechini method. *Journal of Magnetism and Magnetic Materials*

- 442**, 163–175 (2017).
152. Chandel, S. *et al.* Investigation of excess and deficiency of iron in BiFeO₃. *Materials Chemistry and Physics* **204**, 207–215 (2018).
153. Song, G. L. *et al.* Effects of trivalent gadolinium and cobalt co-substitution on the crystal structure, electronic transport, and ferromagnetic properties of bismuth ferrite. *Materials Science in Semiconductor Processing* **27**, 899–908 (2014).
154. Hussain, S. & Hasanain, S. K. Chemical pressure induced red shift in band gap and d-d transition energies in Sr doped BiFeO₃. *Journal of Alloys and Compounds* **688**, 1151–1156 (2016).
155. Ahmed, M. A., Mansour, S. F. & Ismael, H. A comparative study on the magnetic and electrical properties of MFe₁₂O₁₉ (M=Ba and Sr)/BiFeO₃ nanocomposites. *Journal of Magnetism and Magnetic Materials* **378**, 376–388 (2015).
156. Naeimi, A. S., Dehghan, E., Sanavi Khoshnoud, D. & Gholizadeh, A. Enhancement of ferromagnetism in Ba and Er co-doped BiFeO₃ nanoparticles. *Journal of Magnetism and Magnetic Materials* **393**, 502–507 (2015).
157. García-Zaleta, D. S. *et al.* Influence of phases content on Pt/TiO₂, Pd/TiO₂ catalysts for degradation of 4-chlorophenol at room temperature. *Journal of Nanomaterials* **2016**, (2016).
158. Baek, C.-W. *et al.* Effect of Ba(Cu_{1/3}Nb_{2/3})O₃ content on multiferroic properties in BiFeO₃ ceramics. *Materials Science and Engineering: B* **177**, 451–455 (2012).
159. Saravana Kumar, K., Aswini, P. & Venkateswaran, C. Effect of Tb–Mn substitution on the magnetic and electrical properties of BiFeO₃ ceramics. *Journal of Magnetism and Magnetic Materials* **364**, 60–67 (2014).
160. Gu, Y. *et al.* Structural transformation and multiferroic properties of Sm and Ti co-doped BiFeO₃ ceramics with Fe vacancies. *Ceramics International* **43**, 14666–14671 (2017).
161. Haimin, L., Jianguo, Z., Mingzhe, H., Qingsong, Y. & Chunli, Q. Effect of different annealing atmosphere on ferroelectric properties of 0.7BiFeO₃-

- 0.3PbTiO₃ Thin Films. *Rare Metal Materials and Engineering* **45**, 1449–1454 (2016).
162. Vishwakarma, A. K., Tripathi, P., Srivastava, A., Sinha, A. S. K. & Srivastava, O. N. Band gap engineering of Gd and Co doped BiFeO₃ and their application in hydrogen production through photoelectrochemical route. *International Journal of Hydrogen Energy* **42**, 22677–22686 (2017).
 163. Hasan, M. et al. Saturation magnetization and band gap tuning in BiFeO₃ nanoparticles via co-substitution of Gd and Mn. *Journal of Alloys and Compounds* **687**, 701–706 (2016).
 164. Hasan, M. et al. Saturation magnetization and band gap tuning in BiFeO₃ nanoparticles via co-substitution of Gd and Mn. *Journal of Alloys and Compounds* **687**, 701–706 (2016).
 165. Li, Z.-J. et al. Unusual continuous dual absorption peaks in Ca-doped BiFeO₃ nanostructures for broadened microwave absorption. *Nanoscale* **8**, 10415–10424 (2016).
 166. Xian, H., Tang, L., Mao, Z., Zhang, J. & Chen, X. Bounded magnetic polarons induced enhanced magnetism in Ca-doped BiFeO₃. *Solid State Communications* **287**, 54–58 (2019).
 167. Ridzwan, M. H. et al. Structural, electronic and magnetic properties of Ca, Sr and Ba heterovalent A-site ion substitution in BiFeO₃ with different Fe oxidation states. *Materials Today: Proceedings* **7**, 686–691 (2019).
 168. Hussain, S. & Hasanain, S. K. Chemical pressure induced red shift in band gap and d-d transition energies in Sr doped BiFeO₃. *Journal of Alloys and Compounds* **688**, 1151–1156 (2016).
 169. Kaur, B. et al. AC impedance spectroscopy, conductivity and optical studies of sr doped bismuth ferrite nanocomposites. *International Journal of Electrochemical Science* **11**, 4120–4135 (2016).
 170. Liu, L. et al. Effects of (La, Sr) co-doping on electrical conduction and magnetic properties of BiFeO₃ nanoparticles. *Chinese Physics B* **25**, 097801 (2016).
 171. Irfan, S. et al. Band-Gap Engineering and Enhanced Photocatalytic Activity of Sm and Mn Doped BiFeO₃ Nanoparticles. *Journal of the American Ceramic*

- Society **100**, 31–40 (2017).
172. Lu, L., Lv, M., Liu, G. & Xu, X. Photocatalytic hydrogen production over solid solutions between BiFeO₃ and SrTiO₃. *Applied Surface Science* **391**, 535–541 (2017).
 173. Gao, C. *et al.* Tri-state bipolar resistive switching behavior in a hydrothermally prepared epitaxial BiFeO₃ film. *Journal of Alloys and Compounds* **649**, 694–698 (2015).
 174. Yi, J. *et al.* Structure, dielectric, ferroelectric, and magnetic properties of (1-x)BiFeO₃-x(Ba_{0.85}Ca_{0.15})(Zr_{0.10}Ti_{0.90})O₃ ceramics. *Materials Research Bulletin* **66**, 132–139 (2015).
 175. Guilin, S., Jian, S., Zhang, N. & Fanggao, C. Effects of oxygen content on the electric and magnetic properties of BiFeO₃ compound. *Physica B: Condensed Matter* **493**, 47–52 (2016).
 176. Song, G. lin, Su, J., Yang, H., Zhang, N. & Chang, F. Modified crystal structure, dielectric properties, and magnetic phase transition temperature of Ca doped BiFeO₃ ceramic. *Journal of Sol-Gel Science and Technology* **85**, 421–430 (2018).
 177. Wang, X. *et al.* Novel electrical conductivity properties in Ca-doped BiFeO₃ nanoparticles. *Journal of Nanoparticle Research* **17**, 209 (2015).
 178. Ye, W., Tan, G., Yan, X., Ren, H. & Xia, A. Structural and multiferroic properties of Bi_{0.92-x}H_{0.08}Ca_xFe_{0.97}Mn_{0.03}O₃ thin film. *Ceramics International* **42**, 481–489 (2016).
 179. Yun, Q., Bai, A. & Zhao, S. Lattice distortion of holmium doped bismuth ferrite nanofilms. *Journal of Rare Earths* **32**, 884–889 (2014).
 180. Wang, F. *et al.* Oxygen vacancies induced by zirconium doping in bismuth ferrite nanoparticles for enhanced photocatalytic performance. *Journal of Colloid and Interface Science* **508**, 237–247 (2017).
 181. Lam, S. M., Jaffari, Z. H. & Sin, J. C. Hydrothermal synthesis of coral-like palladium-doped BiFeO₃ nanocomposites with enhanced photocatalytic and magnetic properties. *Materials Letters* **224**, 1–4 (2018).
 182. Casillas, J. E. *et al.* Promotion effect of ZnO on the photocatalytic activity of

- coupled Al_2O_3 - Nd_2O_3 - ZnO composites prepared by the sol-gel method in the degradation of phenol. *Applied Catalysis B: Environmental* **208**, 161–170 (2017).
183. Piña-Pérez, Y. *et al.* Photocatalytic activity of Al_2O_3 improved by the addition of $\text{Ce}^{3+}/\text{Ce}^{4+}$ synthesized by the sol-gel method. Photodegradation of phenolic compounds using UV light. *Fuel* **198**, 11–21 (2017).
184. de Moraes, N. P. *et al.* Effect of synthesis medium on structural and photocatalytic properties of ZnO /carbon xerogel composites for solar and visible light degradation of 4-chlorophenol and bisphenol A. *Colloids and Surfaces A: Physicochemical and Engineering Aspects* **584**, 124034 (2020).
185. Khan, H., Usen, N. & Boffito, D. C. Spray-dried microporous Pt/TiO_2 degrades 4-chlorophenol under UV and visible light. *Journal of Environmental Chemical Engineering* **7**, 103267 (2019).
186. Soltani, T. & Lee, B. K. Improving heterogeneous photo-Fenton catalytic degradation of toluene under visible light irradiation through Ba-doping in BiFeO_3 nanoparticles. *Journal of Molecular Catalysis A: Chemical* **425**, 199–207 (2016).
187. Epp, J. X-ray diffraction (XRD) techniques for materials characterization. in *Materials Characterization Using Nondestructive Evaluation (NDE) Methods* 81–124 (2016).
188. Abd Mutualib, M., Rahman, M. A., Othman, M. H. D., Ismail, A. F. & Jaafar, J. Scanning Electron Microscopy (SEM) and Energy-Dispersive X-Ray (EDX) Spectroscopy. in *Membrane Characterization* 161–179 (2017).
189. Yurdakal, S., Garlisi, C., Özcan, L., Bellardita, M. & Palmisano, G. (Photo)catalyst Characterization Techniques. in *Heterogeneous Photocatalysis* **4**, 87–152 (2019).
190. Ohara, S., Adschariri, T., Miyahara, M., Kaneko, K. & Ohtomo, A. Characterization Methods for Nanostructure of Materials. in *Nanoparticle Technology Handbook* 255–300 (2018).

Annexes

About the characterization techniques

Universidad Juárez Autónoma de Tabasco.

A.1 X-Ray Diffraction (XRD)

The XRD methods are based on the ability of crystals to diffract X-rays in a characteristic manner allowing a precise study of the structure of crystalline phases. Recorded diffraction patterns contain additive contributions of several micro- and macrostructural features of a sample. Based on the peak intensity, information about crystal structure (atomic positions, temperature factor, or occupancy) as well as texture and quantitative phase analyses can be obtained. The peak shape gives information about sample broadening contributions (microstrains and crystallite size). In the field of materials science and engineering, several applications were developed to become state of the art techniques, qualitative and quantitative phase analyses and investigations of crystallographic textures.

X-rays are high-energy electromagnetic waves with a wavelength between 10^{-3} and 10^1 nm. The generation of X-rays is generally achieved using sealed tubes or rotating anodes. Sealed tubes and rotating anodes, which are used in laboratory equipment, both produce X-rays by the same principle. Electrons generated by heating a tungsten filament in a vacuum are accelerated through a high potential field and then directed to a target which then emits X-rays.

7

The incident electrons induce two effects leading to the generation of X-rays: the first is the deceleration of the electrons leading to the emission of X-ray photons with a broad continuous distribution of wavelength. The second is the ionization of the impinged atoms by ejecting electrons from the inner shells. The difference between the electron energies of the inner shell and of the incoming electron is emitted in the form of photons, with a characteristic energy depending on the initial and final shell position of the electrons and on the material. The characteristic radiation requires minimum excitation potential of the electrons to be emitted, which depends on the target material.

The radiation coming out of a sealed tube or a rotating anode is therefore a superimposition of a continuous spectrum and of characteristic radiations. In general, XRD methods only use the characteristic radiation with the highest intensity,

the K α radiation, and remove most of the remaining radiation by using appropriate filters or monochromators.

When X-ray photons reach matter, several types of interactions can take place leading to different absorption and scattering effects. An elastic scattering, also called Rayleigh scattering, occurs between the photons and the electrons surrounding the atomic nuclei. In this case, the energy of the scattered wave is unchanged, and it retains its phase relationship to the incident wave. Consequently, the X-ray photons impinging on all atoms of an irradiated volume are scattered in all directions. However, due to the periodic nature of a crystalline structure, constructive or destructive scattered radiation will result, leading to characteristic diffraction phenomena which can be studied to investigate the crystal structure of materials.

The principle of the methods is based on the XRD by periodic atomic planes and the angle or energy-resolved detection of the diffracted signal. The geometrical interpretation of the XRD phenomenon (constructive interferences) has been given by W.L. Bragg. The determination of Bragg's law is given in [Equation 16](#).

$$n\lambda = 2d_{hkl}\sin\theta \quad 16$$

where n is the order of diffraction, λ is the wavelength of the incident beam in nm, d_{hkl} is the lattice spacing in nm and θ is the angle of the diffracted beam in degree. In a polycrystalline, untextured material with fine grains, diffraction occurs for each lattice plane and direction that satisfies the Bragg's law in the case of constructive interferences. This results in the occurrence of diffraction cones appearing in the form of so-called Debye rings or diffraction rings if detected by a plane detector. The total intensity diffracted by a considered unit cell is described by the summation of the intensity scattered from the individual atoms. The diffracted intensities $I_{(hkl)}$ are directly proportional to the square of the crystallographic structure factor $F_{(hkl)}$, which is a complex quantity.

According to the crystal symmetry, different extinctions of interferences will occur, leading to different diffraction patterns. For example, in the case of body-centered

lattices, diffraction occurs if the condition $h + k + l = 2n$ is satisfied, while in face-centered lattices, the condition $h + k, k + l, h + l = 2n$ must be satisfied. The total diffracted intensity for a lattice plan family ($I_{(hkl)}$) depends on several factors. These terms are combined to obtain an expression describing the total intensity at any 2θ position. In general, diffraction data are represented as intensity distribution as a function of the 2θ angle.

3

After background subtraction, the maximum peak intensity I_{max} can be defined as well as the integrated intensity I_{int} (area under the peak). The peak position can be determined by several methods (center of gravity, fit of different mathematical function, etc.). The peak width can be generally characterized either by the full width at half maximum (FWHM) corresponding to the peak breadth at half of the maximum intensity, or by the integral breadth (IB), which corresponds to the width of a rectangle of the same maximal and integrated intensity as the considered peak.

Different lattice planes are in diffracting conditions, and varying intensities of the diffracted signal occur according to the crystal structure of the present phases. Consequently, each phase produces a characteristic diffraction pattern that allows its identification. Moreover, when several phases are present in a system, the characteristic patterns of all phases are superimposed and the intensity of the diffraction peaks of the phases are respectively proportional to their amounts.

3

In order to identify the present phases, a comparison of the present diffraction peaks with known data from a database must be performed. The main available database is provided by the International Center for Diffraction Data (ICDD) and is based on different scientific sources (<http://www.icdd.com/>). For each documented phase, lattice structure, space group, lattice parameters, and the corresponding position, intensity and indexation (Miller's indices) of diffraction peaks are available. The databases are now available electronically and can be integrated in the software packages of most of the providers of diffraction equipment.

After the measurement of the diffraction pattern, a data treatment can be required in order to achieve reliable results. In general, the background must be subtracted from

the measured pattern. Further pattern treatment, such as mathematical removal of $K_{\alpha 2}$ radiation or smoothing operations, might be indicated.

First, the chemical elements which should be considered for the possible phases have to be selected. For this the knowledge about the chemical composition of the analyzed sample is required and therefore at least a qualitative element analysis should be available.³ All elements which are not present can then be discarded, while available elements can be marked as "mandatory" or as "possibly present" for the considered phases. The measured peak data are automatically compared with the entries of the database that fulfill the criterion, which results in a list of possible phases. For each phase, quality marks giving information about the quality and the reliability of the data are specified and should be considered in order to evaluate the results. For every proposed phase, theoretical peak positions and the associated theoretical intensity are shown superimposed to the measured pattern.

The final selection of the present phases can therefore only be performed by the user on the base of the proposed results and of his knowledge about the investigated sample and the measurement conditions. In an ideal case, all measured diffraction peaks should be assigned to a phase [187].

A.2 Rietveld Refinement

By this method the whole measured pattern is refined with a calculated pattern considering several structural, microstructural, and experimental parameters. The refinement is performed by minimization of the function S given in Equation 17.

$$S = \sum_i u_i |y_{i\text{obs}} - y_{i\text{calc}}|^2 \quad 17$$

3

In this equation, $y_{i\text{obs}}$ the measured and $y_{i\text{calc}}$ the calculated intensities at each 2θ position i and u_i , a weighting factor taken from the experimental error margins, which are assumed to be proportional to the square root of the count rate $y_{i\text{obs}}$ following Poisson counting statistics. The calculation of $y_{i\text{calc}}$ at each position i is a function of instrumental contribution, reflections of all present phases, backgrounds, etc.

All factors depending on each phase of the analyzed sample which are taken into account for the refinement are as follows: position of all atoms in the elementary lattice; temperature factor; occupation factor; space group of the lattice; lattice parameters; texture; crystallite size; microstrains; and phase contents. Moreover, several instrumental parameters are also considered in order to separate the contribution of instrument and sample.

All geometrical features of the instrument are described by functions that are convoluted to each other. By correct calculation of the instrumental function, contribution of sample properties to the diffraction pattern can be analyzed. The 3 instrumental function can also be measured by using a standard without sample broadening. In general, the standard SRM660a (LaB_6) is used, as the large crystallites of about 2 mm do not lead to a significant broadening of the peaks.

At the end of a refinement, it is necessary to check whether the results are reliable and whether they meet certain standard criteria. The overall best criterion for the refinement is difference plots between observed and calculated data. When large discrepancies are present, the different parameters considering for the refinement must be checked. The calculated criterion Residuals weighted profile (R_{wp}) gives a reliable information about the fit quality. Thereby, the smallest R_{wp} value represents

the best refinement. It is calculated as shown in [Equation 18](#). The parameter R_{exp} ([Equation 19](#)) represents the minimum expected R_{wp} depending on the number of experimental points (N) and the number of refined parameters (Q). The ratio of both parameters gives the goodness of fit (GOF), which can also be used as a criterion of the refinement quality ([Equation 20](#)).

$$R_{wp} = \sqrt{\frac{\sum_i u_i (y_{i,obs} - y_{i,calc})^2}{\sum_i u_i (y_{i,obs})^2}} \quad 18$$

$$R_{exp} = \sqrt{\frac{N-Q}{\sum_i u_i (y_{i,obs})^2}} \quad 19$$

$$GOF = \left(\frac{R_{wp}}{R_{exp}}\right)^2 \quad 20$$

With this method, complex multiphase materials can be analyzed in order to determine the respective phase contents. Also, it can be used for the evaluation of crystallographic texture, crystallite size, strains and microstrains. However, in order to get reliable results, precise information about the crystal structure of the present phases, including the atom coordinates within the lattice, is required.

3

With this powerful method, very complex multiphase materials can be investigated and quantitative analysis can be performed. However, the method must be used carefully as many parameters can be refined without physical meaning that would lead to good refinements but erroneous results. Therefore, parameter constraints and control are mandatory for such analyses.

A.3 Scanning Electron Microscopy (SEM)

Electron microscopy technique is one of the available techniques that allows the imaging of the surface of specimen. This technique utilizes the interaction between the electrons with the specimen for the generation of topological images. With higher magnification than the light microscope, the electron microscopy has allowed to observe matter at finer detail, past the capabilities of the naked human eye.

2

Different electron detector picks up the corresponding electron for the generation of the morphological images. The electron source is one of the most important components in SEM. Although conventional emitter is reliable and cheap, it falls short in the image production. On the other hand, by detecting the X-ray emitted by the sample, the elemental composition of the specimen can be calculated. This is the working principle of energy dispersive X-ray spectroscopy (EDS). The electron microscopies are essential for the identification of surface conditions, morphological detection, elemental distribution and composition, layer density, and others.

SEM is an electron microscope that uses a focused beam of electrons that react with the sample to produce a topological image and relative composition. Upon contact with the sample, the focused beam of electron will produce secondary electrons (SEs), backscattered electrons, and characteristic X-ray, which is then detected with respective detectors and finally displayed on the monitor. The main components in a typical SEM include the electron source, column which contains electromagnetic lenses, electron detector, sample chamber, and the computer display.

SEM image formation is mainly correlated with the detection of signals received from the interactions between electron signals and the scanned samples. Generally, there are two type of interactions that can occur, namely elastic and inelastic interactions. In the inelastic interaction, low-energy SEs are emitted from the samples after bombarded by the primary beam electrons (transfer of energy to the atom in the sample). On the other hand, elastic interaction is due to the deflection of primary electron upon contact with samples atomic nucleus or electrons of comparable energy.

The deflection of the scattered electrons is at an angle of more than 90 degrees are called back scattered electrons (BSE) and can be utilized for sample imaging. SE mode is the most common type of signal used for SEM image processing. As the incident electrons have relatively low energy, detection can only be achieved to a few nanometers of the sample surface. Thus, SE is relatively accurate to produce the topological contrast of the sample such as surface texture and roughness. It is worth to note that only the SEs that reach the detector will be producing the image, and obstructed SEs will produce dark contrast for the image. Additionally, low voltage electron in the primary beam will most probably produce the SEs from the utmost surface of the sample, thus accurately portraying the detailed topographic information of the sample.

BSE mode of scanning mostly involves the detection of indecent electron with energy higher than 50 eV. The elastic collision of the electron with a higher than 90 degrees directional change will result in almost half of the electrons bouncing back to the direction of its origin and retaining most of its initial energy. Higher atomic number elements will deflect more electrons due to high number of positive ions on its nucleus. BSE yield is defined as percentage of reflected electrons produced by the sample. BSE electrons carry a significant information regarding the structures under the surface of the samples.

For a flat sample, BSE mode would produce a relatively different topological image than the SE mode. In the formation of the images via BSE, the electrons must travel in a straight path from the specimen for it to be detected. The image generation of SE mode is dependent on the surface topography, meanwhile in BSE mode, the atomic number of elements on the surface of the samples will contribute to the contrast in the image, thus allowing distinction in the boundary between different elements.

The electron source is usually either tungsten filament or solid-state crystal. The tungsten electron filament is the most common types of electron source mainly due to its low price point, high reliability, and suitability for low magnification imaging and

X-ray microanalysis. It is shaped like an inverted "V" and heated resistively to irradiate electrons. The diameter of the filament is about 100 mm. The tungsten electron source (the cathode) is usually accompanied with a Wehnelt cylinder and an anode. High voltage source will be supplied to the tungsten and the Wehnelt cylinder at a range of $0.1\text{e}30$ kV. Wehnelt cylinder will function to induce the occurrence of the electron beam, whereas the anode accelerates the electron beam after leaving the thermionic source. Due to the thermionic emission of the heated tungsten, the electron will spread to a wide trajectory from the source. Nevertheless, the Wehnelt cylinder will produce a focusing force to the electron beam.

The current supplied determines the value of electron emission. At the most effective emission point (saturation point), the filament will emit the highest amount of electron with the lowest possible current. If higher current is applied to the filament, negligible difference in amount of electron emission is observed. The occurrence of a false peak is different from one filament to another. The false peak is most probably due to the filament geometries during heating. If the filament is set to work at the false peak, longer lifetime is achieved but at the expense of low electron beam stability. If the filament is subjected to a higher current than the saturation point, the lifetime will reduce significantly. The working life of the filament can also be influenced by the working environment in the SEM.

The solid-state crystal usually consists of lanthanum hexaboride (LaB_6) or cerium hexaboride (CeB_6). It has higher brightness output compared to the tungsten filament and possesses longer life hours than the tungsten filament due to its lower work function. In other terms, the solid-state crystal can produce a higher rate of emission than the tungsten filament with equivalent current supplied. The solid-state crystal is mounted on a support which is usually graphite or rhenium. The support must not be reactive with the solid-state crystal and be able to heat up the solid-state crystal until it can emit the electron beams. In addition to its low work function, the solid-state crystal has much lower effective emission area than the tungsten filament and be able to produce high-resolution SEM images.

The solid-state crystal electron source can be easily fitted into a conventional SEM with a tungsten filament. Nevertheless, the hexaboride crystal needs a high vacuum chamber to avoid contamination at elevated temperature.

EDS is involved in the detection of elemental composition of substance by using SEM. EDS can detect elements that possess the atomic number of higher than boron and these elements can be detected at concentration of least 0.1%. The application of EDS includes material evaluation and identification, contamination identification, spot detection analysis of regions up to 10 cm in diameter, quality control screening, and others.²

Upon collision with the electron beam in typical SEM, the samples interact with the beam and produce characteristic X-rays. Due to the principle that none of the elements have the same X-ray emission spectrum, they can be differentiated and measured for its concentration in the sample. The X-ray is the result of the primary beam of electron interaction with the nucleus of the sample atom. Primary electron beam will excite the electron in the nucleus of an atom, ejecting it from the nucleus and creating an electron hole. An electron from the outer shell (higher energy) of the atom will replace the missing ejected electron and releases the superfluous X-ray. The emitted X-ray consists of X-ray continuum (generated by the deceleration of electron) and characteristic X-ray (generated resulting of higher shell electron filling the electron hole in the nucleus shell).

X-ray continuum is not paramount for the identification of elements in the sample and need to be identified to differentiate them. The intensity of the X-ray continuum is contributed by the factors such as probe current, accelerating voltage supplied, and the atomic number of the sample. On the other hand, the characteristic X-ray will be recorded by the energy dispersive spectrometer for the measurement of the elemental composition in the specimen [188].²

A.4 UV-Vis Diffuse Reflectance Spectroscopy (DRS)

UV-Visible (UV-Vis) spectroscopy is a useful technique for the determination of the absorption properties of materials. Particularly, in the case of semiconductors, measurements of diffuse reflectance allow to estimate the bandgap energy value.

This parameter is critical in the field of photocatalysis since it determines the light energy to be used to activate the semiconducting solids. As far as catalysts are concerned, the diffused reflectance technique provides information on the electronic properties of a solid and—in the presence of transition metals cations—on the coordination and oxidation state of metal.⁶

UV and Vis radiations are part of the electromagnetic spectrum. The study of the interactions of the electromagnetic radiation with the matter (spectroscopy) allows to gain relevant knowledge on the materials of interest, such as the absorption, transmission, and reflectivity properties.

Absorbance spectroscopy, or spectrophotometry, is the quantitative determination of the amount of light absorbed or transmitted by a given material as a function of wavelengths. This gives information about the electronic transitions happening in the studied material. In the case of isolated atoms only electronic transitions can occur, while, in the case of molecules, rotational and vibrational motions are also generated.

When light reaches matter an interaction occurs and, depending on the structure of the materials and on the wavelength of the light, different phenomena can be observed: photon absorption, scattering, reflection, or refraction.

The various components in which the incident light is split after the interaction with the sample are represented by [Equation 21](#):

$$I_0 = A\% + T + R + S$$

⁵ where $A\%$ is the absorbance ($A\% = 1 - 10^A$), T is the transmitted light, R is the reflected light, and S is the scattered light.

Additionally, the fraction of the transmitted light can be calculated by the Beer-Lambert law (Equation 22), which states that the ratio between the fraction of the light measured after interaction with the sample (I) and the incident intensity (I_0) depends on the path length of light through the sample (l) and on the material properties (k_λ is the attenuation coefficient, a typical constant of the medium crossed by the light and depends on the wavelength λ):

$$\frac{I}{I_0} = e^{-k_\lambda l} = T \quad 22$$

The ratio I/I_0 is defined as transmittance (T), whereas absorbance (A) can be calculated from the opposite of the natural logarithm of T , the expression assumes the following form (Equation 23):

$$A = k_\lambda l = \varepsilon c l = -\ln \frac{I}{I_0} \quad 23$$

where ε is the molar absorptivity coefficient of the material and c is the concentration of the absorbing species. From the Beer-Lambert law, it can be deduced that the amount of light absorbed by a medium is independent of the intensity of the incident light.

5 In the case of semiconducting solids, UV-Vis spectroscopy allows to calculate the optical band gap (E_g), namely the minimum energy that must be supplied to an electron to promote it from the top of the valence band to the bottom the conduction band (CB) and the electronic processes occurring in the material after the interaction with the light. The E_g value determination is the first key step when dealing with semiconductors to be used in all technologies involving the conversion of solar to chemical or electric energy.

When a monochromatic light impinges the surface of a powder, a part is absorbed, a part is reflected, and a part is scattered, and after various reflections it can return to the surface. The diffuse reflected light becomes weaker, with respect to the incoming one, if it is partially absorbed by the material. The total reflected light, measured with respect to a non-absorbing material (BaSO_4 , KBr , KCl , MgO) is used,

after some elaborations, to determine the E_g value. Moreover, the occurrence of d-d transitions, exciton binding energies, phonon absorptions and emissions, excitations to or from color centers and/or defect bands can result in a difficult interpretation of UV-Vis diffuse reflectance spectra.

6

The electronic transitions that occur within a material as a result of energy supply (in this case in the form of light energy) are of two types: direct and indirect. Direct transition is described as interaction between two particles (an electron and a photon) where only photons excite electrons, whereas indirect transition is described as a three-particle interaction (photon, electron, and phonon) requiring, at the same time, vibrations and energy transition from the crystal lattice (phonons). A phonon is defined as a unit of vibrational energy that rises from the oscillation of atoms within a crystalline lattice. The lattice vibration, due to the atoms' thermal energy, generates mechanical waves. A packet of these waves can move inside the crystal with a fixed energy and momentum, the waves can be treated as particles, named phonons. Just as a photon is a quantum of electromagnetic energy or light, a phonon is a quantum of vibrational mechanical energy.

From the shape of the DRS it is possible to distinguish the different transition types by mathematical elaborations based on the Tauc [Equation 14](#):

$$\alpha h\nu = A(E_g - h\nu)^n \quad 14$$

where α is the absorption coefficient, h is the Planck's constant, ν is the light frequency, A is the absorption constant, E_g is the band-gap energy, and n is related to the type of electronic transitions. The exponent value is $1/2$ for a direct allowed and 5 3/2 for a direct forbidden transition, 2 for an indirect allowed, and 3 for an indirect forbidden transition. From the graph obtained by plotting $(\alpha h\nu)^{1/n}$ versus $h\nu$ it is possible to calculate the bandgap energy by extrapolating the straight line to $(\alpha h\nu)^{1/n} = 0$ axis (Tauc plot).

The coefficient α can be acquired from the diffuse reflectance spectrum by the Kubelka-Munk function, provided that this function is able to properly describe the

diffuse reflectance phenomena in a solid. When light of determinate energy is absorbed by a material, the measurement of the diffuse reflected light at different wavelengths originates the so-called diffuse reflectance spectrum. By considering an infinitely thick sample, the intensity of the diffuse reflectance spectrum can be expressed by the Kubelka-Munk Equation (Equation 24):

$$F(R_{\infty}) = \frac{(1-R_{\infty})^2}{2R_{\infty}} = \frac{\alpha}{S} \quad 24$$

5 where the reflectance of an “infinitely” thick sample (R_{∞}) represents the ratio of the intensity of light reflected from a sample to the intensity of reflection from a standard sample, α is the absorption coefficient, and S is the scattering coefficient. By introducing the coefficients α and S , both the absorption and scattering phenomena are taken into consideration in Equation 24. If the absorption coefficient is not dependent on wavelength, then $F(R_{\infty})$ is proportional to the absorption coefficient α , and this latter can be substituted in Equation 25:

$$[F(R_{\infty})hv]^{1/n} = A(hv - E_g) \quad 25$$

5 By plotting $[F(R_{\infty})hv]^{1/n}$ versus hv it is possible to calculate the band-gap energy of a material by drawing a tangent line to the point of inflection of the curve: the hv value at the point of intersection of the tangent line with the horizontal axis is the E_g value. The unit for hv is eV (electron volts), and its relationship to the wavelength λ (nm) is $hv = 1239.7/\lambda$ [189].

A.6 X-Ray Photoelectron Spectroscopy (XPS)

X-ray photoelectron spectroscopy (XPS) is a surface analysis technique that is based on energy spectrum measurements of photoelectrons emitted from a material surface under irradiation with a monochromatic soft X-ray radiation. XPS is routinely used for a qualitative and/or quantitative analysis of surface elemental compositions ⁴ and a chemical or an electronic state analysis of each element in the sample surface. A significant feature of the XPS analysis is that the technique is one of the ultimate surface-sensitive methods for analyzing the elements that are present within 1 – 10 nm of the sample surface.

First physical basics involved in the photoelectron emission can be described as when a material surface is irradiated with a photon with an energy of $h\nu$, where h is Planck's constant and ν is the frequency of the radiation, the photon energy is totally absorbed by an electron that is bound in either core levels or valence levels of an atom in a molecule or solid with a binding energy of BE , leading to ionization and the emission of the bound electron out of the atom with an energy of $h\nu - BE$ through the photoelectric effect. Hence, the photoemitted electron is called a photoelectron.

⁴ Main components of the XPS system for the photoelectron measurements include a source of monochromatic X-ray radiation beam, a sample stage with a set of stage manipulator and a sample introduction-transfer mechanism, an electron energy analyzer with an electron collection lens and electron optics, an electron detector system, and mu-metal magnetic field shielding, which are all equipped in an ultrahigh vacuum (UHV) chamber with UHV pumps. In the commonly employed X-ray sources, monochromatic X-rays are usually produced by diffracting and focusing a nonmonochromatic $K\alpha$ X-ray radiation emitted from an electron bombarded thin metal anode (usually Mg or Al), which gives rise to $MgK\alpha$ radiation with a photon energy of 1253.6 eV and $AlK\alpha$ radiation with a photon energy of 1486.6 eV. Photoelectrons, which are emitted from the sample surface through the photoelectric effect, are collected into the electron energy analyzer.

The kinetic energy of the photoelectron measured with the energy analyzer is determined as follows. Here, it is noted that the Fermi levels at the sample surface and the electron energy analyzer are kept at a common level because the sample surface and the electron energy analyzer are electrically connected to each other and thus both of the objects are in thermal equilibrium. Therefore, the kinetic energy of the photoelectrons measured with the electron analyzer (E_k) can be determined using [Equation 26](#):

$$E_k = h\nu - BE - \phi \quad 26$$

where E_k is the kinetic energy of the photoelectron as measured with the electron energy analyzer, BE is the binding energy of the photoelectron emitted from one orbital within the atom as normalized to the common Fermi level, $h\nu$ is the photon energy of the X-ray radiation being used, and Φ is the work function of the electron energy analyzer as normalized to the common Fermi level. The energy spectrum of photoelectrons measured with an XPS system reflects the electronic structures of the atoms because each element produces a characteristic set of XPS peaks at characteristic binding energy values. Therefore, the elements that are present in the sample surface can be directly identified by the characteristic set of XPS peaks.

Dependence of binding energy for electrons in core levels (K, L, and M shells) is shown as a function of the atomic number Z of elements. The binding energy generally increases with increasing atomic number Z of elements, being roughly proportional to the square of the atomic number. The characteristic combinations of the binding energies, which are unique to each element, provide significant advantage of XPS analysis for direct identification of elements, in which discrimination of elements can be easily performed even for neighbor elements in the periodic table.

Furthermore, the exact binding energy of the photoelectron depends not only on the orbital level from which the photoelectron is emitted but also on the local chemical state of the atom, which gives rise to small shifts in the XPS peak positions in the spectrum, being so-called chemical shifts. The small changes in the binding energy

occur due to Coulomb interactions between the photoemitted electron and the ion core that is rearranged by the chemical bonding with the neighbor atoms and/or molecules in the solid. Therefore, information about the chemical states for the specific elements of interest can be analyzed by observation of the chemical shifts.

4

In routine analysis by XPS, two kinds of spectrum survey modes are usually taken in scanning the kinetic energy by properly setting the energy width and the resolution for measurements; (1) wide-scan survey spectrum (wide energy width and low-energy resolution; mainly employed for qualitative analysis of elements) and (2) narrow-scan survey spectrum (narrow energy width and high-energy resolution; mainly employed for quantitative analysis of elemental composition and for analysis of chemical state identification) [190].

Structural, optical and photocatalytic properties of Bi_{1-x}A_xFeO₃ (A = Ca, Sr) synthesized by Pechini method

ORIGINALITY REPORT

20%

SIMILARITY INDEX

PRIMARY SOURCES

- 1 E. Salaya-Gerónimo, D. S. García-Zaleta, G. Jácome-Acatitla, E. Huerta-García et al. " Structural, optical and photocatalytic properties of Sr doped and Ca doped compounds prepared by Pechini method ", Journal of Chemical Technology & Biotechnology, 2022

[Crossref](#)
- 2 M. Abd Mutualib, M.A. Rahman, M.H.D. Othman, A.F. Ismail, J. Jaafar. "Scanning Electron Microscopy (SEM) and Energy-Dispersive X-Ray (EDX) Spectroscopy", Elsevier BV, 2017

[Crossref](#)
- 3 J. Epp. "X-ray diffraction (XRD) techniques for materials characterization", Elsevier BV, 2016

[Crossref](#)
- 4 "Characterization Methods for Nanostructure of Materials", Elsevier BV, 2018

[Crossref](#)
- 5 Sedat Yurdakal, Corrado Garlisi, Levent Özcan, Marianna Bellardita, Giovanni Palmisano. " (Photo)catalyst Characterization Techniques", Elsevier BV, 2019

[Crossref](#)
- 6 coek.info

Internet

- 7 moscow.sci-hub.se Internet 108 words — 1 %
- 8 Leena V. Bora, Rajubhai K. Mewada. "Visible/solar light active photocatalysts for organic effluent treatment: Fundamentals, mechanisms and parametric review", Renewable and Sustainable Energy Reviews, 2017
Crossref 98 words — < 1 %
- 9 Sefiu Adekunle Bello, Funsho Olaitan Kolawole, Stephen Idowu Durowaye, Sunday Wilson Balogun et al. "Recent developments in techniques and technologies for analytical, spectroscopic, structural, and morphological characterization of modern materials of advanced applications", Elsevier BV, 2024
Crossref 60 words — < 1 %
- 10 Chaitanya Sarangapani, N.N. Misra, Vladimir Milosavljevic, Paula Bourke, Finbarr O'Regan, P.J. Cullen. "Pesticide degradation in water using atmospheric air cold plasma", Journal of Water Process Engineering, 2016
Crossref 59 words — < 1 %
- 11 spectrum.library.concordia.ca Internet 52 words — < 1 %
- 12 Hamidah Abdullah, Md. Maksudur Rahman Khan, Huei Ruey Ong, Zahira Yaakob. "Modified TiO₂ photocatalyst for CO₂ photocatalytic reduction: An overview", Journal of CO₂ Utilization, 2017
Crossref 47 words — < 1 %
- 13 Jiadong Xiao, Yongbing Xie, Hongbin Cao. "Organic pollutants removal in wastewater by heterogeneous photocatalytic ozonation", Chemosphere, 2015
Crossref 47 words — < 1 %

- 14 Md Moniruddin, Baurzhan Ilyassov, Xiao Zhao, Eric Smith, Timur Serikov, Niyazbek Ibrayev, Ramazan Asmatulu, Nurxat Nuraje. "Recent progress on perovskite materials in photovoltaic and water splitting applications", Materials Today Energy, 2018
Crossref 47 words — < 1 %
- 15 Eman Abdul Rahman Assirey. "Perovskite synthesis, properties and their related biochemical and industrial application", Saudi Pharmaceutical Journal, 2019
Crossref 46 words — < 1 %
- 16 Qilei Yang, Guilong Liu, Yuan Liu. "Perovskite-Type Oxides as the Catalyst Precursors for Preparing Supported Metallic Nanocatalysts: A Review", Industrial & Engineering Chemistry Research, 2017
Crossref 44 words — < 1 %
- 17 Seo Jin Ki, Ki-Joon Jeon, Young-Kwon Park, Sangmin Jeong, Heon Lee, Sang-Chul Jung. "Improving removal of 4-chlorophenol using a TiO₂ photocatalytic system with microwave and ultraviolet radiation", Catalysis Today, 2017
Crossref 42 words — < 1 %
- 18 Hadis Sepahvand, Shahram Sharifnia. "Photocatalytic overall water splitting by Z-scheme g-C₃N₄/BiFeO₃ heterojunction", International Journal of Hydrogen Energy, 2019
Crossref 35 words — < 1 %
- 19 ijsrset.com Internet 35 words — < 1 %

EXCLUDE QUOTES ON

EXCLUDE BIBLIOGRAPHY ON

EXCLUDE SOURCES OFF

EXCLUDE MATCHES < 35 WORDS